Nano Handling and Measurement of Biological Cells in Culture

Yo Hou

NANO HANDLING AND MEASUREMENT OF

BIOLOGICAL CELLS IN CULTURE

Yu Hou

PhD

2015

UNIVERSITY OF BEDFORDSHIRE

Nano Handling and Measurement of Biological Cells in Culture

by

Yu Hou

A thesis submitted to the University of Bedfordshire in partial fulfillment

of the requirements for the degree of Doctor of Philosophy

ABSTRACT

This thesis systematically investigates the nano handling and measurement techniques for biological cells in culture and studies the techniques to realize innovative and multi-functional applications in biomedicine. Among them, the technique based on AFM is able to visualize and quantify the dynamics of organic cells in culture on the nano scale. Especially, the cellular shear adhesion force on the various locations of biological cells was firstly accurately measured in the research of the cell-substrate interaction in terms of biophysical perspective. The innovative findings are conductive to study the cell-cell adhesion, the cell-matrix adhesion which is related to the cell morphology structure, function, deformation ability and adhesion of cells and better understand the cellular dynamic behaviors. Herein, a new liquid-AFM probe unit and an increment PID control algorithm were implemented suitable for scanning the cell samples under the air conditions and the liquid environments. The influence between the surface of sample and the probe, and the damage of probe during the sample scanning were reduced. The proposed system is useful for the nano handling and measurement of living cells.

Besides, to overcome the limitations of liquid-AFMs, the multiple optical tweezers were developed to integrate with the liquid-AFM. The technique based on laser interference is able to characterize the optical trap stiffness and the escape velocity, especially to realize the capture and sorting of multiple cells by a polarization-controlled periodic laser interference. It can trap and move hundreds of cells without physical contact, and has broad application prospects in cytology. Herein, a new experimental method integrated with the positioning analysis in the Z direction was used to improve the fluid force method for the calibration and characterize the mechanical forces exerted on optical traps and living cells. Moreover, a sensitive and highly efficient polarization-controlled three-beam interference set-up was developed for the capture and sorting of multiple cells. By controlling the polarization angles of the beams, various intensity distributions and different sizes of dots were obtained. Subsequently, we have experimentally

observed multiple optical tweezers and the sorting of cells with different polarization angles, which are in accordance with the theoretical analysis.

ACKNOWLEDGMENTS

LIST OF CONTENTS

LIST OF FIGURES

VIII

LIST OF TABLES

LIST OF ABBREVIATIONS

AFM	Atomic Force Microscope
A/D	Analog to Digital
BS	Beam Splitter
CABG	Coronary Artery Bypass Graft
CCD	Charge-Coupled Device
CTLs	Cytotoxic T Lymphocytes
CLSM	Confocal Laser Scanning Microscope
CMOS	Complementary Metal Oxide Semiconductor
DEP	Dielectrophoresis
DNA	Deoxyribonucleic Acid
D/A	Digital to Analog
ESM	Electromagnetic Scattering Model
ESEM	SEM Integrated Environmental
EM	Electron Microscope
FBS	Fetal Bovine Serum
FIB	Focused Ion Beam
FSD	Fast-Spinning Disc
HIV	Human Immunodeficiency Virus
HRSEM	High Resolution Scanning Electron Microscope
LBI	Laser Beam Interference
IBM	International Business Machines Corporation
LFCM	Laser Flow Cyto Meters

LM	Levenberg-Marquardt
MAT	Micropipette Aspiration Technique
MS	Mechanosensitive
MT	Magnetic Tweezers
NK	Natural Killer Cells
OCT	Optical Coherence Tomography
OM	Optical Microscope
OT	Optical Tweezers
pH	Hydrogen Ion Concentration
PID	Proportional-Integral-Derivative
PPFC	Parallel-Plate Flow Chamber
PSD	Position Sensitive Detector
PT	Poking Technique
PZT	Piezoelectric Ceramic Transducer
QD	Four-Quadrant Photo Detector
RBCs	Red Blood Cells
RNA	Ribonucleic Acid
RO	Ray-Optics
SLM	Spatial Light Modulator
SPM	Scanning Probe Microscope
SS-AFM	Sample-Scanning AFM
TE	Transverse Electric
TIRF	Total internal Reflection Fluorescence
TM	Transverse Magnetic
TRAIL	Tumor Necrosis Factor-Related Apoptosis-Inducing Ligand
TS-AFM	Tip-Scanning AFM
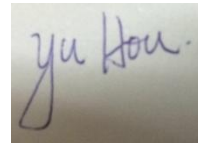
DECLARATION

I declare that this thesis is my own unaided work. It is being submitted for the degree of Doctor of

Philosophy at the University of Bedfordshire.

It has not been submitted before for any degree or examination in any other University.

Name of candidate: Yu Hou   Signature:

Data: 20 December 2015

Chapter 1

Introduction

1.1 Background

The cell is the basic unit of life which can affect the physiological functions of body. The particularity of human body often depends on the performance of single cell. Hence, further investigations on cells will elucidate the overall potential of life, cure diseases, and be the key of life transformation[1][2]. Cells are stimulated by different stresses and strains throughout their lives such as the hydrostatic pressure, the fluid shear force, the drawing force and the stiffness change of extracellular matrix, which come from the internal physiological environment and the external environment. Then, cells will adjust or maintain its internal structure to adapt these stimuli by changing their behaviors, and respond the effects of the external environment simultaneously. Other research has found that the mechanical behaviors from the external environment are involved in the cell survival, proliferation, differentiation and information transfer and so on. Any missing or incorrect stresses and strains will impact cell function, and may lead to diseases including cancer[3]. On the other hand, the morphological structure and functions of cells, cell growth, development, maturity, proliferation, apoptosis, death and carcinogenesis, differentiation and the regulation mechanism of cells, are related to mechanical properties of cells[4][5]. For instance, the study of the interaction between cells and functional material, research of artificial organs, the cell-cell adhesion and cell-substrate adhesion are closely related to the biological compatibility of artificial implants. The exploration of the cell-substrate adhesion is the key factor critical for the success of the implantation operation of artificial organs. Hence, to understand the mechanical properties of single cells as well as their variations is of great significance for the effective prevention, diagnosis, treatment and rehabilitation of diseases. However, the cytology is

much less developed than the molecular biology in the scientific knowledge system. The most important reason is that there is still lack of satisfactory experimental methods and techniques for us to study cells from a vast and diverse of aspects. The force and deformation of the membrane have direct impact on the realization of the cell function and the viability of status. Moreover, nanotechnology at present is increasingly significant in research field due to the exploration of the exciting new physical mechanisms when the research is down to the nano scale. Therefore, the demand for analysis of living cells from the micro/nano scale is an increasing trend for both fundamental biology and clinical diagnostics. There is a need to develop devices and techniques that can physically characterize not only individual cells but also populations of cells more rapidly and with the enhanced sensitivity and required accuracy. Moreover, devices and techniques must be designed so that they can also present cells with the biochemical and mechanical stimuli in a controlled and reproducible way. Thus, there are still challenges to measure the properties of cells accurately, such as keeping the cells survival in repeated experiments, localizing the cells with high efficiency and providing the necessary controlled stimuli.

1.2 Overview of Current Nano Handling and Measurement Techniques of Biological Cells

The traditional research of cell biomechanics mainly includes the cell deformation, the cell movement, the interaction between cells and the force within cells, and responding to the principles. In recent years, with the rapid development of biophysical sciences and nanotechnology, the parameters which include the force, the deformation and the conductance of cells and biological molecules could be accurately detected in their physiological environment.

1.2.1 Nano Handling Techniques of Biological Cells

Up to now, some of the recently developed nano biophysical technological tools and nano handling techniques such as AFM (Atomic Force Microscope), MAT (Micropipette Aspiration

Technique), MT (Magnetic Tweezers), DEP (Dielectrophoresis), OT (Optical Tweezers), and Micro-fluidics and PT (Poking Technique). These techniques can realize the quantitative study biological tissues and molecular changes on the micro/nano scale. For instance, Liu et al used the AFM as an indenter tool to do the indentation experiment in order to obtain the mechanical properties of living SMCC-7721 cancer cells treated with fullerenol ($C_{60}(OH)_{24}$) for 24h, 48h, and 72h[6]. Different mechanical models of probe tips were used to calculate the Young's modulus under different indentation depths, and experimental results showed that the elastic modulus of single living cells could be used as a powerful biomarker to evaluate the effects of fullerenol on the cells and reveal significant information for cellular dynamic behaviors. Figure 1.1 shows the results of Young's modulus measurements by AFM. A global decrease in the Young's modulus is accompanied by the morphological changes of cells with the time-dependent effect.
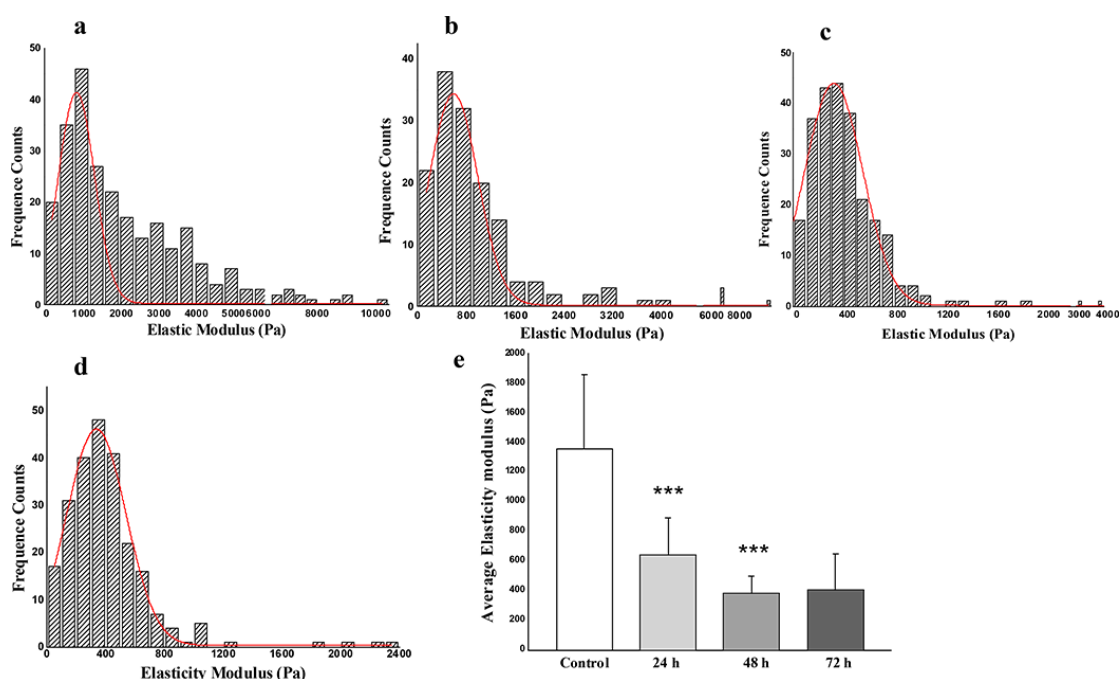
Figure 1.1 Histograms and the normal distributions of elastic modulus -frequency count of living SMCC-7721 cancer cells during the treatment with fullerenol for 24h, 48h, and 72h[6].

Bavi et al used the MAT to characterize the mechanical properties of lipid bilayers which played a crucial role in the gating of MS (Mechanosensitive) channels[7]. Experimental results showed that

excised liposome patch fluorometry was superior for measuring the intrinsic mechanical properties of lipid bilayers. Figure 1.2 shows the four negative pressure steps of -5 to -20 mmHg used for the changes of the nominal in-plane stress in the membrane. The MAT is a micro-handling process and has the advantage of studying single cells.
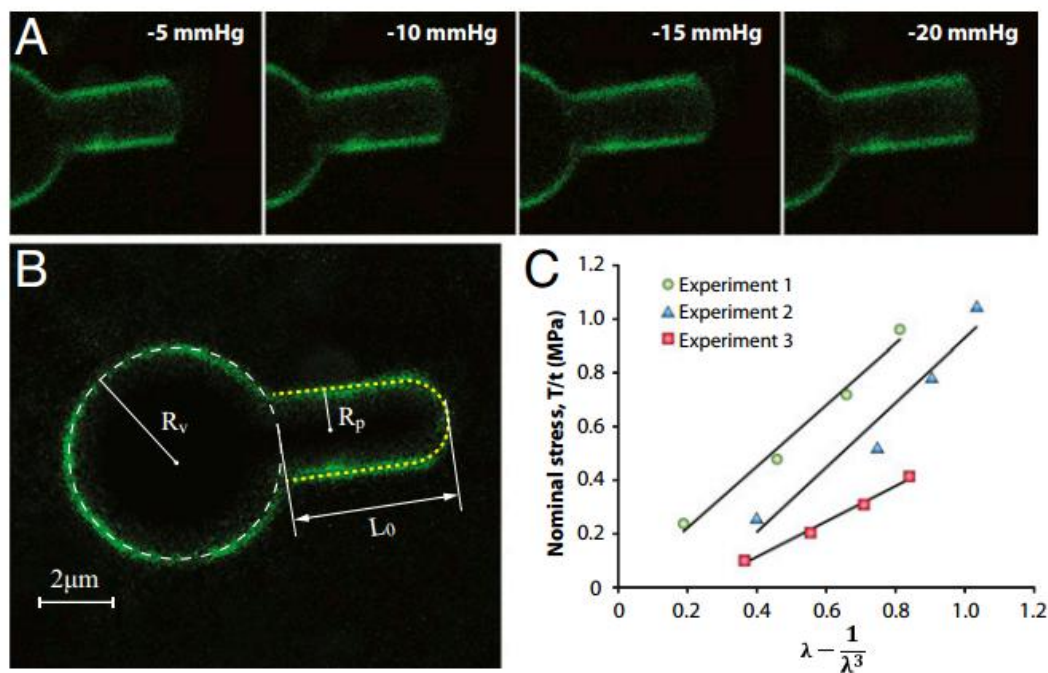
Figure 1.2 Cell-attached patch fluorometry experiments by four negative pressure steps[7].

Chang et al described a novel high-throughput magnetic tweezers-based 3D micro-channel electroporation system which could realize the gene therapy, regenerative medicine, and intracellular detection of target mRNA[8]. This method is characterized by direction-control and wide measuring range. Figure 1.3 shows that magnetic labeling and the low voltage pulses do not damage the cell membranes. However, the low resolution of handling restricts the application of MT.
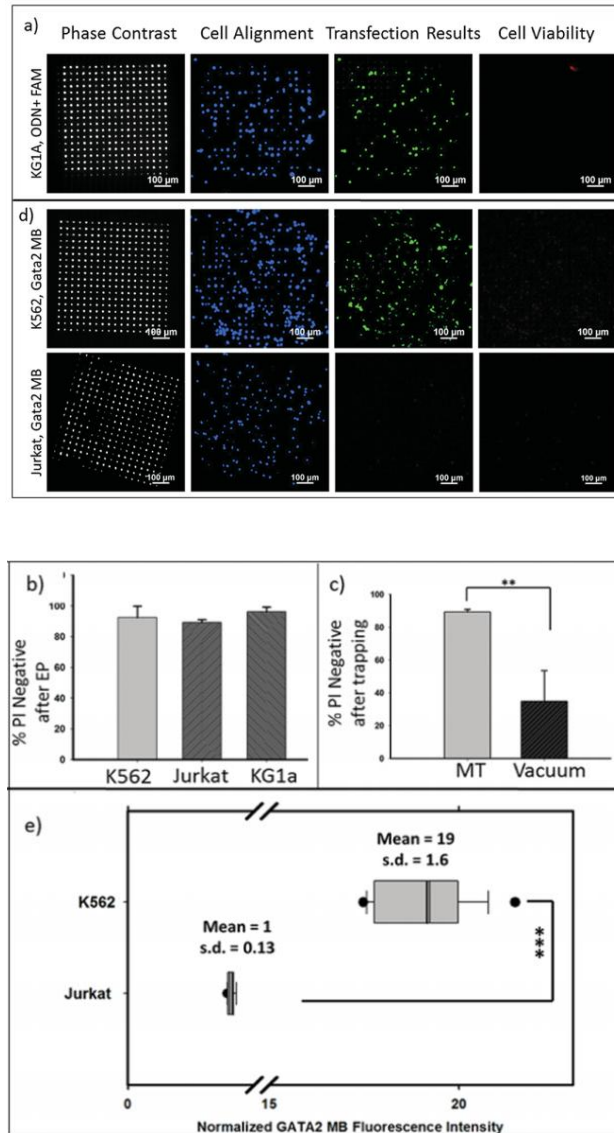
Figure 1.3 High-throughput cell transfection on 3D micro-channel electroporation[8].

Mirsaidov et al demonstrated a new method with the potential to capture multi-cellular organism for creating the synthetic tissue with submicron precision[9]. They used SLM (Spatial Light Modulator) to form a heterogeneous optical tweezers array in a 30mm×30mm×45mm volume where cells were conveyed. The optical tweezers array was induced through a microfluidic network for creating the synthetic tissue, and time-multiplexed manipulation was used to organize cells into a complex array, as shown in Figures 1.4. The optical technology has been actively

developed to play an important role in bioscience due to its advantages of remote manipulation and less damaging. The OT belongs to remote nano handling and recently has been developed as a powerful technique for the cytology studying with less damaged but it has the disadvantage of inefficiency in cells trapping.
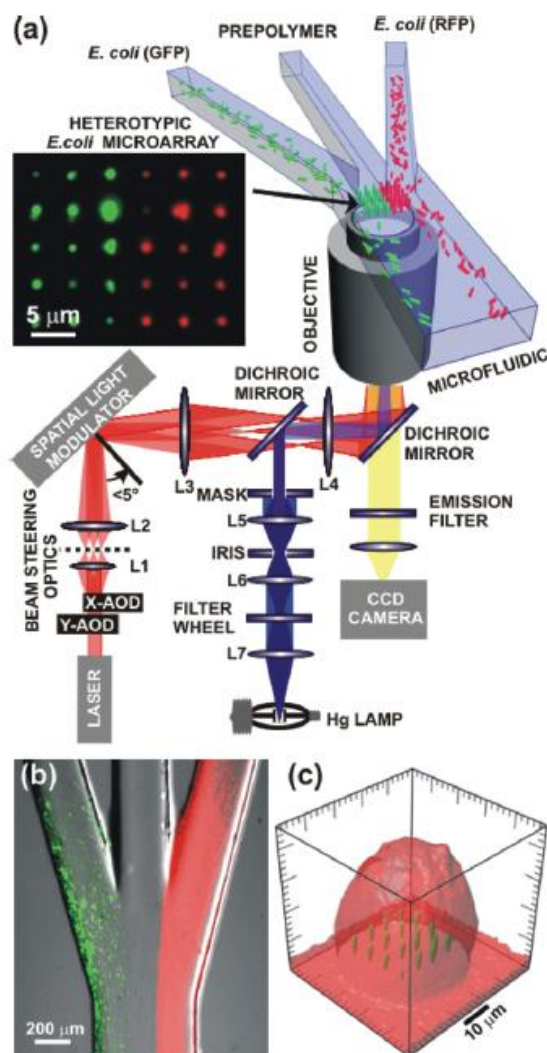
Figure 1.4 Schematic diagram of multiple, time-shared optical tweezers in a micro-fluidic network[9].

Compared with others, AFM has both nano handling and measurement functions. It is a high resolution device that is used not only for direct microscopy, but also for the manipulation of

biological cells in culture, which is good for the cell applications[10][11][12]. Shen et al. presented a new method to measure the single cell stiffness based on AFM[13]. Yang et al. used the AFM-based nanorobotic system to identify the mechanical marker for the apoptosis process[14]. From the AFM scanned images, they found that normal adjacent cells were closely linked and the cells became softer when they lost the cell-cell adhesion due to the acantholysis which led to apoptosis. The unique potential of AFM has been well recognized in biological research[15].

1.2.2 Nano Measurement Techniques of Biological Cells

Not only the mechanical properties but also the reciprocity of cell surface molecules plays a crucial role in cytology research. Many of these reciprocities are operating together with others, collaborating in the regulation of cell functions, such as the transportation of many kinds of substrates across membranes, signal transduction between two cells and cell adhesion. Moreover, an exceptional nano structures will also be emerged, for instance, the distribution of the surface proteins with sugar molecules and their density, size, direction of functional groups and connections. Thus, to explore the reciprocity of cell surface molecules and the relevant nano structures will be significant in the understanding of the pathophysiology of malaria. An integrated high-throughput approach will be needed. which is able to perform the high-resolution measurement, and sensitive and effective analysis of cells in the physiological condition and effective analysis.

There are currently several common instruments used for nano measurements including OM (Optical Microscope), EM (Electron Microscope), CLSM (Confocal Laser Scanning Microscope) and SPM (Scanning Probe Microscope). Shtrahman et al used OM with multifocal fluorescent probes to demonstrate the fast optical recording of neuronal action potentials could be used to reveal the Ca^{2+} transients resulting from APs in neurons labeled in millisecond resolution[16]. OM is one of the most powerful tools for the amplification in cytology as its convenient and efficient operating, but the image is still affected by the limited resolution and the sample thickness.

Narayan et al demonstrated several advantages in scanning electron microscopy and used it to obtain three-dimension images of HIV (Human Immunodeficiency Virus) cores[17]. However, EM is very expensive to build and maintain due to the requirements of complex special services and stable environments. The samples have to be placed in vacuum with a complicated sample preparation except the environmental scanning electron microscope, which allows the sample to be viewed in wet conditions and low pressure (up to 20Torr or 2.7kPa)[18]. CLSM is a new scanning imaging technique which can obtain high resolution images with the depth selectivity. The interior structures of sample can be imaged by three-dimensional reconstructions. It is widely used in the biological science and nano crystal imaging and spectroscopy. It is often combined with fluorescent markers to obtain the three-dimensional structures of biological samples, the communication between two cells, the dynamic analysis of calcium ions and pH values inside cells[19]. Moreover, it can also observe submicron particles which is below to the resolution limit of the optical microscope. In the past years, AFM has been increasingly used for exploring the surface properties of cells on the nano scale. It uses a physic probe as a sensor to image the surface of samples and reaches an impressive atomic resolution by the interaction force between the tip of probe and the sample. Its transverse resolution can be up to 0.1nm and the longitudinal resolution 0.01nm, which is more than one thousand times higher than the resolution of optical microscopes. Compared with other microscopes, AFM has many advantages as shown in Table 1.

Table 1.1 Comparison of nano measurement techniques.

	AFM	OM	EM	CLSM
Resolution	0.1nm/0.01nm	200nm	0.8-20nm	150nm
Actuator	PZT	Step motor	Magnetic coil	Laser rotating mirror
Working environment	Atmosphere and liquid	Atmosphere	Vacuum Wet environment and low pressure	Atmosphere
Measurement objects	Various materials	Various materials	Electrically conductive materials	Various materials
Dimensions	3D	2D	2D	3D

In conclusion, AFM can work in different environments with sub-nanometer resolution and image various materials in three-dimensions. It has been successfully applied in cytology research. Chen et al used AFM to investigate the toxicity of dauricine on daudi cell of B lymphoma cells[20]. Experimental results showed that the control cells were round and the surface was smooth after treated with dauricine. Figure 1.5 shows the topological morphology of daudi cells between control group and drug group.
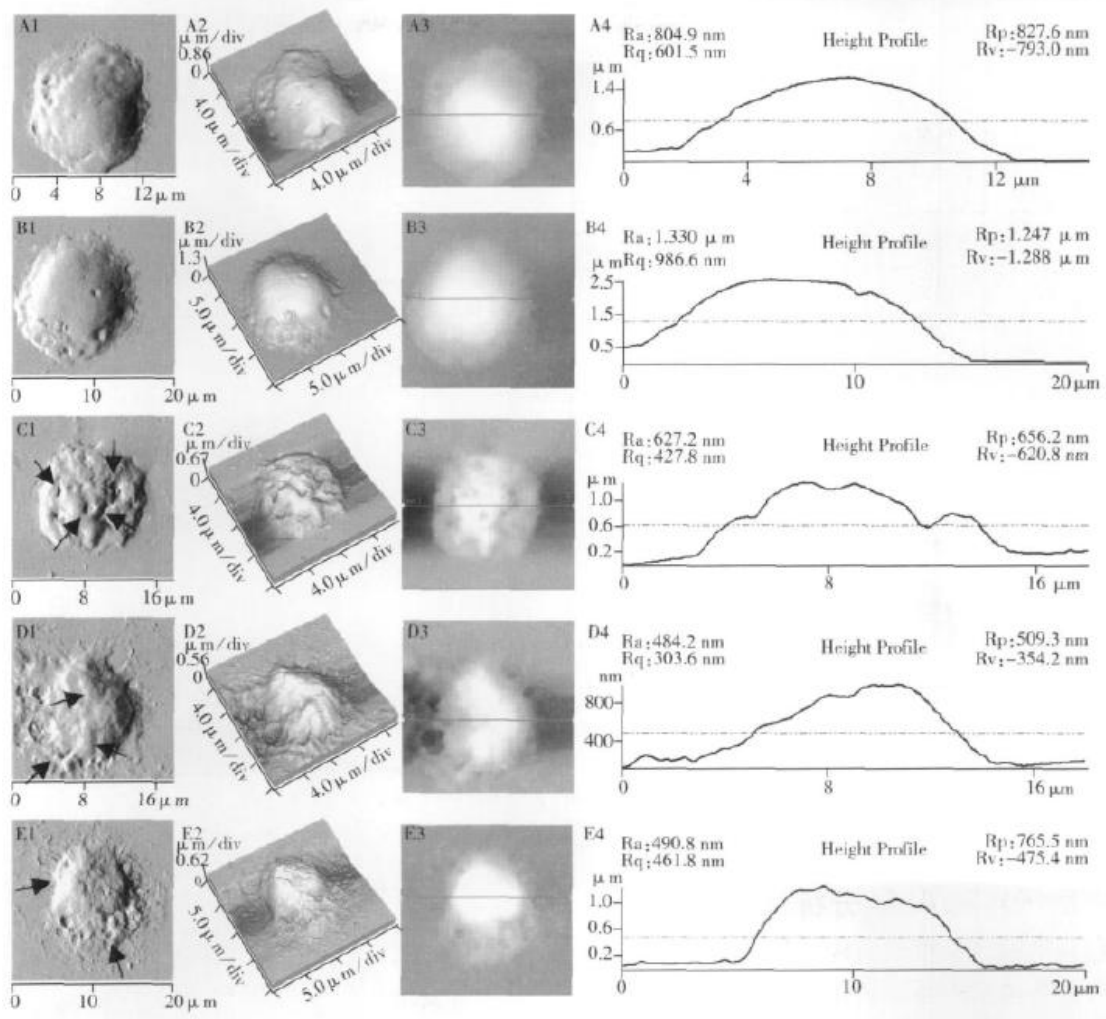
Figure 1.5 Topological morphology of daudi cells detected by AFM[20].

Wang et al used AFM to observe the surface of preadipocyte, and found that they were stretched with full of parapodiums, and different sizes of plaques and protuberances were spread on the cell membrane[21]. Sun et al used AFM to detect the dynamic growth of human umbilical cord mesenchymal stem cells, and found that the adherent cells showed various shapes including spindle, polygonal and fibroblast-cell-like shapes[22]. Moreover, the sizes of mesenchymal stem cells were homogeneous. However, there is a lack of working time with AFM for biological applications in uncontrolled environments. Cells will be died after the imaging, and there is almost no report on the imaging of cells over the course of growth. For this reason, one of the aims in this

work is to use a novel method of liquid-AFMs which can work in culture. The probe tip is totally put into the culture during scanning, and real-time visual feedback needs to be achieved for the cell observation. Hence, there is a rising consensus among researchers that a single tool is not enough to support them for further investigation. They have tried to add more interfaces or combine with different instruments to solve those problems in multi-functions.

1.2.3 Hybrid technologies of Biological Cells

Great efforts on different biological applications of AFM have been made by scientists worldwide in recent years. AFM has both nano handling and measurement functions. The applications of AFM instruments and other microscopes have shown the feasibility of nano instrument development, which will also result in an explosion in applications for biomedical and clinical translational studies[23]. Fatikow et al. developed a new system which combined with AFM, FIB (Focused Ion Beam), and HRSEM (High Resolution Scanning Electron Microscope)[24][25]. Figure 1.6 shows the automated AFM-based nano manipulation system. It was used to realize nano handling, analysis and structuring with the haptic feedback and SEM vision for the samples in the high vacuums or at 100% relative humidity environment.
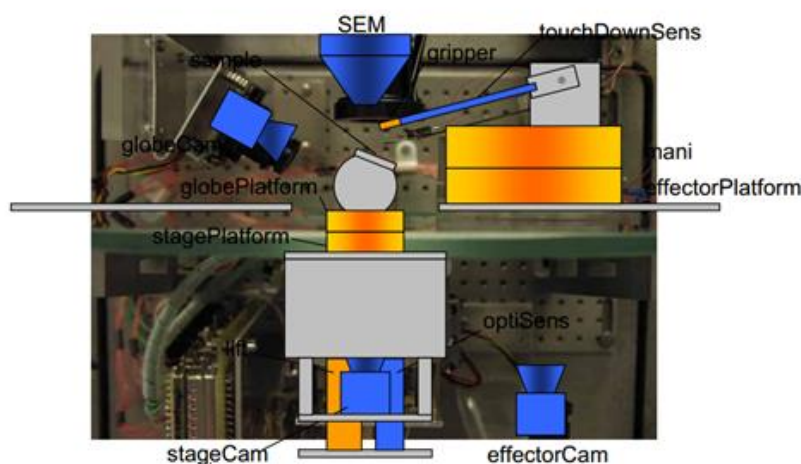
Figure 1.6 Schematic of the automated AFM-based nano manipulation system[24,25].

Trache et al. developed a technology that integrated AFM with FSD (Fast-spinning Disc) confocal microscope and TIRF (Total Internal Reflection Fluorescence) to analyse the mechanisms of living cells with high temporal and spatial resolution[26]. This system can be used in a broad range of applications in molecular dynamic research of adherent living cells, including cell surface topography, mechanical stimulation and optical imaging to the response in real-time, as shown in Figure 1.7.
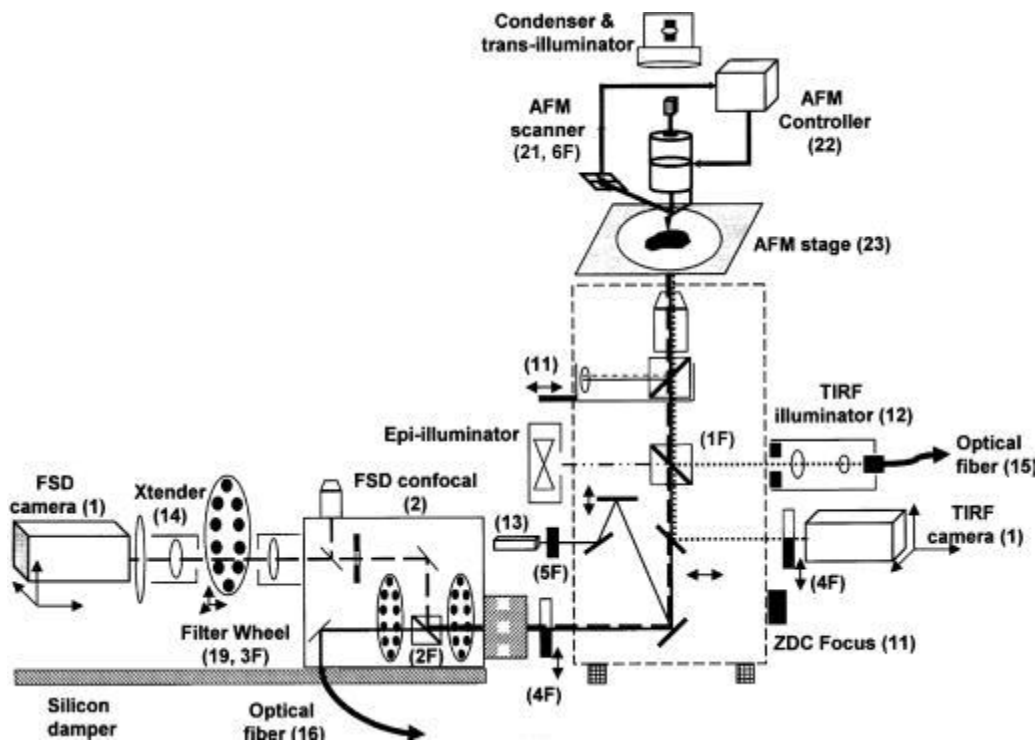
Figure 1.7 Schematic layout of the integrated system with AFM, TIRF and FSD[26].

There are other groups exploring these ideas as well. Ahmad et al. fabricated the bucking nano needle using the focused ion beam etching on a tip of a commercial available AFM cantilever in a developed system called an ESEM (Environmental Scanning Electron Microscope). It was used as a force sensor for the stiffness characterization of single cells[27]. A four-probe handling system

and visual feedback used with SEM for micro/nano object research was designed by the company Zyvex[28]. This system can be used for mechanical and electrical characterizations, and nano handling on the micro/nano scale. Pfister et al. and Doak et al. used CLSM to facilitate the coupled AFM to provide a new means of complementary 3D high resolution imaging and fluorescence imaging for biological cells[29][30][31].

However, there are some problems when applying robot systems to the manipulation, measurement and handing of cells. The first problem is the environment related to the living cells to be measured. The cells in most of experiments are usually cut into slices, and AFM is used in the air. For this reason, one of the aims in this work is to design a novel AFM which can be used in the liquid. The second problem is the effect of those micro/nano assembly machines which combine with the AFM. SEM is used in vacuum and environmental scanning, and may have huge thermal effects to damage the sample. CLSM and TIRF cannot be used for the handling and measurement of the forces of cells, and FIB is used in the manufacturing of surface. Therefore, the technique to explore the mechanical actions of optical fields to trap and manipulate neutral particles has led to a wide range of applications. This technique has been used to combine with the AFM to manipulate and study the properties of micron-sized dielectric particles, and it is only recently that this precise force measurement instrument has been applied to the study of biological systems. Liphardt et al integrated the AFM and OT to investigate the process while DNA (Deoxyribonucleic Acid) acted on the RNA of escherichia coli such as packages, folding and transcription[32]. Huisstede et al. developed a new instrument combined with the AFM and OT to investigate the interaction between the DNA and protein in single molecules, as shown in Figure 1.8[33]. Two traps created by AFM and OT allowed the bead-DNA-bead system to realize free movements, and the estimated experimental resolution was 15nm.
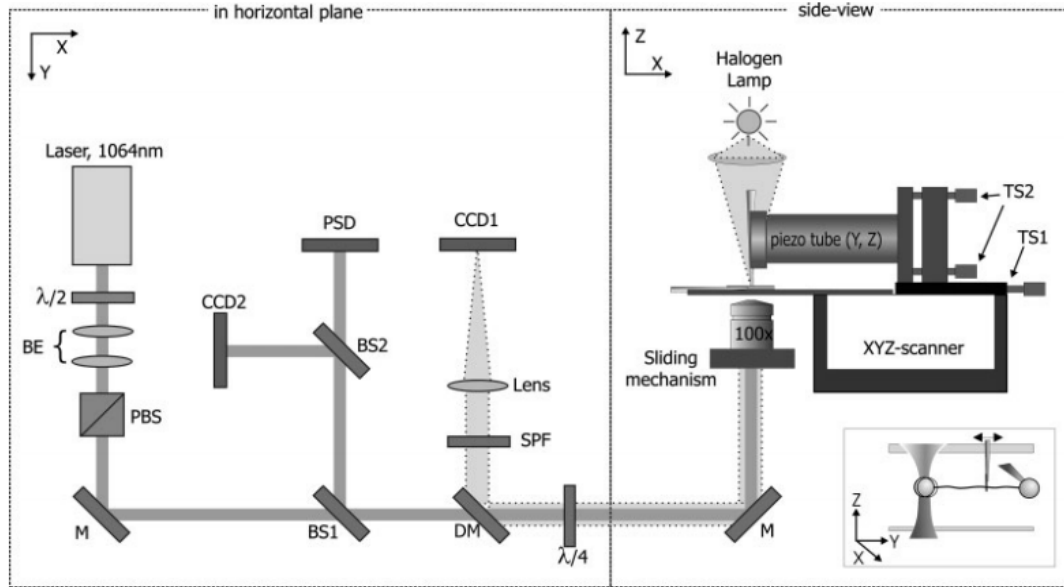
Figure 1.8 Schematic layout of the integrated system with AFM and OT[33].

However, the efficiency of optical tweezers application combined with the AFM is not high. To solve this problem, there are two main methods for multiple optical trapping: the first one uses the high numerical aperture objectives based on strongly focused beams[34][35]. The other one based on interference methods is used when particles are trapped by an interference field[36][37][38][39]. Among them, LBI (Laser Beam Interference) is a promising technology for the volume creation of large regular array of optical traps with easily constructed and inexpensive micro-lenses. This method does not require strongly focused beams and provides a way to generate periodical and quasi-periodical optical traps with the adjustable width and less damaging, so that simultaneous spatial manipulation of a large number of particles can be achieved.

From the literature review of nano handling and measurement techniques of biological cells, an integrated system including a liquid-AFM and OT based on laser beam interference has several advantages compared to other techniques, and they are described in the following points.

1) To develop a liquid-AFM which can work in culture:

• It provides true 3D surface topographical information of the living cells in vitro.

• It can image the cell surface with nano resolution, and up to 0.01 nm vertical resolution.

• It allows measuring various physical properties of the biological samples, such as elasticity, adhesion, hardness and friction.

2) To design a multiple optical tweezers system:

• It can remotely manipulate the biological cells on the nano scale.

• It provides measurable forces and distances suited for cells dynamics.

• It allows moving and selecting multiple living cells.

• The system can work in normal buffer conditions.

1.3 Aim and Achievements of the Thesis

1.3.1 Aim and Objectives

This work aims to develop a new system and new techniques which will be able to visualize and quantify the dynamics of living cells in culture on the nano scale and accurately measure the interaction force on the surface of biological cells at the molecular level. An integrated system including a liquid-AFM and OT based on laser beam interference is developed because of their numerous significant advantages. To realize the development of the proposed design, several objectives are set-up and they are described in the next chapters.

❑   To conduct a comprehensive literature review of the techniques of nano handling and measurement of biological cells in culture and analyse their advantages and disadvantages.

❑   To design a liquid-phase nano handing system which includes a human-machine interface system, actuators, sensors, a platform and a liquid cell.

❑   To perform an experiment of PSD detection and nano force modelling with correction parameters in culture and achieve better quality of images (decreasing the overshooting and minimizing system errors) for cells by PID controller.

❑   To carry out the cellular shear adhesion force measurement by liquid-AFM and study the mechanical properties of cells based on the liquid-AFM.

❑   To design an optical tweezers based on laser beam interference and perform the capture experiment of biological cells.

❑   To break through the limited size generated by multiple optical tweezers and achieve nano handling and separating cells by this system.

❑   To analyse the experimental results, and recommend further work.

1.3.2 Achievements

This work contributes to an integrated system combination of liquid-AFM and OT based on laser beam interference for the nano handling and measurement of biological cells in culture. A novel method of AFM measurement was developed in culture, and the probe tip is totally put into the culture during scanning. A specific liquid cell with input/output ports and a glass on the surface of the liquid could remove the surface movement of liquid and achieve the reliable handling and measurement of biological cells for a long time. In experiments, the mechanical properties and the cellular shear adhesion forces of two types of living cancer cells were obtained with the liquid-AFM. With the investigation of optical tweezers, a simplified vectorial ray-tracing method combine with the RO (Ray-Optics) model and integrated with the positioning in the *Z* direction was presented for calculating forces. In addition, the capture experiment of biological cells based on single optical tweezers and the capture and sorting of multiple cells by polarization-controlled three-beam interference optical tweezers were achieved successfully. These findings pave a way

for the improvement in medicine for the cell research.

During my PhD work, 2 journal papers and 2 conference papers have been published. Some published results are described in the thesis. Chapter 3 covers the work of "Development and Optimization of Liquid-AFM". According to the PID controller, the system needs to implement the real-time control of the system with three parameters in the imaging of cells. Chapter 4 discusses the work of "Cells Imaging and Mechanical Properties Study of Cells Based on Liquid-AFM" and "Cellular Shear Adhesion Force Measurement Based on Liquid-AFM" which is submitted in the journal of medical and biological engineering. Chapter 5 covers the work of "Force Characterization of Biological Cells Based on Single Optical Tweezers". Chapter 6 discusses the work of "Capture and Sorting of Multiple Cells by Polarization-controlled Three-beam Interference". My publications are shown below.

Journal papers:

1. Yu Hou*, Zhen Hu, Zuobin Wang and Zhankun Weng. Interference Lithography Detection System in Large Area. China Science Paper, 10(8):948-951, 2015.

2. Yu Hou*, Zuobin Wang, Dayou Li, Renxi Qiu, Yan Li and Jinlan Jiang. Cellular Shear Adhesion Force Measurement by Atomic Force Microscope. Journal of Medical and Biological Engineering, accepted.

3. Yu Hou*, Zuobin Wang, Yaowei Hu, Dayou Li and Renxi Qiu. Capture and Sorting of Multiple Cells by Polarization-controlled Three-beam Interference. Journal of Optics, published.

International conference papers:

1. Yu Hou, Zuobin Wang, Jiaojiao Song, Dayou Li. Yong Yue and Carsten Maple, Magnetic Surface Patterns Made by Non-Destructive Laser Interference. Proc. IEEE 3M-NANO, 2013.

2. Yinbao Lei, Zuobin Wang , Jia Xu, Jinjin Zhang, Dapeng Wang, Yu Hou*, Yong Yue, and Dayou Li., Determination of Two-dimensional Phase Shifts in Three-beam Laser Interference Patterns. Proc. IEEE 3M-NANO, 2012.

Chapter 2

Fundamental Theories and Methodology

2.1 Fundamental Theories and Structures of AFMs

The precursor to AFM, the STM (Scanning Tunneling Microscope) was invented by IBM (International Business Machines Corporation) scientists Gerd Binnig and Heinrich Rohrer in the early 1980s at IBM Research[40]. Moreover, they shared the 1986 Nobel Prize in Physics for the invention. In 1990, Eigler et al used STM to realize the first manipulation of atoms[41]. 35 xenon atoms were manipulated into patterns using STM to form the initials "IBM", and it began the age of nano manipulation science and technology. This event means the resolution can be reached repeatable at the atomic level. Binnig at el developed the AFM based on STM with atomic resolution[42].

In the early implementation, AFM was developed to realize the imaging of non-conductors which was not able to be achieved by STM. However, some nano particles were usually moved by the probe as well. This phenomenon had inspired many studies by scientists. The AFM was used both as a tool for the imaging of samples on the nano scale and as a force sensor for the handling and measurement. After that, the unique potential of AFM has been well applied in interdisciplinary areas, which covers many research fields including physics, chemistry, microelectronics, materials science and especially the biomedicine. AFM is today a crucial tool for the development of nano science.

2.1.1 Physical Mechanisms of Atomic Force

AFM is the most rapidly developed technique in imaging in the last two decades. A physical probe is used as the sensor to image the surface of samples and reach a rather impressive atomic resolution by the interaction force between the probe tip and the sample. When the gap between the AFM probe and the sample is small enough, there will exist different action forces[43]. Based on the action scope and the strength of the forces, they can be divided into the long- range force and short- range force. Generally if the distance from the sample is longer than 10nm, the force on the probe is called as the long-range force. If the distance from the sample is less than 10nm, the force on the probe is called as the short-range force.

1. Long-range force

The long-range force mainly indicates the action force when the distance from the probe tip to the sample surface is more than 10nm, such as electrostatic force and magnetic force. A complete theory is formed for these long range forces. Figure 2.1 mainly analyses the rotary and symmetric probe system.
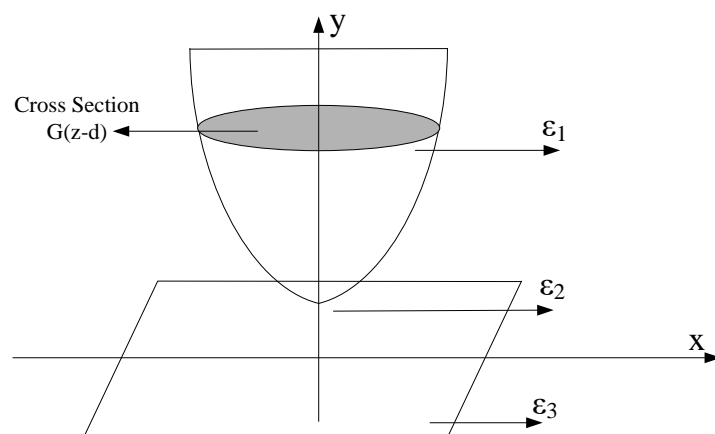
Figure 2.1 Schematic diagram of the interaction between the sample and the probe. ε_1 is the dielectric constant of probe, ε_2 is the dielectric constant between the sample and the probe, and ε_3 is the dielectric constant of sample.

20

As show in Figure 2.1, owing to the smooth sample surface and the ideal rotary and symmetric probe tip, the force acting on the unit volume of the probe can be obtained by the integral of Lifshitz theory, and the Lifshitz theory is expressed as[44]

$$f(z) = \frac{\hbar}{4\pi^2 c^3} \int_0^\infty \int_1^\infty p^2 \zeta^{\frac{3}{2}} \times \left[\frac{1}{\alpha \exp(x) - 1} + \frac{1}{\beta \exp(x) - 1} \right] dp d\zeta \qquad (2.1)$$

where $\hbar$ is the reduced Planck constant, c is the speed of light, p and ζ are the loss factors of two dielectric constants. α and β are the constants.

Then, Eq. (2.1) can be integrated to obtain the force acting on the probe[44].

$$F(d) = \int_d^\infty f(z) G(z - d) dz \qquad (2.2)$$

where G(z-d) is the function of the force acting on the probe with the distance between the probe and the substrate. From Eqs. (2.1) and (2.2), the acting force between the probe and the sample can be deduced in a common case, but it is difficult to have the parsed solution of two equations in actual cases. Only the numerical values can be obtained with computers. Generally the acting force between the probe and the sample under the semispherical conditions with the probe tip can be expressed as[45]

$$F(d) = -\frac{A}{d^m} + \frac{B}{d^n} \qquad (2.3)$$

2. Short-range force

Generally the atom is a stable neutral electric system. When two atoms approach within several nanometers, the external electronic clouds of the atoms will deform due to Coulomb electrostatic force. The attraction force will first occur between the two toms based on the distance from remote to near. When the two atoms approach to each other to some extent, the overlapping of electronic

clouds and the interaction between the neutral charges will generate repulsive force. Provided that the atoms are rigid small balls, the total potential energy of the system can be represented approximately as[45]

$$V(d) = -\frac{A}{d^m} + \frac{B}{d^n}$$

(2.4)

Then, the acting force between the two atoms can be expressed as[45]

$$F(d) = -\frac{\partial V}{\partial r} = -\frac{mA}{d^{m+1}} + \frac{nB}{d^{n+1}}$$

(2.5)

2.1.2 Analysis of Forces on the Probe

When the probe approaches to the sample, it will be generally suffered from different forces. The types of forces under the air conditions and the liquid environments are different, as shown in Table 2.1. The long-range forces mainly include the liquid film damping, electrostatic force and surface tension (capillary force). The short-range forces mainly include the Van der Waals force and Coulomb force. These acting forces will be described as follows.

Table 2.1 Main forces act on the probe when it approaches to the sample.

Force		Range	Types	Note
Long-range force	Liquid film damping	~10μm	Resistance	Exist in the tapping mode
	Electrostatic force	0.1-1μm	Attractive force or repulsive force	Relation to the type of sample
	Surface tension (Capillary force)	10-200nm	Attractive force	Exist in air conditions
Short-range force	Van der Waals force	0.1-1nm	Attractive force	
	Coulomb force	0.01-0.1nm	Repulsive force	

1. Liquid film damping

The liquid film damping is a damp film to obstruct the probe motion[46]. Generally when the probe approaches to or keeps away from the sample, the probe will suffer from a resistance at about 10μm from the sample, the resistance is called as the liquid film damping. When the probe rushes down, the air between the probe and the sample will be instantly compressed and will generate a repulsive acting force. When the probe rushes up, the air between the probe and the sample will generate the vacuum, which will lead to "an attractive force". This obstruction only occurs in the vacuum area. This force will not affect the contract mode of AFM according to the action range.

2. Electrostatic force

The long-range force and electrostatic force are frequent in AFM detection due to the influences from the charge density on the surface of the probe and the sample. Generally, the electrostatic force exists within the range of 100-1000nm from the probe to the sample[47][48]. The electrostatic force is attractive or repulsive depending on the different natures of the sample material. To study the electrostatic force, the scientists specially developed the electrostatic microscope. The electrostatic force may disturb AFM under the non-contact mode due to its acting scope. When it happens, the ion sources with the reverse polarity will be used to eliminate the influences of the electrostatic force in the acting area. In addition, the electrostatic force mainly exists under the air conditions and appears very weak in the liquid environment, so it can be ignored in liquid-AFMs.

3. Liquid surface tension

The liquid surface tension is called as the capillary force and belongs to the long-range force. The steam in the air will form 5-10nm water film on the surface of the sample[49]. When the probe approaches to the sample, the liquid surface tension will exist at 10-200nm from the probe to the sample according to the thickness of the water film. The liquid surface tension is an attractive force. If it is strong, it can pull the probe into the soft sample and lead to some damage. The liquid surface tension occurs between the sample with the water film on the surface and the probe tip

without water film on the surface. At this time, the sample and probe can be soaked in the solution to eliminate the action, or the force is measured in the vacuum. This attractive force affects the contact mode of AFM under the air conditions and will not be considered in the liquid environment.

4. Van der Waals force

When the probe approaches to the sample, the probe will suffer from the first short range force, which is called as Van der Waals force. Although the Van der Waals force is very weak, it is the main acting force for AFM imaging. The Van der Waals force exists in the gas phase, liquid phase and vacuum, and is very sensitive within 0.1-1nm from the sample[50].

5. Coulomb force

When the distance between the probe and the sample reduces to about 0.1nm, they will approximately touch each other. In this case, the atomic electron cloud will be overlapped and deformed on the surface of the probe and the sample, and will exclude each other[49]. The acting force is 10^{-8}-10^{-11}N. This acting force will exist in the air conditions or liquid environments and become an important part of the short range force to the probe under the tapping mode and the contact mode.

Besides the above forces, the probe will be suffered from the double electron layer force, the hydrophobic force and hydrated force which depend on the influences from different samples. Moreover, due to the different materials of probes and the different factors in the liquid environment, the probe may generate the compression force, the cutting force and the friction on the *XY* plane during scanning.

2.1.3 Principle of Atomic Force Microscopes

The AFM scans the samples based on the tip of the probe installed on the cantilever in an AFM system, as shown in Figure 2.2. The acting forces between the sample and probe (repulsion force or attractive force) change continuously in scanning, and the corresponding cantilever will be deflected. The optical lever is used to magnify and reflect the laser beam off the cantilever to the PSD (Position Sensitive Detector). After the photoelectric conversion and processing, the signals showing the sample height will be delivered to the computer for processing and be restored to the sample surface topography in real time. The height of the nano displacement platform is controlled via the feedback system to keep the constant acting force between the sample and the probe.
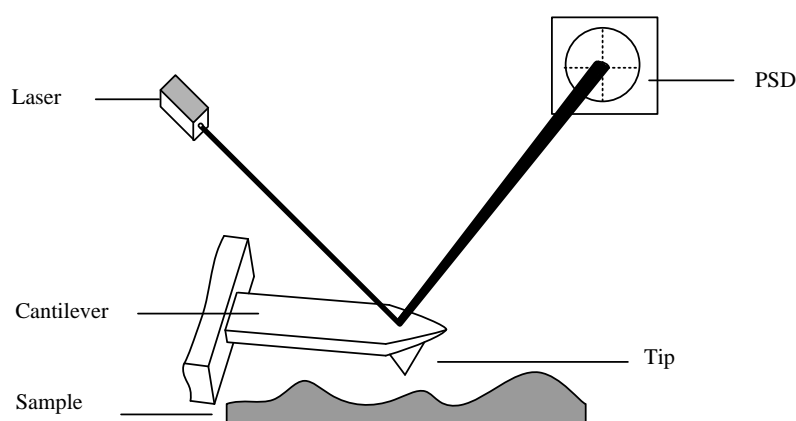
Figure 2.2 Schematic diagram of the force detection on the cantilever.

2.1.4 Operation Modes of Atomic Force Microscopes

Multiple different operation modes were developed according to the distance between the probe and the sample and the detected force in imaging during the evolvement for the past decades. The most common operation modes are the contact mode, non-contact mode and tapping mode, as shown in Figure 2.3. The three operation modes are different, and have different operation

principles. The following part briefly shows the three operation modes.

Mode	Contact mode	Non-contact mode	Tapping mode
Diagram			

Figure 2.3 Schematics of the operation modes of AFM and the corresponding imaging results.

1. Contact mode

From Figure 2.4, we can easily find that the attractive force is generated between the probe and the sample when the probe approaches to the sample[51]. With the decrease of the distance between the probe and the sample, the probe will suffer from repulsion force between atoms. When the repulsion force offsets the attractive force, the atoms will contact each other.
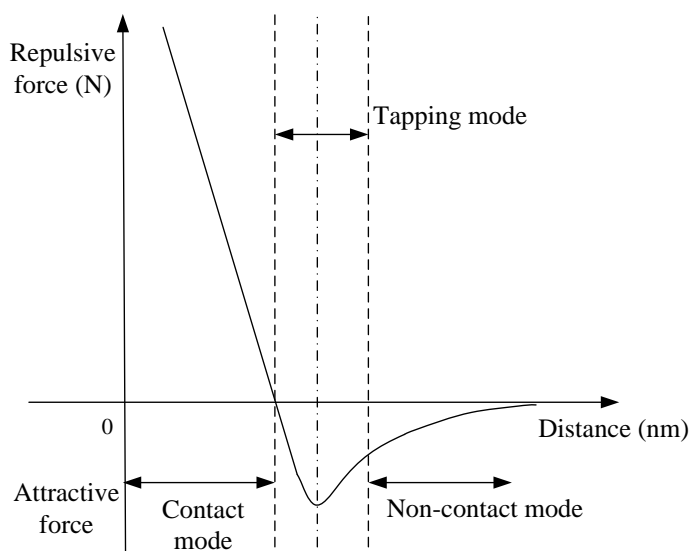
Figure 2.4 Relationship of the force and the distance, and the corresponding operation modes[51].

26

The contact mode is also called as the repulsion force mode. The probe also slightly contacts the surface of the sample and slides in scanning in this mode. Certain repulsion force exists in the contact part between the probe and the sample. The cantilever will have a large upward deviation due to the force from the probe, so that the AFM can obtain high-quality scanning images. To ensure that the AFM probe does not damage the sample, the repulsion force between the probe and the sample keeps about 10^{-7}N[51].

When people study the probe scanning process in the AFM contact mode in liquid, it is found that the routes are not fully repeated and the "jump" phenomena will occur, as shown in Figure 2.5(B).

In Figure 2.5(A), when the probe approaches to the sample, the probe will first suffer from about 10^{-10}N attractive force along the route A→B. The attractive force is very weak, so the cantilever does not deflect. When the probe reaches Point B, the attractive force and repulsion force of the probe will be equal and reverse, so they will be offset. When the probe moves along the route B→C, the repulsion force will gradually increase and the cantilever will deflect upward. In Figure 2.5(B), when the probe keeps away from the sample, the moving route of the probe is not fully overlapped with the route in Figure 2.5(A). The forces on the probe will be contrary in the routes C→B and B→C. When the probe keeps away from the sample, the repulsion force will become smaller. The upward deflection of the cantilever will become smaller and the cantilever will reach the balanced state at Point B. The probe will suffer from the increasing attractive force in the route B→D. The cantilever will deflect downward and the probe also suffers from the increasing elastic force from the cantilever. When the probe moves to Point D, the elastic force to the probe will be larger than the attractive force, so the probe suddenly breaks away from the sample and jumps to Point A from Point D. It will generate a "jump".
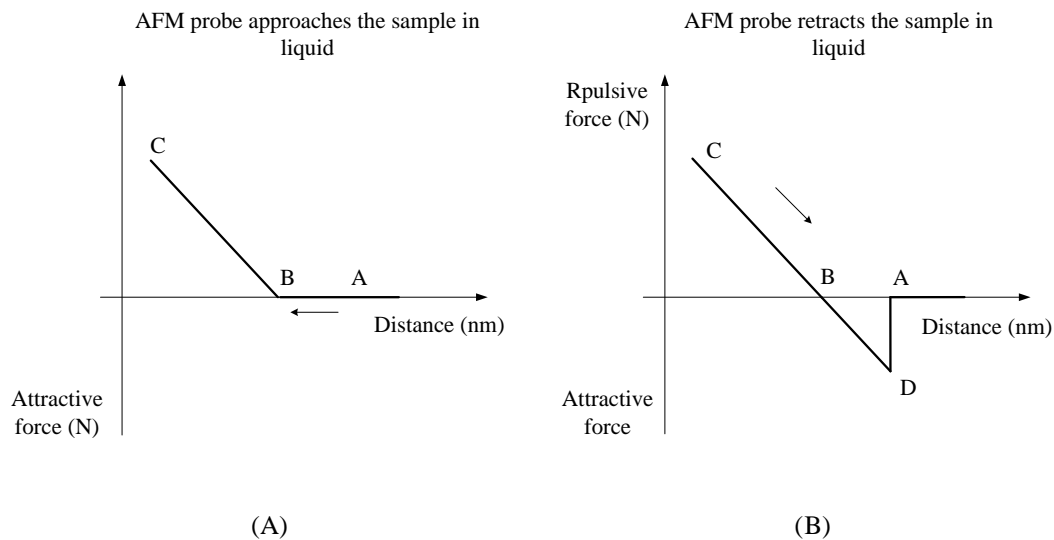
Figure 2.5 Moving route of the probe when it approaches the sample and retracts. (A) AFM probe approaches the sample in liquid. (B) AFM probe retracts from the sample in liquid.

The contact mode will differ during operations under different environmental conditions. The sample will condensate a 5-10nm water film on the surface under the air conditions. When the probe enters this area, the probe will be attracted by the liquid surface tension of the steam. In addition, the electrostatic (attraction) force should not be ignored. The movement of probe will generate some forces which may damage the sample in scanning in this mode (E.g. shear and friction). The forces may even affect the AFM imaging quality and could not truly reflect the sample pattern. When the contact scanning is performed in the liquid environment, although the electrostatic force and liquid surface tension are not considered, the probe may deform, move or damage the sample, and even affect the imaging quality of the AFM.

The contact mode indicates the operation in contact with the sample, so the sample under the test should be solid.

2. Non-contact mode

The probe does not directly contact the sample surface in the non-contact mode. The probe will

scan with 1-10nm amplitude at 5-10nm above the sample[52]. The operation mode is contrary to the contact mode. The probe does not contact the sample, so the non-contact mode will not damage or pollute the samples, and no special requirement for the sample rigidity is needed in this mode.

The image is formed in the non-contact mode by detecting van der Waals forces between the probe and the sample. The gap between the probe and the sample is controlled by keeping the stable resonance frequency of the cantilever or constant amplitude during scanning. Based on the vibration theory, vibration is very sensitive to the force change. In the non-contact mode, the probe approaches to the sample at the resonance frequency. The probe frequency changes due to the acting force. The change of the recording force can be detected by detecting the amplitude change. The theoretical analysis is described as follows.

The vibration equation of the cantilever in the operation mode is expressed as[52]

$$z'' + 2\gamma\omega_0 z' + \omega_0^2 z - F_0 \sin(\omega t) = 0 \tag{2.6}$$

The relationship between the amplitude of cantilever and the drive frequency can be written as

$$\begin{cases} A = \dfrac{A_0(\omega_0/\omega)}{\sqrt{1 + Q^2(\omega_0/\omega - \omega/\omega_0)^2}} \\ \omega_0 = C\sqrt{k} \end{cases} \tag{2.7}$$

where A is the probe amplitude, A_0 is the probe amplitude in the resonance frequency, ω is the shock excitation frequency, ω_0 is the resonance oscillation frequency of the probe, c is the function of the probe mass, k is the elastic constant of the probe, and Q is the quality factor of the probe.

When A is very small, the force f (acting force between the probe and the sample) can be regarded as the elastic force. The tangent gradient reduces by k, so ω_0 reduces to $\omega_{0'}$.

$$\omega_0' = c\sqrt{k - f'} \tag{2.8}$$

If $f' \ll k$, then

$$\Delta\omega = \omega_0 f'/2k \tag{2.9}$$

From Eqs. (2.8) and (2.9), the acting force f can be obtained via f' integral and f' can be expressed as[52]

$$f' = k\left(\frac{1 - 2a^2 + \sqrt{4Q^2(a^2 - 1) + 1}}{2(Q^2 - a^2)}\right) \tag{2.10}$$

As shown in Figure 2.6, to make the sensitivity of f' reach the maximum, the probe should be located in the steepest area of the relation curve between the amplitude and the shock excitation frequency (the frequency is 295kHz). In this case, the probe shock excitation ω_w can be obtained based on Eq. (2.8).

$$\omega_w \approx \omega_0(1 \pm 1/\sqrt{8}Q) \tag{2.11}$$

Then, f' reaches the maximum. Combined with Eqs. (2.6) and (2.8), the amplitude-frequency characteristic of the probe can be expressed as[52]

$$\Delta A = (2A_0Q/3\sqrt{3}k)f' \tag{2.12}$$
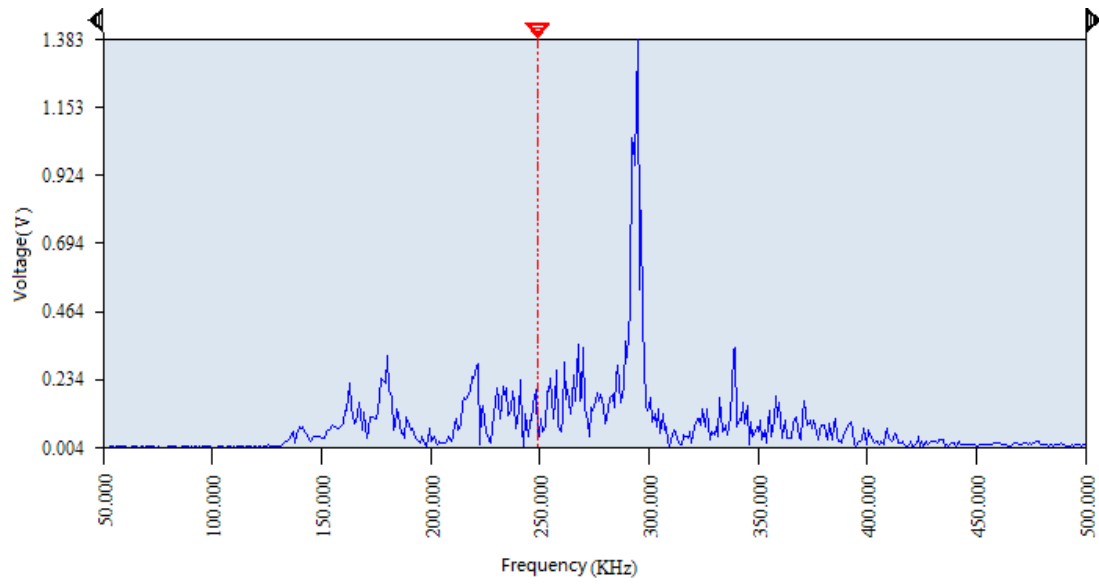
Figure 2.6 Relationship of the amplitude-frequency characteristic of the probe.

Based on the above description, the non-contact mode requires highly sensitive force detection device. This mode has low resolution and is not suitable for operations in the liquid phase environment.

3. Tapping mode

The tapping mode is called as the knocking mode or vibration mode. Like the non-contact mode, the tapping mode will generate vibration by exciting the cantilever based on the piezoelectric crystal. Its vibration frequency approaches to the resonance frequency of the cantilever (100-400kHz). The amplitude is over 20nm. The amplitude of the cantilever is larger in the tapping mode and it is within the Van der Waals forces and liquid surface tension as the attractive force, so the force acting on the probe includes the repulsion force and attractive force[53]. The total force is about 10^{-9}-10^{-12}N. The vibration probe will frequently contact the sample surface in operation, so the resolution can reach the nanometer magnitude in the contact mode. The damage to the sample due to the shear between the probe and the sample can be ignored due to the instantaneous contact. It breaks through the AFM restriction in the contact mode.

31
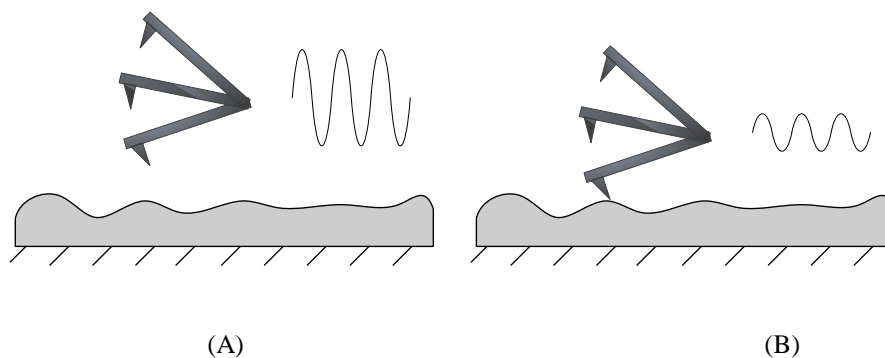
Figure 2.7 Schematic diagram of the tapping mode of AFM. (A) The vibration probe does not contact the sample. (B) The vibration probe contacts the sample.

As shown in Figure 2.7 under the air conditions, when the vibration probe does not contact the sample, its vibration is "free" vibration with the full amplitude. When the vibrating probe contacts the sample, the probe's amplitude will reduce due to repulsion force and the probe is forced to vibrate. The cantilever will deflect upward, and the detector will obtain the change of the amplitude. Then, the stable amplitude of the cantilever is kept via the feedback system, and the sample topography is obtained. The specific process is shown in Figure 2.8. The probe approaches to the sample along the route A→B and will be suffered from the attractive force between the probe and the sample, so its vibration frequency will reduce slightly and its amplitude will also reduce. When the probe moves to Point B (namely the gap between the probe and the sample is the amplitude of the probe), the probe can contact the sample surface. At this time, the acting force between the probe and the sample mainly includes the repulsion force. When the probe continues forwarding along the route B→C, the probe amplitude and distance are linear like the contact mode. If the amplitude increases, the knocking force between the sample and probe will affect the amplitude. When the probe reaches Point C, its amplitude approaches to zero. If the probe continues forwarding to Point D, the cantilever will deflect upward.
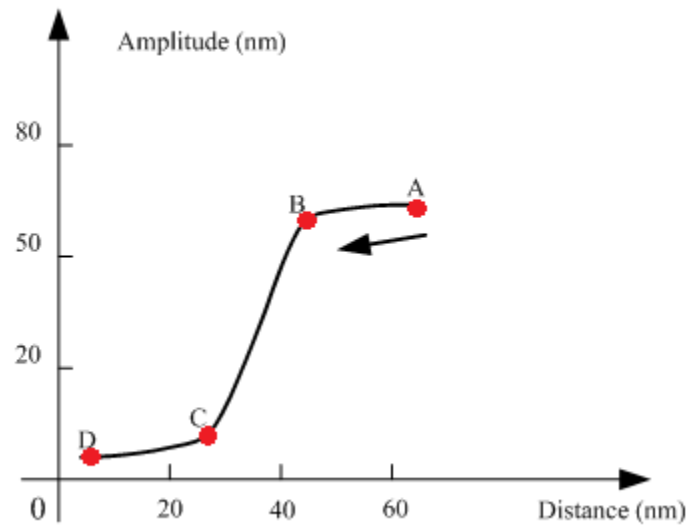
Figure 2.8 Relationship between the distance and the amplitude when the probe approaches to the sample.

In the tapping mode, it is difficult to calculate the amplitudes of different points on the probe surface under actual conditions. In addition, the tapping mode is also applicable to the operation under the liquid phase environment. The liquid phase environment is close to the true physiological condition of the microbes such as cells, so this operation mode is extensively applied in the cytobiology.

2.1.5 Scanning Techniques

At present, there are many kinds of commercial AFMs in the world and the designs of their probes are diversified. However, each design of probe aims to pursue high resolution scanning images. Based on this purpose, under the fundamental principle of minimizing the load of piezoelectric scanner, the feedback speed and scanning speed in the *Z* direction are ensured and the linear scanning in the *X/Y* direction is realized. According to different designs of probes, the scan mode of AFM can be divided into two common modes[54].

Sample-Scanning AFM is referred to the SS-AFM. In this mode, the laser, QD (Four-quadrant Photo Detector) and probe are fixed. The real-time PZT control moves the sample on the *XY* plane and in the *Z* direction, and simultaneously obtains the sample topography.

Tip-Scanning AFM is referred to the TS-AFM. In this mode, the scanner drives the probe to scan the surface of sample, which is relatively static, simultaneously obtaining the sample topography. Moreover, compared with the SS-AFM, it needs to bring in a light path tracing system.

Sample scanning probe feedback sets the advantages of scanning and probe scanning in one. It applies the plate scanner to drive the sample to scan the *XY* plane, uses the *Z* direction PZT (Piezoelectric Transducer) to control the timely feedback of probe, and simultaneously obtains the sample topography.

Different scan modes have their advantages and disadvantages. In the thesis, the sample scanning mode was selected according to the experimental environment, difficulty level of realization, accuracy of measurement and sample size. The scanning path of AFM is the "*Z*"-shape which is described in Section 3.7.

2.2 Fundamental Theories and Models of Optical Tweezers

In 1970, Ashkin found that the focusing laser beam could pull the micro particles which had a higher refractive index in medium, to the focus of laser beam[55]. The dielectric micro particles were accelerated by the attractive force in the opposite direction generated by the argon ion laser. He displayed the motion of a particle restricted by the counter propagation laser beam in three-dimensions. In 1971, Ashkin and Dziedzic firstly realized the optical capture of dielectric microparticles under microscope. Subsequently, they developed a single-beam optical tweezers in 1986[56]. The optical tweezers can utilize the light scattering force to confront the gravity of microparticle and light pressure force of laser beam in the opposite direction, and to maintain the

stable vertical positioning of particles. Moreover, the gradient dipole force kept particles in the central positioning of Gaussian beams. At present, the single-beam optical tweezers have been used widely and could be used to research angular momentum light, thus to measure the internal stress of cells.

In the traditional single-beam optical tweezers, a high numerical aperture lens was used to focus the laser beam to a diffraction limit point, and then a single-beam gradient trap can be generated by the light gradient in the sample plane. Near the focus, the optical trap could capture the particle which the refractive index is higher than that of medium. All of particles with dimensions between nanometer and tens of microns, including insulated particles or small metallic particles and even animate particles, can be operated by optical tweezers. If a particle has the same refractive index with that of medium, the particle will not be attracted by light beam. If the refractive index of particle is lower than that of medium, the particle will be affected by a repulsive force to keep away from the light beam. In the last decades, the optical tweezers has been mature as an important tool in the fields of biology, physical chemistry and biophysics. Biologists are firstly aware of the potential of optical tweezers and use it to capture and operate micro-particles. In the biological field, the optical trap provides a new tool to operate microorganisms and cells. Different biological objects have been captured successfully, including viruses, bacteria, yeast cells and red blood cells[57][58]. Subsequently, the light gradient force and optical trapping potential have been extended to single-cell manipulation and single-cell sorting. Since there is less-damaged in the process of capturing particles with optical tweezers, optical tweezers becomes an important tool in biological studies[59]. Moreover, optical tweezers can be easily combined into existing commercial microscope systems.

Combined with new instruments, optical tweezers can play a greater role. For instance, together with an automatic mobile platform, optical tweezers could be used to select and separate different cells, and to perform the DNA manipulation[60][61][62]; together with a high-precision position

sensor, and the tweezers could be used to measure the biological force, as shown in Figure 2.9[63].
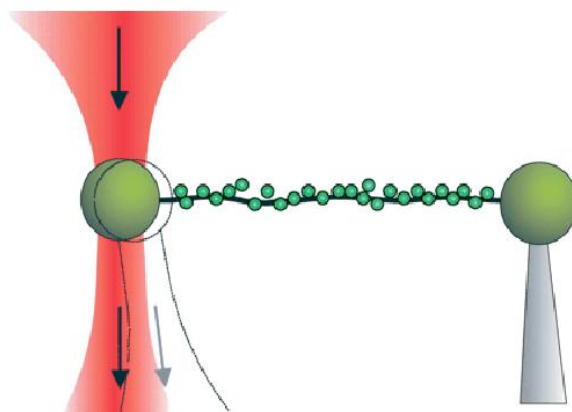
Figure 2.9 Optical tweezers were used to stretch the chromatin fibers[63].

2.2.1 Fundamental Theories of Optical Tweezers

In the single-beam optical tweezers, the laser beam can be focused in liquid through a high numerical aperture lens, and all particles near the focus with refractive property can be attracted to the focus.

In the basic optical tweezers, it contains a highly stabilized laser, high numerical aperture lens, beam expander, optical adjustment system and the tools for observing the capture of samples, as shown in Figure 2.10[64]. Combined with a high precision platform, dynamic positioning of sample relative to the trapping potential could be provided, which greatly facilitates the calibration. The platform can realize the motion of sample and the relative motion of captured objects.
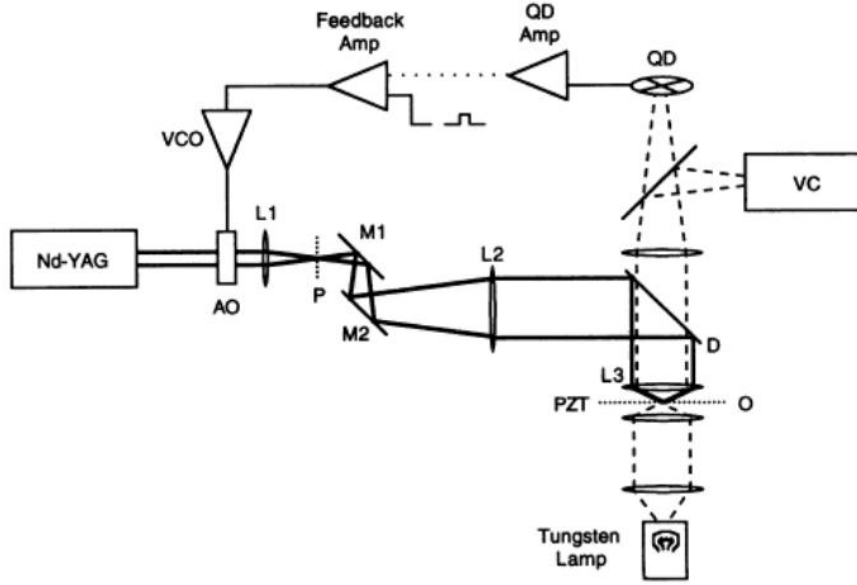
Figure 2.10 Schematic diagram of the single-beam optical tweezers[64].

There are two typical methods, namely numerical calculation method and experimental measurement method, to describe the capturing force of operating objects with optical tweezers.

In the numerical calculation method, two kinds of models are applied to deduce the optical trapping force on particles. The first one is the RO (Ray-Optics) model, which is suitable for that the dimension of object is much larger than the wavelength of laser beam[65]. The second one is the ESM (Electromagnetic Scattering) model, which is suitable for that the dimension of object is smaller than the wavelength of laser beam[66]. The RO model has developed quite perfect, while the electromagnetic scattering model introduced to electromagnetic calculation remains to be further demonstrated.

2.2.2 Ray-Optics Model

In order to reduce the complexity of calculating the optical trapping force, the handled objects are usually considered as the homogeneous and transparent particles. The reason for this is that other shapes are difficult to be calculated, the cell walls of the most animal cells and plant cells are

spherical, and the polystyrene balls and silicon balls which are usually used as operation handles are also the spherical. Hence, analysis of optical trapping force on Minovsky Particle imposed by laser can apply the principles of RO model to analyse the force condition of particles and apply the approximation algorithm of geometrical optics, as shown in Figure 2.11[67]. Because of the common occurrence of spherical center scattering, many efforts have been made to research the interaction of linearly-polarized beams and spherical objects. In order to obtain the numerical calculation of optical force under the RO model, researchers have developed many models. The most common model of capture mechanics was proposed by Svoboda et al. in 1994.
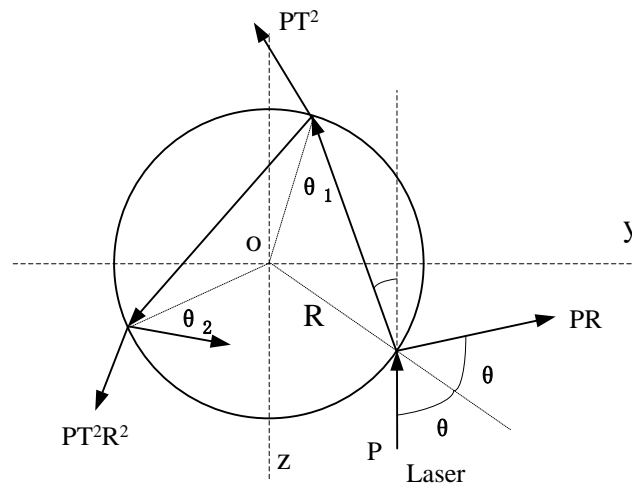
Figure 2.11 Schematic diagram of Ray-Optics model[67].

Figure 2.11 illustrates the RO model for the force acted on the medium sphere by single-beam incident light with the power of p. The incident power in unit time is $n_1 p / c$, and the angle between the incident light and the medium sphere is θ. The reflection light PR and the refracted lights PT^2 and PT^2R^2 are visible in Figure 2.11. In the scope of geometrical optics, light can be divided into many single beams with the same strength, the consistent direction of transmission and the same polarization. Each beam travels along a straight line in the same medium. The laws of refraction, reflection and polarization of light at different medium interfaces comply with

Fresnel Principle and the diffraction of light in the field is neglected. The force imposed on the medium sphere is the sum of the light PR carried by the reflection light on the surface of sphere and the lights PT^2 and PT^2R^2 refracted from the inside of sphere[65].

$$F = Qn_1p/c$$

(2.13)

where Q is the non-dimensional coefficient, n_1 is the refractive index of environment around the sphere, p is the laser power, and c is the light speed in the vacuum.

The force imposed on the sphere by light can be divided into the scattering force f_{sca} that travels along the light and the gradient force f_{grad} that is perpendicular to the propagation direction of light. According to Eq. (2.13), it is concluded that if the power of laser remains unchanged, for the same particle, the acting force of light acted on the particle can be expressed as[65]

$$f_{sca} = 1 + R\cos2\theta - \frac{T^2[\cos(\theta - \theta')] + R\cos2\theta}{1 + R^2 + 2R\cos2\theta'}$$

(2.14)

$$f_{grad} = R\cos2\theta - \frac{T^2[\sin2(\theta - \theta')] + R\sin2\theta}{1 + R^2 + 2R\cos2\theta'}$$

(2.15)

where R and T are the reflectivity and the refractive index of light on the surface of sphere, respectively; θ and θ' are the angle of reflection and refraction, respectively.

In the RO model, the gradient force and the scattering force of light imposed on the sphere are the vector sum of the gradient force and scattering force of all divided laser beams. This method is simple in calculation and easy to discuss the factors of effects on the optical trapping force. However, this method cannot present the relationship between the acting force of light acted on the particle and the size of particle, it neglects the diffraction spots after the focus of laser. Therefore, based on this method, the neglected optical polarization and scattering of light beam

39

are taken into consideration to improve the calculation of optical trapping force of Minovsky Particle.

2.2.3 Electromagnetic Scattering Model

If the particle diameter is much smaller than the light wavelength and in the scattering field of Rayleigh, the acting force on the particle can be calculated through the electromagnetic scattering model. For the electromagnetic scattering model, if the diameter of light spot generated by the highly focused laser is larger than the particle diameter, it can be considered that the particle is in a non-uniform electric field, which generally comes from the light distribution of laser. In general, the laser intensity has a fundamental-mode Gaussian distribution, namely, the laser beam is the strongest in the center and decreases gradually to both sides. If the particle is in a uniform electromagnetic field, it is easily affected by the distribution of electromagnetic field to show polarization itself. If the particle is in a non-uniform electromagnetic field, instead of polarization, it receives the function of electric field in electromagnetic field and the particle moves to the place where the electric field is the strongest. To sum up, if the particle is in a laser beam, it always moves to the center of light beam which originates from the interaction of the light-induced dipole moment between the electric component of light and the particle, as shown in Figure 2.12[68].
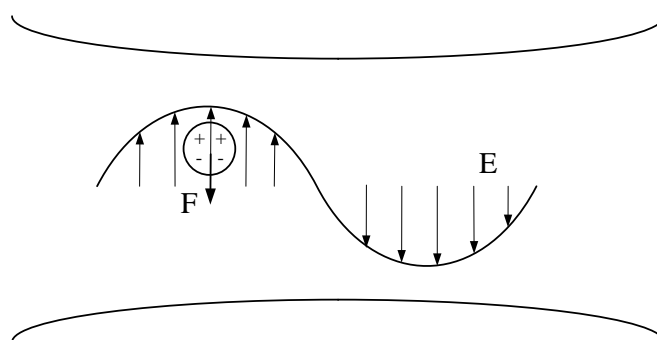
Figure 2.12 Schematic diagram of the force of Rayleigh on electromagnetic fields[66].

Therefore, after the laser beam is focused, the light intensity at its focus is the strongest and the particle finally moves to the focus being caught. Then, the gradient force caused by the Rayleigh

particle can be expressed as[69]

$$F_g = -\frac{n_m}{2} a\nabla E^2$$

(2.16)

where ∇E^2 is the gradient of light intensity, a is the polarizability of dipole moment of the Rayleigh particle and it can be expressed as[70]

$$\alpha = 3n_m^2 \frac{m^2 - 1}{m^2 + 2}$$

(2.17)

where $m = \frac{n_p}{n_m}$ is the relative refractive index of the particle, R is the radius of particle. This is the influence of the field induced by adjacent dipoles in the low-frequency case described by Clausius-Mossotti relation. The force is directed along the opposite direction of field gradient when $\alpha < 0$, and directed along the positive direction when $\alpha > 0$. That means the particle will be pulled into the centre of the light field maximum when its density is larger than that in the surrounding medium.

Combining the above techniques, the model RO and EM show that the particle will automatically move towards to the maximum of light intensity by the gradient dipole force. When the gradient force equals to the scattering force, the particle will be tapped. Then combined with a high magnification microscope, the particle can be manipulated in real-time.

2.2.4 Experimental Measurement

Theoretical calculation cannot substitute direct measuring results, because the optical force is sensitive in the tiny movement on the geometric deflection. There are many methods that can be used to calibrate the stiffness when the optical tweezers are in operation, such as the drag force

method, power spectrum method and equipartition theory. The drag force method is normally divided into the static method and the dynamic method. In the static method, after the particle is captured, the sample driven by the location platform moves at a constant velocity (usually trapezoidal movement). Subsequently, the particle deviates from the initial balance position due to the drag force of medium and reaches a new balance between the drag force and viscous force of light. The drag force can be calculated through Stokes' law[71]

$$F = 6\pi\eta Rv \tag{2.18}$$

where v is the velocity of the platform, R is the radius of the particle, and η is the viscosity of the solution. Then we can calculate the drag force under a certain offset until the particle cannot be captured. In the dynamic method, the particle is fixed at the position with a certain distance from the laser focus and the capturing laser is off at the beginning. When the laser is on, the particle will move to the focus of light beam. In the process, the motion curve of particle can be monitored and recorded in real time. The following equation is suitable for this process[72]

$$ms'' = F_{trap}(s) - F_{drag}(s') \tag{2.19}$$

where s is the location of the object and m is the mass of the object. The drag force can be calculated through the position of particle (function of time) and the Stokes' law. In addition to the above two methods, limited escaping force method is also developed by researchers. Because the tapping stiffness at the escaping point is different from the stiffness of the non-escaping point, the drag force method could not determine the accurate tapping stiffness. When the tapping particle vibrates at the balance point, the amplitude and frequency are related to the trapping stiffness. The power spectrum of deviation of a sphere 'x' is given by the following formula[73].

$$S_x(f) = \frac{k_b T}{\eta\pi^2(f_c^2 + f^2)} \tag{2.20}$$

where $f_c = \dfrac{k}{2\pi\lambda}$ is the characteristic frequency, T is the temperature, k_b is the Boltzmann constant. In the method of power spectrum, the tapping stiffness can be induced by the Levenberg-Marquardt (LM) algorithm. Here, the Lorentzian power spectrum of silica bead moving within one optical trap is shown in Figure 2.13.
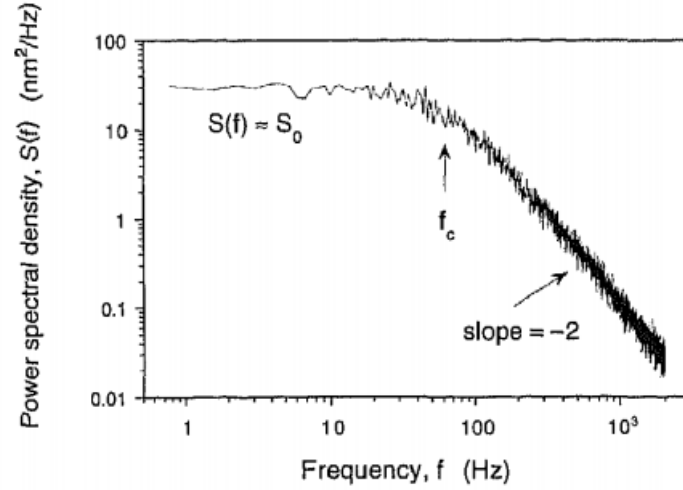
Figure 2.13 The Lorentzian power spectrum of the Brownian motion of a silica bead moving within one optical trap produced by a laser with 6mW[73].

The calibration of the thermal noise only relies on temperature and can obtain accurate results. It demands high precision measuring instruments, and the result can easily be affected by the band width and noise of system. In general, such calibration result usually contains an error of 5%. Accurate measurement of the cell force is significant to understand the physiological and pathological states of cells and tissues. Many numerical computation methods and experimental calibration methods have been used to obtain the optical force when optical tweezers are in operation. The force imposed on an object by optical potential trap depends on the properties of object (including size and composition) and the properties of optical potential trap (including the shape and stiffness of light beam), which can be described through the methods of numerical calculation and experimental calibration.

2.3 Applications in Cytology Based on AFM and Optical Tweezers in Liquid

2.3.1 Characterization of Biological Cells Based on Liquid-AFMs

AFM has great potential in a broad range of research fields, including biomechanics, biophysics and biochemistry, in particular, for the study of cells. AFM is used both as a tool for the 3D topographical information observation of cells on the nano scale and as a micro robot for the manipulation of cells. AFM can be directly used in the desired physiological conditions such as surface measurement, manipulation and characterization of living cells, bacteria, viruses, DNAs, protein molecules, and a variety of organic molecules. In addition, AFM still has been widely concerned as a sensitive sensor for the measurement of the force curves over the sample surface, such as elasticity, hardness, adhesion and friction.

2.3.1.1 AFM detection of topographical information

AFM was the most rapidly developed scanning imaging technique in the last two decades. It uses a physical probe as a sensor to image the surface of samples with an impressive atomic resolution by the interaction force between the tip of probe and the sample. Its resolution can be reached up to 0.1nm transverse resolution and 0.01nm longitudinal resolution, more than several thousand times of the resolution of optical microscopes. Moreover, compared to any other imaging microscope techniques, AFM is particularly useful for the research of biological systems due to the minimum preparation of the sample. The culture medium can be changed while scanning cells.

In cytology, AFM is capable of detecting the changes between transformed cells and normal cells in terms of morphology, cell growth, cell to cell interaction, especially organization of cytoskeleton[74][75][76][77]. AFM was used as a highly sensitive microscope for cell research. Barrera et al. used AFM to obtain different magnification images of Ab-decorated receptors, and provide the morphology information about the architecture of three types of ligand-gated ion channels, as

shown in Figure 2.14[78]. In other studies, Braet et al. used AFM to investigate surface and submembranous structures of living hepatic natural killer (NK) cells under the physiological conditions.
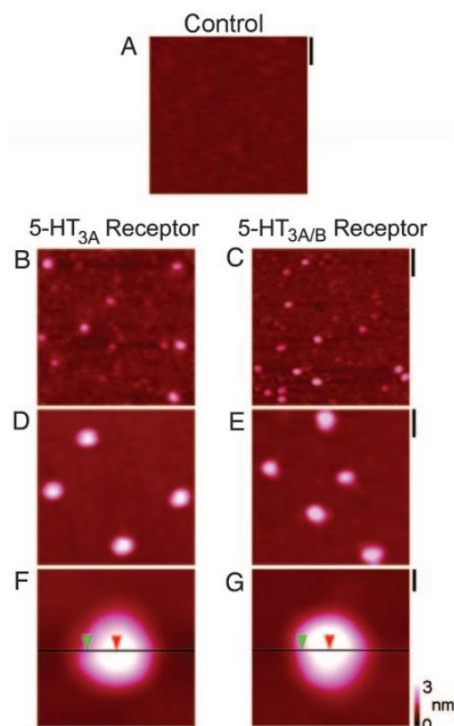
Figure 2.14 Different magnification images of 5-HT3A/B and 5-HT3A receptors scanned by AFM[78].

However, AFM has not been the straight microscopy in the majority of these applications. Confocal microscopy, in particular fluorescent optical microscopy, is still superior to AFM for cell imaging due to its quick imaging and provides robust statistics. The major advantage of AFM comes from several features, including ability to detect surface interaction, capability to obtain the force curve of cell stiffness and mechanics and extremely high sensitivity in the vertical deformation of cantilever.

2.3.1.2 Atomic force spectroscopy of surface interactions

It has been shown that AFM is capable of measuring the force curve between single molecules

attached to AFM tip and surfaces of interest. It has vast potential applications beyond biomedical field. This mode of operation is usually called atomic force spectroscopy[79][80]. Any material of the samples is generally available for the morphology imaging with AFM. Meanwhile, ligand-receptor interactions on the cell surface are different interactions between the probe and sample are usually identified as the supplement to the information of the sample[81].

Unlike the imaging function of the AFMs, atomic force spectroscopy usually needs to close the feedback loop. Cantilever-probe is used as a force sensor to characterize the samples. The characteristic information in each scanning point is more accurate than the surface information obtained in scanning process. In general, the AFM tip approaches the cells sample at a certain speed and indentation force by the movement of PZT. During the process, the deflection of cantilever will be detected by PSD, and the characteristic information of cell mechanics and surface interactions can be analysed. Moreover, it can also attain a considerable higher resolution, especially along the vertical direction. The research of surface interactions is beneficial to understand and explore the complicated development processes of physiological and biochemical changes at the single-molecule level[82].

The atomic force spectroscopy represents the deflection signal for each complete up-down movement of the PZT. Typically, the cantilever stays in its balanced state and zero deflection of the force curve if tip away from the sample surface with no long-range interactions, as shown in Process A in Figure 2.15. The pull-down process continues, when the sample is brought close to the tip, and due to the attractive forces between the tip and the sample, the tip adheres to the sample, as shown in Point C in Figure 2.15. Then, the sample scanning is carried up as the PZT continues to extend. Eventually, the spring force equals to the attractive forces with non-deflection, as shown in Point D in Figure 2.15. When the PZT continues to extend, a strong repulsion force between the sample and the tip will exist, and the cantilever bends against the sample, as shown in Process F in Figure 2.15. After each approach, a force versus extension profile can be obtained.

During the process, the AFM tip will form a slight upward bend by physical adsorption, covalent bonding, or ligand-receptor interaction. When the tip and sample separates, the cantilever adheres to the surface of sample due to an attractive force, and results in a cantilever bending towards the substrate, as shown in Process G in Figure 2.15. Then, the cantilever performs a sudden rebound as the bending stretched further, and finally is pulled free with non-deflection, as shown in Process H in Figure 2.15.
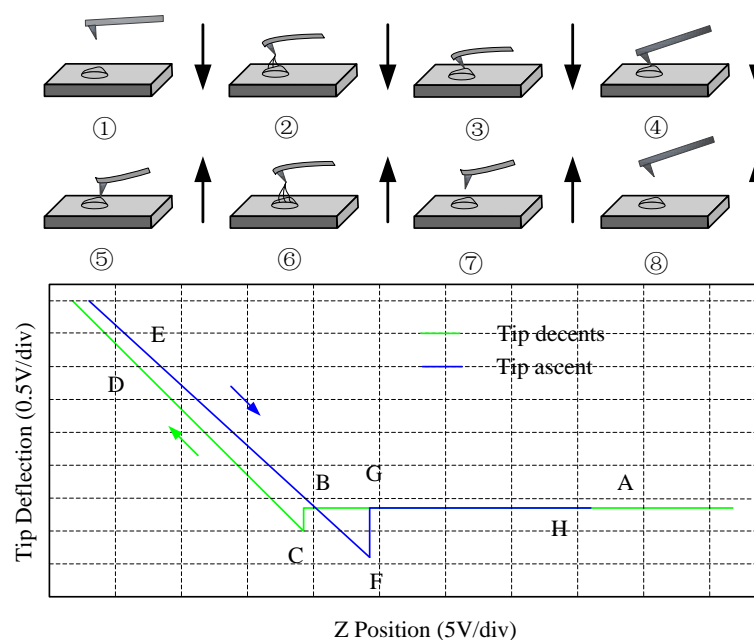
Figure 2.15 Schematic of the typical force-distance curve in atomic force spectroscopy. ① Probe is away from the sample with non-deflection. ② Probe is pulled down with the upward deflection due to the attractive force. ③ Probe sticks to the surface of sample. ④ Probe is pulled down when it reaches a balance with non-deflection. ⑤ Probe is pulled away from the sample as the indentation is completed. ⑥ Probe sticks to the sample with the downward deflection due to the attractive force. ⑦ Probe performs a sudden rebound when it leaves the surface completely. ⑧ Probe is pulled free with non-deflection.

2.3.1.3 Cell mechanics

In the studying of cell mechanics, the AFM records viscoelasticity characteristics on the cell

surface with sub-nanometer resolution. It has a unique advantage in the lateral manipulation and enough loading force on the surface with extremely high precision. Moreover, the pathogenesis of diseases can be attained with the AFM method by the correlation of elasticity of different diseases[83]. Berdyyeva et al discovered that the cell elasticity could be changed quite considerably in older versus younger cells, as shown in Figure 2.16[84]. The Young's modulus of older cells was decreased two to four times than the younger cells, and the volume of older cells was increased.
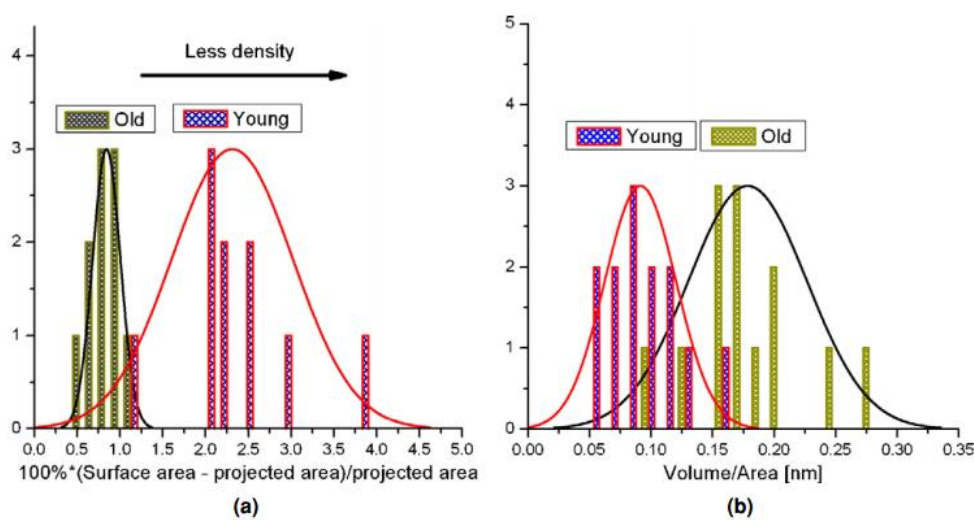
Figure 2.16 Statistics of the cytoskeleton[84].

By now, there are many scholars researched on the detection of elasticity of cancer cells, which shows differences from normal cells, including indentation measurement of living cells[85] and viscoelasticity characteristics detection during cell division or bio-efficacy[86]. In addition, cell adhesion refers to cell-cell and cell-matrix interactions, which is not only the main approach for the communication between cells but also an important biological phenomenon for the maintenance of morphology and functions in multi-cellular organisms[87][88]. For instance, on the research of artificial organs, the cell-cell adhesion and the cell-substrate adhesion are closely related to the biological compatibility of artificial implants[89]. Hence, AFM has been used in the research both as a terminal executor for the detection of the morphology character on the cell

surface and as a manipulator for the acquirement of various mechanical properties on the cell surface. Above all, great attention has been paid to the cell-cell adhesion, cell-matrix adhesion, stiffness change of cells and viscoelasticity distribution, related cell morphology structure, function, deformation ability and adhesion of cells.

2.3.2 Characterization of Biological Cells Based on Optical Tweezers

Compared with the cell test method in traditional medicine, the application of optical tweezers as the cell testing tool could solve the problems existed in the test of biomedical cells. Optical tweezers could control the living cells without any damage and rapidly isolate them from the various clusters. Moreover, optical tweezers has a little impact on the surrounding environment during the process of cell manipulation. Implementation of capture and separation experiments for cells using optical tweezers could conveniently study the properties of cells, such as the adhesion between two cells, the elasticity of the cell membrane and the strain capacity of the cell, thus to effectively understand the real physiological process of cells[90]. However, applying optical tweezers to the test of cells also has many disadvantages and its theory is still immature, which needs further analysis and development.

2.3.2.1 Elasticity of cell membrane tested by optical tweezers

The red blood cell of human body has a small volume, with a diameter of only 7μm, and has a shape like a disc, down in the middle and thick at the edge, with good elasticity and plasticity. Moreover, the diameter of blood capillary is smaller than micron. When it passes through the blood capillary which the diameter is smaller than it, it can change its shape and restore the original shape after it passes. Thus, it can be seen that the blood capillary must have good orientation property to go through the blood capillary without any damage. The results show that such deformation characteristic of blood capillary plays a critical role in the process of blood circulation. Therefore, the elasticity of blood capillary is an important indicator to reflect the

functional activity of blood capillary. Fontes et al used optical tweezers to measure the membrane viscosity, cells adhesion, and the zeta potential of two RBCs (Red Blood Cells) in an electrolytic solution, as shown in Figure 2.17[91]. The cell adhesion was quantified by displacing two RBCs apart until they were not agglutinated. The experimental results showed that the force-displacement relationships for the red bloods could be obtained reproducibly in vitro and further demonstrated the existence of elastic properties of the red blood cell.
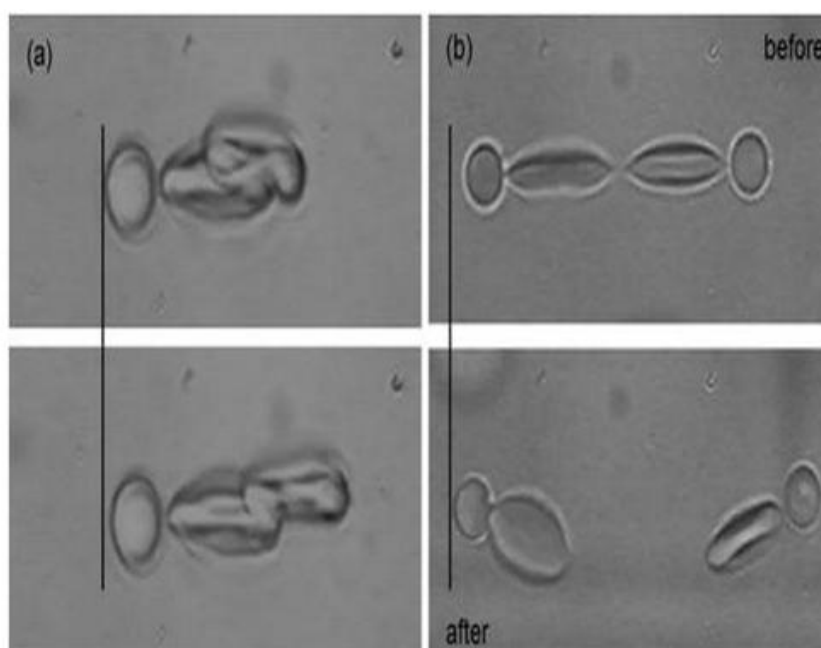
Figure 2.17 Optical tweezers were used to measure the cell adhesion quantified by displacing two RBCs apart until they are not agglutinate[91].

2.3.2.2 Quantity of electric charge on the surface of cell tested by optical tweezers

The electric charge on the surface of cell is closely related to the growth cycle of cells and directly affects the changes of physical functions of cells. It plays an important role in the cell differentiation, cell recognition, cell adhesion, swallowing and spitting of cells and transformation from normal cells to cancer cells[92]. At present, the common method of biological medicine could

not measure its quantity of electric charges, and could only know that the quantity of electric charges on the surface of cell has changed, but could not demonstrate the variable quantity. The variable quantity of electric charges on the surface of cell has an important meaning for further research on physiological properties of cells. Therefore, the method for detecting the quantity of electric charges on the surface of cell by optical tweezers has been proposed. Pesce et al used optical tweezers to measure the surface electric charge of single *Bacillus subtilis* spores, as shown in Figure 2.18[93]. This technique was able to discriminate the three spore types of *Bacillus subtilis* according to their hydrodynamic coefficient induced by the surface charge.
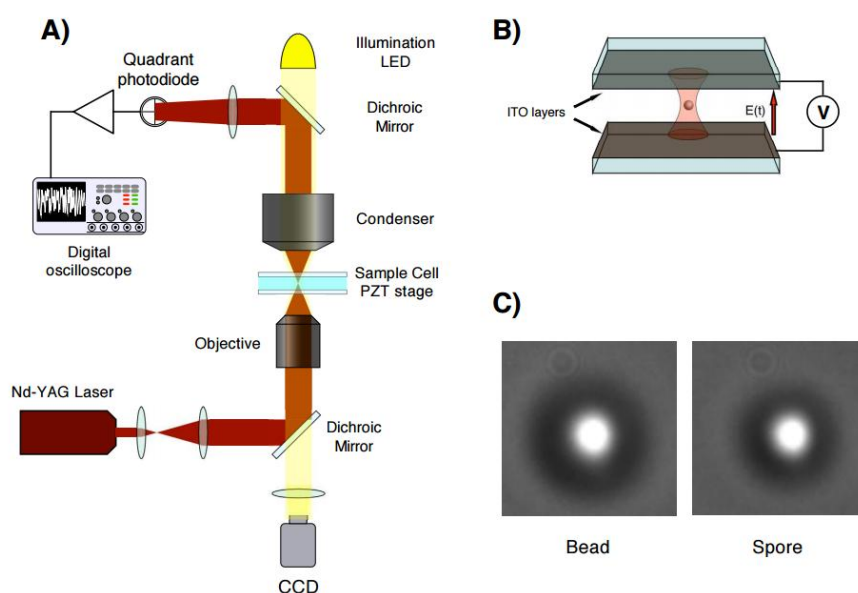
Figure 2.18 Optical tweezers were used to measure the surface charge of *Bacillus subtilis*[93].

Since the surface of cells has positive and negative changes, cells scatter in the solution in suspended states. In an electric field, cells generate electrophoresis due to the influence of electric field and the cell suspension will occur with electro-osmosis, thus to generate an electro-kinetic phenomenon. At this time, cells and the reference sample start the relative motion with the movement speed depending on the magnitude of external electric field, so controlling the

magnitude of external electric field can control the movement velocity of cells. The combination of optical tweezers and the electro-kinetic phenomenon reaches the purpose of detecting the quantity of electric charge on the surface of cell. Since the cells have different suspending heights in liquid, it causes inaccurate measurement results. Therefore, a method that could accurately describe the mechanical characteristics of cell manipulation is needed to accurately express optical force.

The above mentioned are the main applications of optical tweezers in implementing cell tests. The biggest difference between them and existing biomedical cells is that optical tweezers could test living cells without any contact, ensure cell activity, and make test results more accurate. Medical test method, for instance, the LFCM (Laser Flow Cyto Meters), needs to implement fluorescence calibration for cells, and can only test the calibrated cells, thus to affect the cell activity and lead to the error between the test results and living cells. However, optical tweezers technology is still immature with many problems. For instance, optical tweezers implement tests by applying the different refractive indexes of the media, while there are cells mixed in different sizes in cell research. Therefore, it is meaningful for the combination of the optical tweezers technology and medical test method.

2.4 Methodology in the Thesis

In this thesis, a hybrid nano handling and measurement technique based on AFM and optical tweezers is presented and the techniques to realize innovative and multi-functional applications in biomedicine are studied. Among them, the technique based on AFM is able to visualize and quantify the dynamics of living cells in culture on the nano scale, especially the cellular shear adhesion force was accurately measured in the research of the cell-substrate interaction in terms of biophysical perspective. The innovative findings are conductive to study the cell-cell adhesion, the cell-matrix adhesion, related to the cell morphology structure, function, deformation ability and adhesion of cells and better understanding of the cellular dynamic behaviors. The technique based

on multiple optical tweezers are able to characterize the optical trap stiffness and the escape velocity, especially to realize the capture and sorting of multiple cells by a polarization-controlled periodic laser interference output. It can trap and move hundreds of cells without any physical contact, and has broad application prospects in general biology, cell biology, Immunology, cell engineering and genetic engineering. The framework of methodology of my work is shown in Figure 2.19.
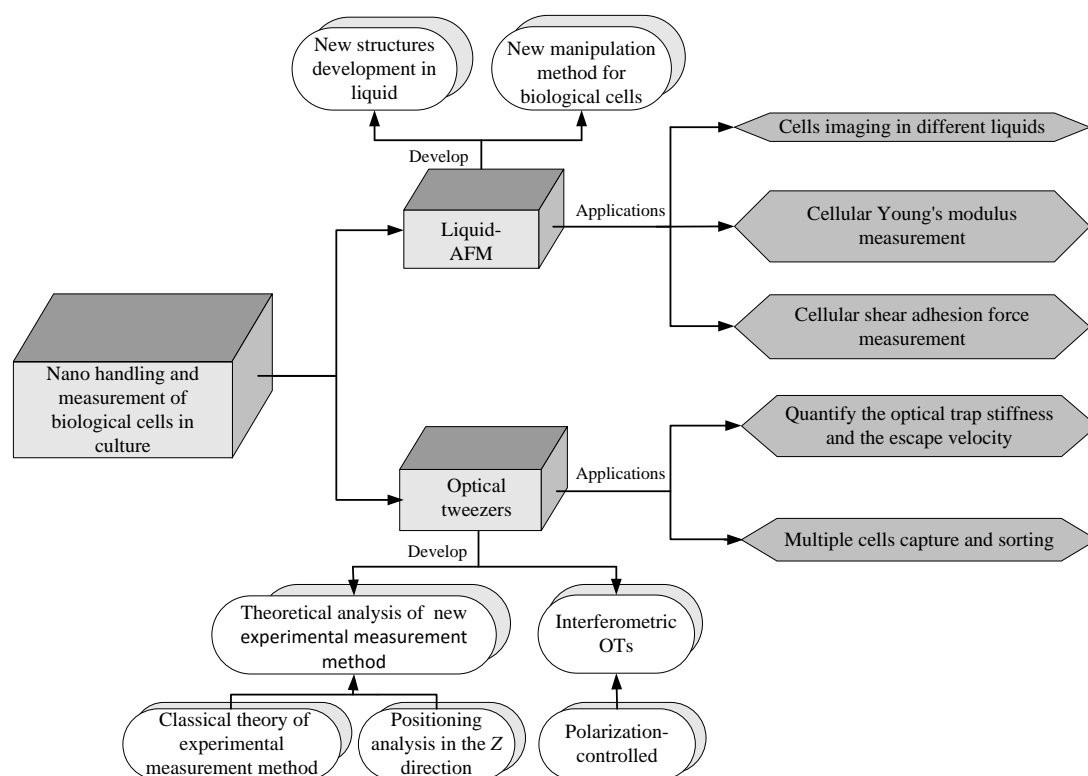
Figure 2.19 Framework of the research methodology.

Compared with the predominance and the deficiency of nano handling and measurement techniques and combined with the background and motivation in this thesis, an integrated system including liquid-AFM and OT based on laser beam interference is developed. Moreover, several potential applications, including cell imaging, cellular viscoelasticity measurement, cellular shear adhesion force measurement, cell escape velocity measurement and the capture and sorting of

multiple cells, are experimentally explored. Among them, the cellular shear adhesion force measurement and the capture and sorting of multiple cells by polarization-controlled three-beam interference are the unique applications which can effectively improve the detection mechanisms in medicine tests.

Benefiting from the methodology of the hybrid nano handling and measurement technique, several chapters, which revealed in views of system development, theoretical derivation and applications respectively, are well established. Chapter 3 describes a novel development of liquid-AFM system, which is capable of imaging both in liquid environments and air conditions with high resolution. A unique scanner head and liquid cell are developed which can overcome the limitations of current AFM systems developed above. The innovations bring about a high level of system integration in the structural design and provide a suitable environment for biological samples which can live for a long time. In Chapter 4, the biomechanical analysis of quantities of individual single cell applications is explored with high efficiency and straightforwardness. It shows the relationship of biomechanical and cellular viability, which is not clearly provided in the state-of-art. The method provides a way for the measurement of the cellular shear adhesion force between the cell and the substrate, and for the simultaneous exploration of cells using the AFM imaging and manipulation. Subsequently, Chapters 5 and 6 are to implement the development of nano handling technique based on OT. The main objective of Chapter 5 is to develop single optical tweezers, and a novel static viscous-drag-force method has been presented to characterize the optical trap stiffness and the escape velocity. Inspired by the shortcoming of experimental results in Chapter 5, a sensitive and highly efficient polarization-controlled three-beam interference set-up is proposed for the capture and sorting of multiple cells in Chapter 6. With the theory of superposition of three beams, simulations on the influence of polarization angle upon the intensity distribution and the laser gradient force change with different polarization angles are carried out. Hence, the methodology focuses into the innovation of nano handling and measurement of biological cells in culture and the improvement of the detection mechanisms in medicine tests.

2.5 Summary

In this chapter, two basic concepts in the traditional AFM and OT are introduced. These two techniques have become the most basic tools for biomedical research with their unique working method. This chapter mainly shows the generality and efficiency of biological characterization based on the AFM and OT, and describes their working principle, working mode and working process in the application of biomedical research. With the investigation of traditional products, it is found that there are a number of limitations associated with the nano handling and measurement problems in the physiological cases such as the structural design of AFM for the air condition may not be suitable to work in liquid, few reports on OT has considered the dynamic analysis during the automated transportation and most of studies for the creation of multiple optical traps are limited to create a pattern of linear interference fringes or a few of dot traps without adjustable formations. Hence, the methodology is addressed to overcome the deficiencies in Section 2.4. In the subsequent chapters, the integrated system and its application in biomedicine research will be described in detail.

Chapter 3

Development and Optimization of Liquid-AFM

In the previous chapter, we discussed the working principle, the operation modes and the scanning techniques of atomic force microscope for applications in the field of biomedicine and addressed the shortcomings in current research. On that basis, this chapter designs and establishes the completed liquid-AFM. The main tasks are to design and manufacture a new liquid-AFM probe unit, establish new photoelectric detection system, develop and optimize the scanning control and feedback circuit, and compile the scanning control software which is suitable for the cell imaging used in air conditions and liquid environments to improve the working efficiency and accuracy for the micro/nano manipulation. Each part of the liquid-AFM is described as follows, including the structure of probe unit, the photoelectric detection system, the micro/nano feed mechanisms, the external devices and the scanning software.

3.1 Design of Liquid-AFM

Figure 3.1 shows the schematic of a liquid-AFM currently under the investigation. It basically comprises five main parts, including the liquid-AFM probe unit which consists of a quick-release chuck for the attachment of probe holder and an unique liquid cell, the photoelectric detection system which consists of an AFM scanner, the position control platform, the laser and the PSD (Position Sensitive Detector) for measuring the deformation of the cantilever and an optical microscope with CMOS (Complementary Metal Oxide Semiconductor) camera for monitoring the position of the probe and the samples, the micro/nano feed mechanisms which consist of a coarse adjustment displacement platform and a fine adjustment displacement platform, the external

devices which consist of A/D (Analog to Digital) and D/A (Digital to Analog) converters, and the human-machine interface system with the control software and the sample imaging in real time.
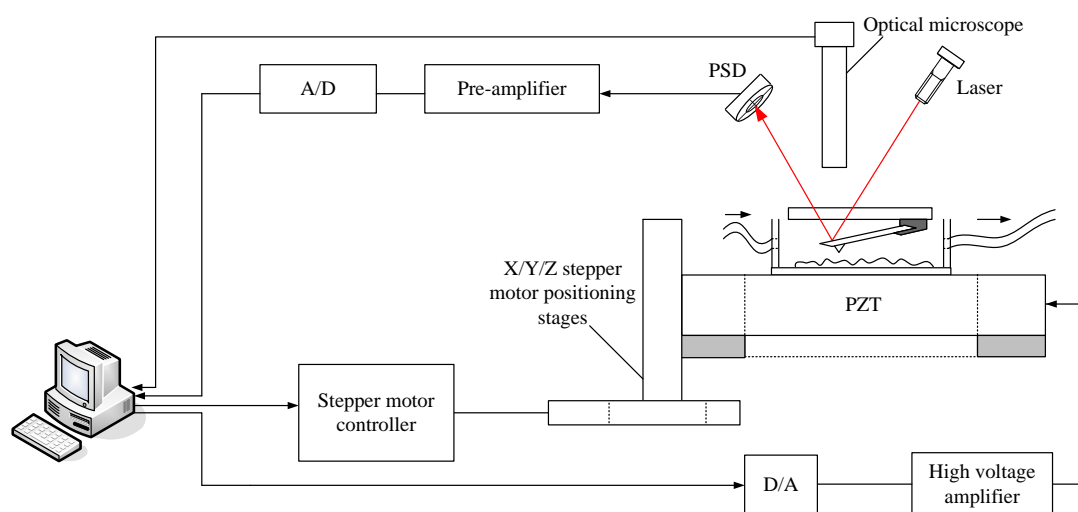
Figure 3.1 Schematic set-up for nano handling and measurement of biological cells in culture.

In the liquid-AFM, the stepper motor positioning stage is the micrometer-ranged coarse approaching mechanism placed on the table and it supports the PZT scanner. The 3D PZT scanner is the precise approaching mechanism with the motion range of 150μm×150μm×150μm. The sample to be measured is placed on the scanner. Hence, a typical optical detection method for sample-scanning AFM is developed. The collimated laser beam is focused on the reverse side of cantilever coating with the metallic reflector, and reflects the movement of cantilever through the interface of air-solid and solid-liquid. Then, the atomic forces are transformed into a magnified deflection displacement and detected by the PSD without the influence between the surface tension and the probe. This method has enabled the elimination of the limitations of current AFM systems which are hard to work in both air conditions and liquid environments. When the probe approaches to the sample, the scanner drives the sample to implement the scanning in the direction of *X-Y* and the cantilever deflects with the surface undulation of the sample. As shown in Figure 3.1, the red laser is reflected from the cantilever and probe, and detected by the PSD. It can detect

the deformation of the cantilever, due to the external atomic force between the sample surface and the probe. While the probe is brought to contact with the surface of the sample, the system starts to scan over the sample. The square PZT, selected as the scanner in the AFM system can also remove the scanning errors produced by PZT Tubes. After the conversion of A/D card, the human-machine interface and the feedback control system can receive the detection signals. When the sample is scanned along the direction of X-Y, the recording of the PZT displacement in the Z direction can obtain the three-dimensional information of the sample surface. Meanwhile, the feedback circuit is used to control and adjust the extending and contracting of PZT in the Z direction to implement the feedback compensation, so as to adjust the distance between the probe and the sample, and protect the sample free from the damage. The AFM system needs to keep the deflection of the cantilever always in the *Setpoint*.

Figure 3.2 Photograph of the liquid-AFM system.
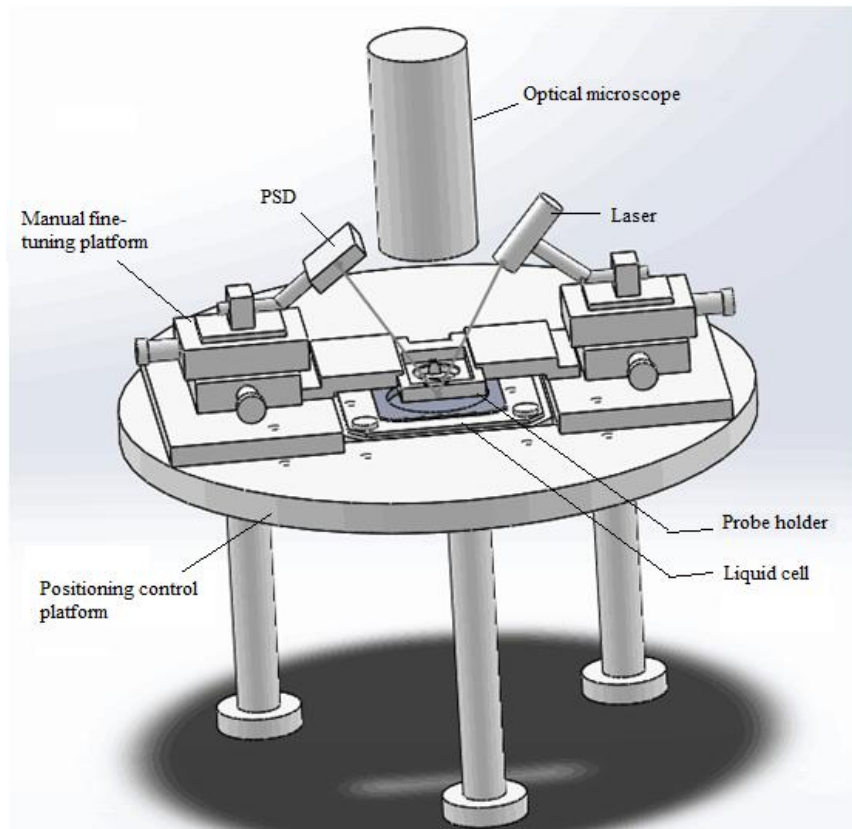
(A)
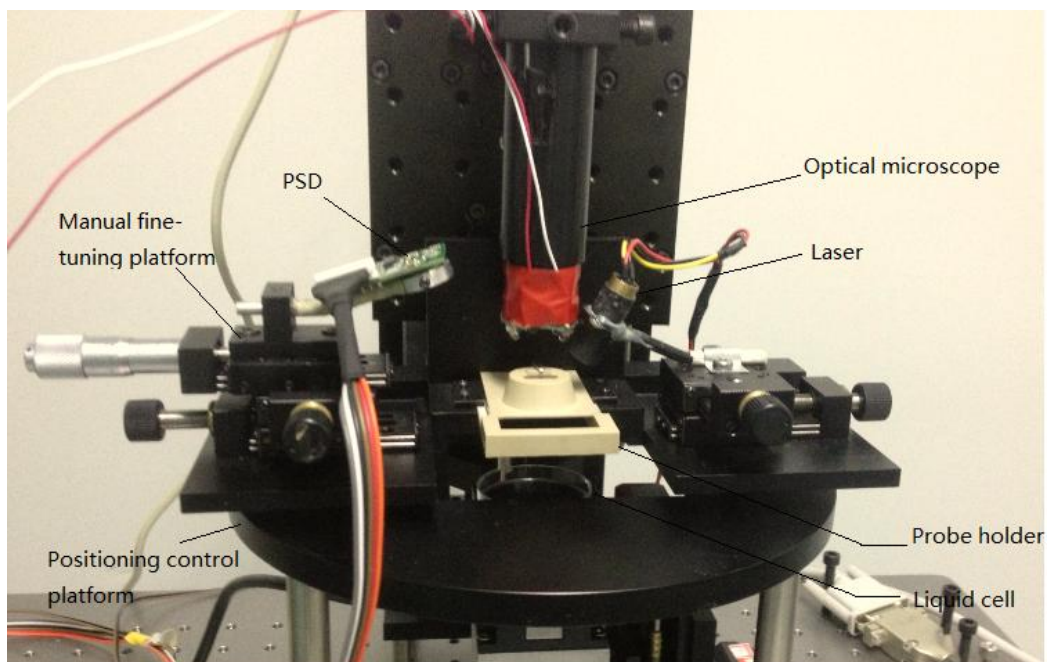
(B)

Figure 3.3 Configuration of the liquid-AFM platform designed by Solidworks (A) and its photo (B).

Figure 3.3 shows the schematic of the liquid-AFM platform which can be used in both air conditions and liquid environments. The sample to be measured is up to a maximum size of 150μm×150μm in each scanning. Combining with the stepper motor positioning stage, the scanning range can be improved from 100μm to 25mm in 3D. The liquid-AFM has a number of advantages, as described in the following.

1. The lateral resolution of the AFM measurement in culture is better than 2nm, and the vertical resolution is better than 0.1nm, covering a scan range up to 150μm×150μm×150μm.

2. A transparent window is designed to make the beam path across the interface of the air-solid and the solid-liquid, rather than the air-liquid path. The probe tip is not influenced by the interfacial force.

3. A special liquid cell is designed to make the cells survival for a long time while they are manipulated. Cells can be observed by AFM during the whole growth and development.

3.2 Development of Liquid-AFM Probe Unit

The liquid-AFM probe unit mainly includes the quick-release chuck for the attachment of the probe holder, the position control platform and the unique liquid cell.

3.2.1 Probe Holder

The probe holder is designed for the probe hold and quick-release chuck for the attachment of the probe, as shown in Figure 3.4. It is designed by the Solidworks platform. As shown in Figure 3.4(A), the insulated circuit board provides enough layers for the electric signal input with no distractions and the slots of probe holder support the quick-release chuck for the attachment of the probe. As shown in Figure 3.4(B), the probe can be fixed by the iron band when it scans the sample. From Figure 3.4(C), the ellipse section can totally put the probe into the culture during

scanning, and the angle of 11 °makes up the incline between the cantilever and the sample.

(A)

(B)

11 °

7mm

70mm

(C)
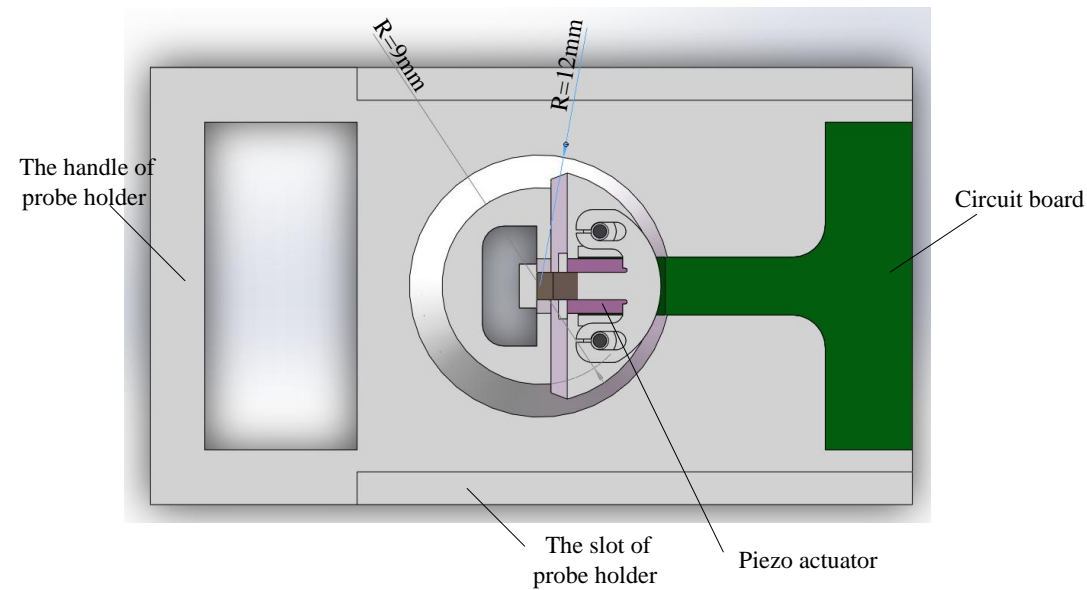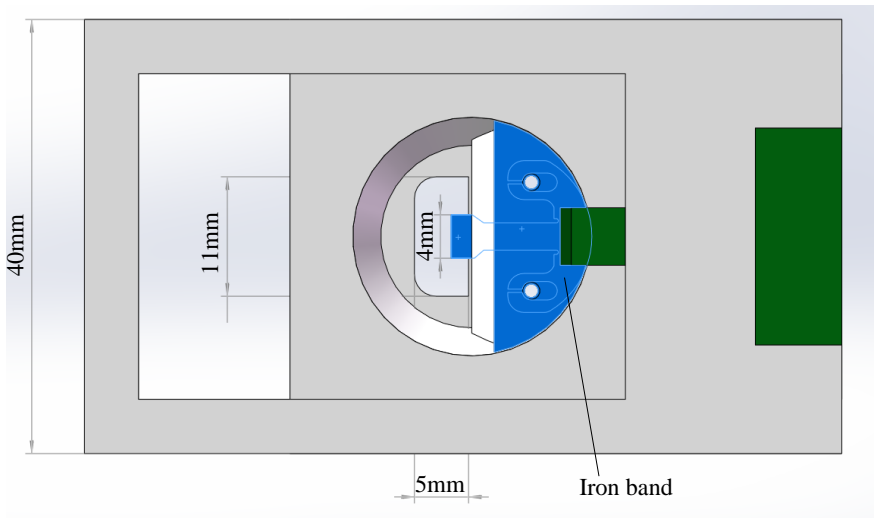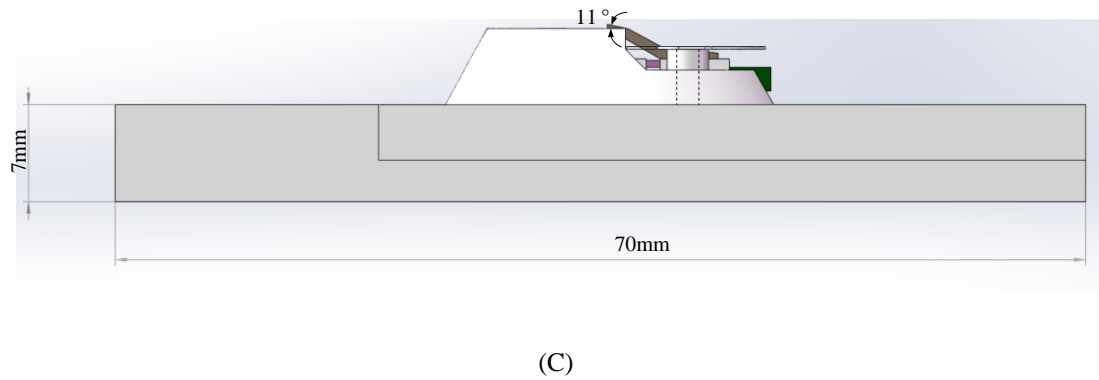
Figure 3.4 Design of the probe holder. (A) The bottom view of the probe holder. (B) The top view of the probe holder. (C) The side view of the probe holder.

3.2.2 Liquid Cell

This is a novel method of AFM measurement in both air conditions and liquid environments. In most of the previous versions of AFM measurement in culture, a liquid-drop was simply dropped on the sample surface, and the probe was used to scan the surface in the liquid-drop. Firstly, the sample was not totally submerged from above into the liquid cell. Secondly, the probe tip and the optical beam path were undoubtedly disturbed by the interfacial force. While in our new design, these problems can be successfully avoided. The transparent window fixed in the probe holder has been designed over the probe, and it makes the beam path across the interface of the air-solid and the solid-liquid, rather than the air-liquid path, as shown in Figure 3.5(A). The most significant advantages of this structure are that the surface tension of liquid just acts on the crescent shape part, the evaporation of liquid is decreased and the influence between the surface tension and the probe can be avoided. Thus, the beam path of the AFM measurement in liquid is not disturbed by the surface fluctuation of the liquid, and the cells can survive for a long time while they are measured and manipulated. Furthermore, a specific liquid cell with the input/output ports and a glass on the surface of the liquid, as shown in Figure 3.5(B), could remove the surface movement of liquid and eliminate the air bladder.
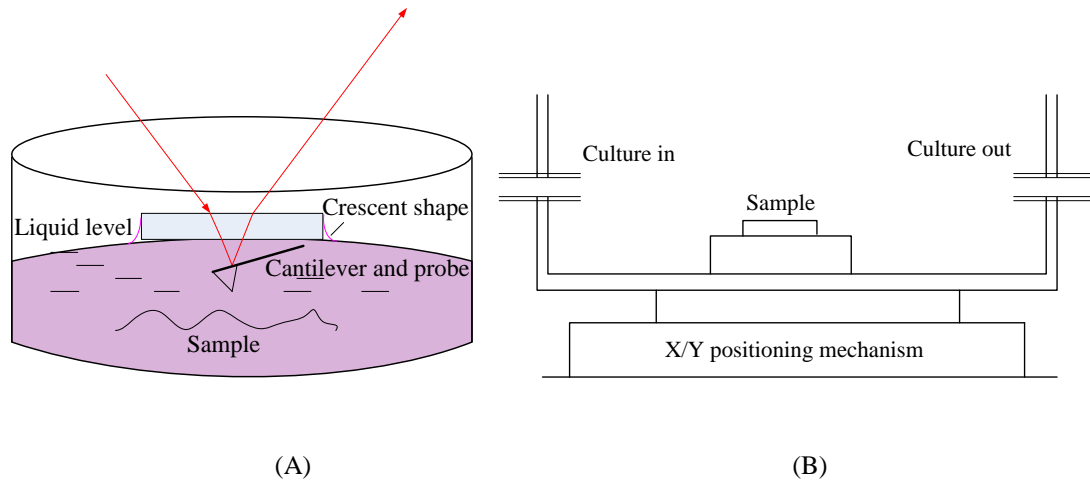
Figure 3.5 Schematic of light path of AFM in liquid (A) and the design of liquid cell (B).

3.3 Development Photo-electric Detection System in the Liquid Environment

3.3.1 AFM Scanner

The AFM scanner is mainly used for supporting the probe holder, as shown in Figure 3.7. There are two parts in the AFM scanner, including the regulatory region of PSD and the laser, respectively. Two of the same 2D displacement tables have been used for the movement of PSD and laser with a maximum displacement of 25mm, as shown in Figure 3.6(A). It can provide a large range of movement for the PSD to receive the optical signals when the scanning environment is changed from different liquids. The distance between two regulatory regions is 70mm. Hence, there is enough space to place big samples. Moreover, three counterbores are processed at the lower side of the scanner used to be fixed with the thread through the holes located in the position control platform, as shown in Figure 3.6(B). The center of AFM scanner is basically a point in the middle of three counterbores. Through the calculation of force acting on the scanner, the design can be displayed more stable.
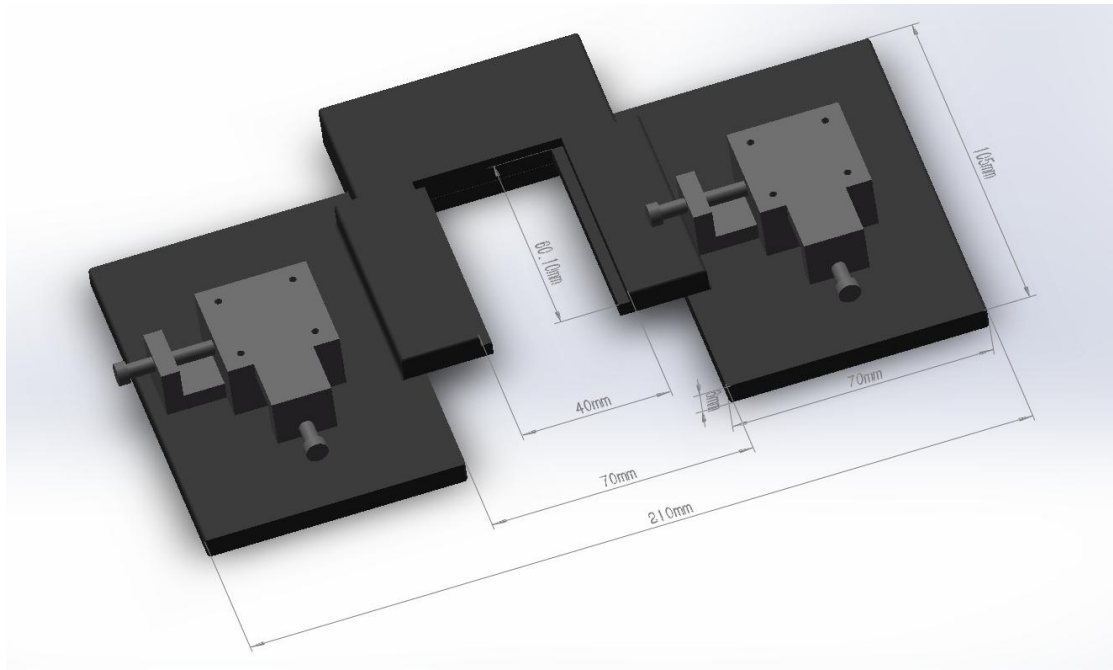
(A)
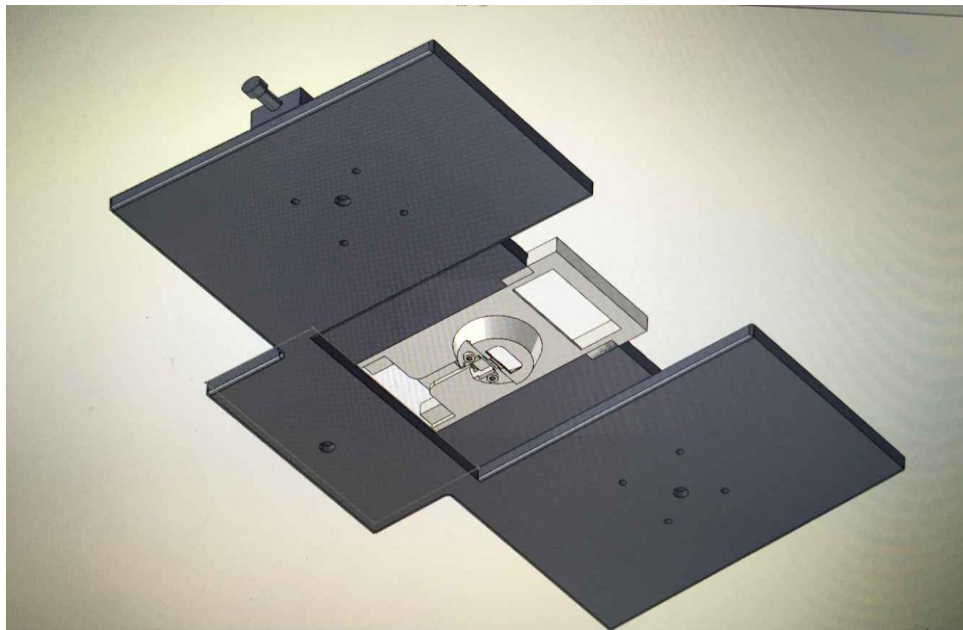
(B)

Figure 3.6 Design of AFM scanner by Solidworks. (A) The front view of the AFM scanner. (B) The

bottom view of the AFM scanner.

3.3.2 Position Control Platform

The position control platform is mainly used for supporting the scan head which will be described in the   following section, and adjusting the location between the scan head and sample. As shown is Figure 3.7(B), it is the drawing of the position control platform by Solidworks. There are three threads through the holes used for fixing and adjusting the scan head on the horizontal position, and the three threaded holes are on the lower side of the platform used for combining with the adjustable supporting bar. The distance from the base line can be adjusted by the supporting bar due to the height of sample. Hence, the height of sample to be measured can be reached up to a maximum of 5cm.
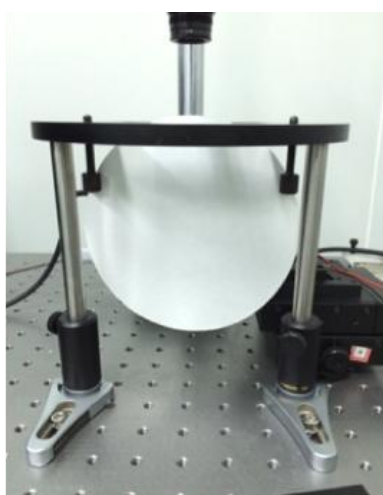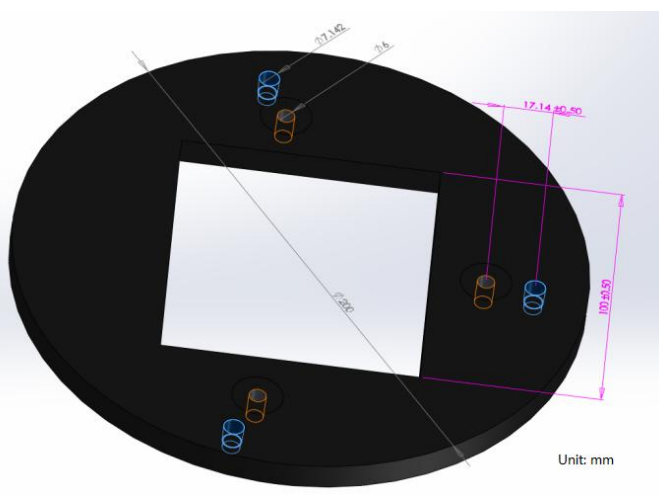
(A)   (B)

Figure 3.7 Design of the position control platform. (A) The photograph of position control platform.

(B) The design of position control platform by Solidworks.

3.3.3 Light Source

A semiconductor continuous laser made by CNI (Changchun New Industries Optoelectronics Technology) operated in the TEM_{00} mode at 650nm, with the output power of 0-10mW and the

beam divergency of 1.0mrad, is used as a light source. Its operating voltage is 10V and provided by a DC power supply.

3.3.4 Detection System

PSD is the position sensitive detector with the current to voltage amplifiers that provide the up-down and the left-right difference signals. Additionally, the PSD also provides a signal that is the sum of all the four quadrant field signals, as shown in Figure 3.8. The detector active area of PSD has the diameter of 7.8mm.

The sum signal: According to the light intensity, the probe can be adjudged whether it contacts the sample. Moreover, the situation of probe can also be estimated to know if it is polluted.

The up-down signal: The deflection of cantilever and the forces acted on the sample can be calculated by this signal, and then the topographical information can be obtained.

The left-right signal: This signal reflects the deflection of the cantilever in the twisted direction, and the deflected information and the force acted on the probe in the twisted direction including friction, shearing adhesion forces, and the step effect can be calculated by this signal.

The PSD used in the design made by PSS (Pacific Silicon Sensor, INC.) with the power supply ±15V and the output voltage ±3V.

Figure 3.8 Photograph of the PSD.

3.3.5 Real-time Visual Feedback System

In the current development of nano manipulation, AFM is often used to scan the whole area to show the topography of the sample without the real-time visual feedback. To overcome the shortcoming, there is an optical microscope above the liquid cell, as shown in Figure 3.9. The optical microscope could show an area of the picture in real-time, and combine with the force feedback. The visualization and quantification of the dynamics of living cells in culture can be implemented.
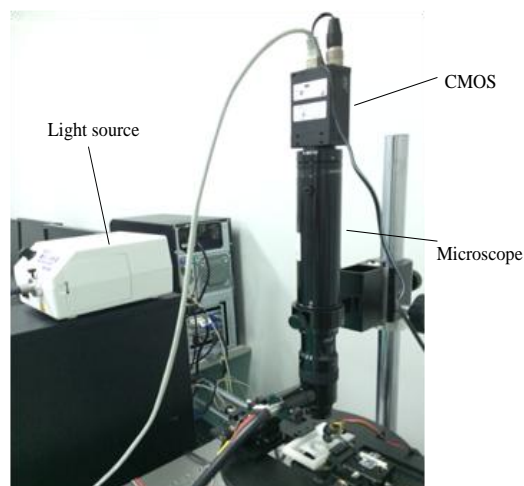
Figure 3.9 Photograph of the optical microscope.

The optical microscope consists of a CMOS color camera and a simple single lens microscope with the maximum magnification of 5×, as shown in Table 3.1. Table 3.2 shows the parameters of CMOS color camera. It has more than 9 million pixels and the size of each pixel is 1.75μm to meet the requirements of biological sample imaging and positioning. According to the principle of optical microscope, the working distance is inversely proportional to the resolution. Moreover, too small working distance between the objective and the sample may block the light path emitted from the laser onto the AFM cantilever. Hence, a suitable optical microscope with an enough working distance and magnification is very important in the structural design.

Table 3.1 Parameters of the optical microscope.

Magnification	Working distance	Field of view	NA	Depth of field	Resolution
5.0×	32mm	1.0×0.7mm	0.25	32μm	1.3μm

Table 3.2 Parameters of CMOS color camera.

Type	Pixel	Size of each Pixel	Transmission rate	Scanning mode	Sensitivity	Optical size
RZ-F900CF	3488×2616	1.75μm×1.75μm	4FPS	progressive scanning	550nm	1/2.3inch

3.3.6 Design of the Light Path in Liquid-AFM Probe Unit

According to the size and the operation parameters of the optical microscope, as shown in Figure 3.10(A), it is the design of the light path in the liquid-AFM probe unit. Because the optical microscope is located over the probe holder, the light beam emitted from the laser cannot perpendicularly incident on the cantilever. Hence, when the light beam intersects the edge of optical microscope, it is the limiting position in the design. Then, the incident angle can be

determined as the minimum design angle. Furthermore, as the active area of PSD is 7.8mm in diameter, the beam divergency of laser is 1.0mrad, and the width of probe usually used in the experiment is 50μm, the light path in the design is less than 8cm and the distance between the laser and probe is less than 3cm. Hence, a suitable angle of 48.1 °is designed for the light path. As shown in Figures 3.10(B) and (C), they are the schematics of the light path when the light passes through the silica glass and emits into the solutions with different refractive indexes. Among them, the laser passed through the silica glass will be expanded when $n_{air} < n_{glass} > n_{liquid}$. Then, the manual fine-tuning platform used to adjust the position of PSD is designed with a large motion range, so that the whole light spot emitted into the PSD can be detected.

(A)

$$n_{air}<n_{glass}<n_{liquid} \qquad\qquad n_{air}<n_{glass}>n_{liquid}$$

$$48.1\,° \qquad\qquad 48.1\,°$$

$$(B) \qquad\qquad (C)$$
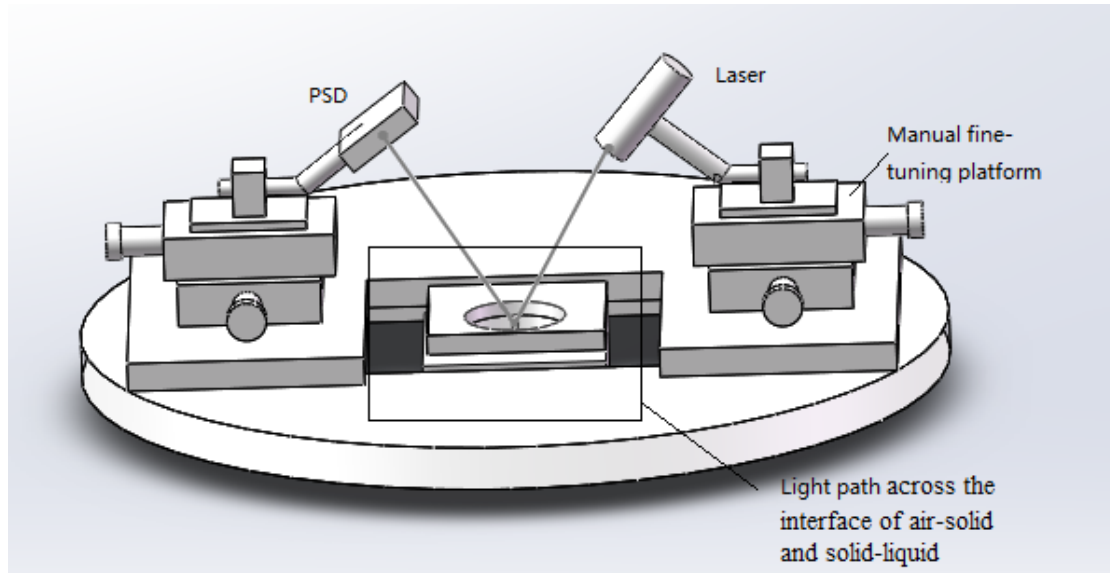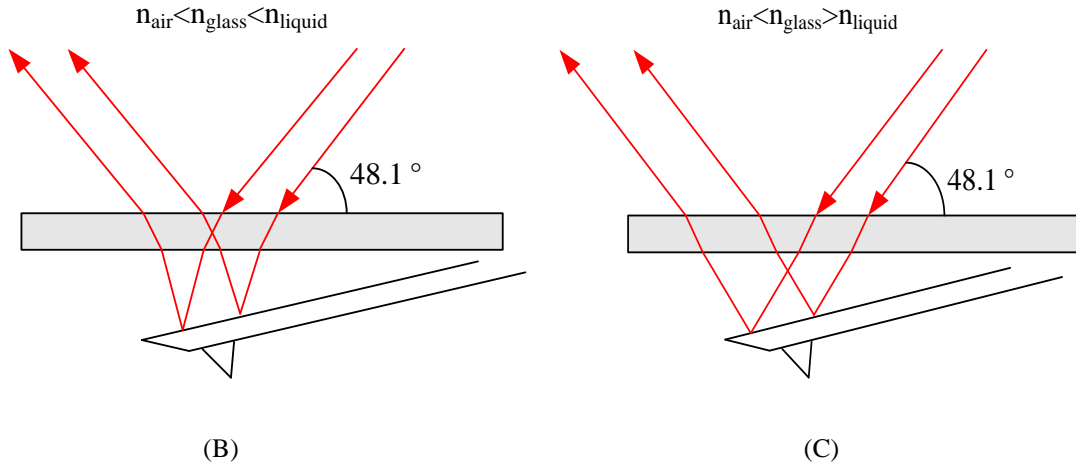
Figure 3.10 Schematic of light path passing through the silica glass into the liquid, reflecting from the cantilever, and falling onto the PSD. The refractive index range of solutions is 1.33~1.72 and the refractive index of silica glass for the laser with the 650nm wavelength is about 1.456. (A) The overall structure diagram. (B) The schematic of light path when $n_{air}<n_{glass}<n_{liquid}$. (C) The schematic of light path when $n_{air}<n_{glass}>n_{liquid}$.

According to the principle of optical lever, the magnification of cantilever deflection on the PSD can be expressed as

$$\begin{cases} 2(Q_1 + Q_2) = \dfrac{L_2}{R} \cdot \dfrac{180}{\pi} \\[2mm] Q_1 = \dfrac{L_1}{R'} \cdot \dfrac{180}{\pi} \end{cases} \tag{3.1}$$

where Q_1 is the slant angle of the probe relative to the horizontal plane and here is 11˚, R' is the length of cantilever, R is the distance between the laser and the probe, Q_2 is the deflection angle of the probe when it scans the sample. L_1 and L_2 are the radians of the deflection of probe and the whole deflection, respectively. Hence, the magnification of cantilever deflection on the PSD can be expressed as

$$A \approx \frac{L_4}{L_1} = \frac{2R}{R'}$$

(3.2)

where L_4 is the displacement of light spot on the PSD. The length of cantilevers which usually used in the experiments is 100μm or 200μm. Hence, the corresponding magnification is 500× or 1000×. The vertical resolution is better than 0.1nm. As shown in Figure 3.11, it is the overview of the photoelectric detection system which can be used both in air conditions and liquid environments and the CCD performance in real time.

(A)   (B)
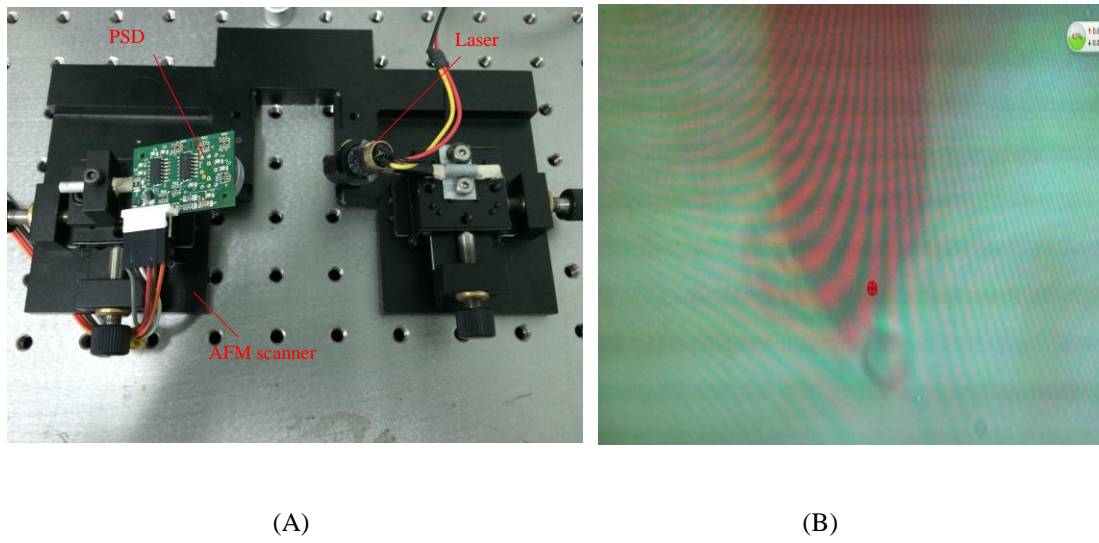
Figure 3.11 Schematic of the photoelectric detection system (A) and the CCD performance in real time (B).

3.4 Development of Micro/Nano Feed Mechanism

The micro/nano feed mechanisms consist of an adjustment micro displacement platform and an adjustment nano displacement platform. They are used not only as the tools for the scanning of sample morphology and the movement of sample in a large area, but also as a sample stage for the sample scanning applied in this design. The adjustment micro displacement platform is composed of three high-accurate electrically-controlled micro displacement platforms which apply the

high-resolution DC motor driving translation stages with the models of M-126.CG1 and M-112.12S manufactured by PI (Physik Instrumente). Three dimensional micro displacement platforms after combination are used to provide the scanning area of the nano displacement platform, and locate the position of sample or probe. The travel ranges of three axes are all 25mm. For the manipulation of samples, the micro-displacement platform is to improve its resolution and repositioning accuracy. Since the Z axis is used for the micro-focusing of optical microscope and the rapid insertion of probe, the relative resolution and repositioning accuracy of Z axis displacement platform should be superior to those of X-Y axes, so as to avoid the damage of probe in case of over adjustment and rapid insertion. In this system, it is not suitable to select a large Z axis displacement platform due to the limitation of the working space, so we select the product M-112.12S, which meets both the design requirements of the system parameters and the space.

The nano displacement platform selected in the system is a three-dimensional PZT actuator with the model of P-561.3CD manufactured by PI company and its inside applies a flexure hinge structure design to ensure that the return difference approaches zero value. The nano displacement platform is mainly used to carry and drive the sample to implement the 3D movement that accomplishes the morphology imaging and the characterization of samples. The travels of the three axes are 150μm×150μm×150μm in the open loop. Since the system is mainly used for the characterization and the detection of morphology and mechanics in biomedicine, the larger travel on the Z axis is helpful for the measurement of the characteristics of biological samples. The resolution of this piezoelectric ceramic displacement platform under the condition of open loop can reach 0.2nm and meet the needs of the surface morphology of biological sample and the characterization of mechanics, as shown in Table 3.3 for the specific parameters. Three-dimensional adjustment micro/nano displacement platforms can be combined into the functions of scanning and positioning for the micro/nano feed mechanisms.

Table 3.3 Specifications of micro/nano displacement platforms.

Translation stage	Active axes	Travel range	Max. load	Unidirectional repeatability	Feedback controller
M-126.CG1	X/Y	25mm	200N	1μm	Open loop
M-112.12S	Z	25mm	30N	0.1μm	Open loop
P-561.3CD	X, Y, Z	150μm×150μm×150μm	50N	2/2/4nm	Open loop

For the controllers of the micro/nano feed mechanisms, C-663 mercury step controller and C-863 mercury servo controller from PI company are used to control the movement of M-126.CG1 and M-112.12S micro-displacement platforms, respectively. Furthermore, the nano displacement platforms in the system E501 modular piezo controller from PI are also used. This system selects amplifier module to integrate into the controller, with an output voltage range of -20~120V.

3.5 Development of the External Devices and the Human-Machine Interface

The mechanical elements such as the micro/nano feed mechanisms are controlled by computer with D/A and A/D converters which used to collect the PSD output data synchronously. Among which the A/D converter with the model of USB-7646B manufactured by ZTIC (Beijing Zhongtai Yanchuang Technologies) is used to convert three input analogue signals to three digital signals. 16 effective bits for input frequencies up to 400KHz can satisfy the requirements of data collection from the PSD ($\pm$5V). The D/A converter with the model of PCI2303 made by ATD (Beijing Art Technology Development) which has 16 effective bits for four output voltages of 0-10V. Hence, the resolution of PZT actuator on the Z axis can be achieved. Moreover, the conversion time of the D/A converter should not be more than 10μs, and has a statistical time delay function with the accuracy up to 100ns. Table 3.4 shows the specific parameters of the D/A and A/D converters.

Table 3.4 Specifications of D/A and A/D converters.

	Resolution	Sampling rate	Port number for input/output	Voltage Input/output	Conversion method	Bus type
A/D	16bit	400K	16 for input	±10V/±5V for input	Software triggering	USB2.0
D/A	16bit	≤10μs	4 for output	0～10V/ for output	Software triggering	PCI

The secondary development for both D/A and A/D software can be applied to run on PCs under the Microsoft Windows XP/2K/7, and the development of the human-machine interface system with the control software will be described in Section 3.6

3.6 Development and Optimization of Feedback Control System

In addition to the design of physical structure, we also use the feedback control system to improve the imaging quality. The feedback control system is a closed-loop control system formed on the basis of feedback control principle. As shown in Figure 3.12, the feedback control system has four fundamental parts in the design, namely the controlled process, sensor device, actuator and controller. Among them, the controlled process refers to the AFM system built above, which is immutable, the sensor device refers to the above mentioned detection of the force on cantilever, the actuator refers to the part of actually executing control orders, which is the nano displacement platform, and the controller refers to the digital PID controller, which will be introduced in details below. It is mainly used to control and calibrate the behaviors of actuator through the programmes. With the adjustment of feedback control system, AFM can reduce or remove the deviations and improve the stability, the response speed and the accuracy of system.
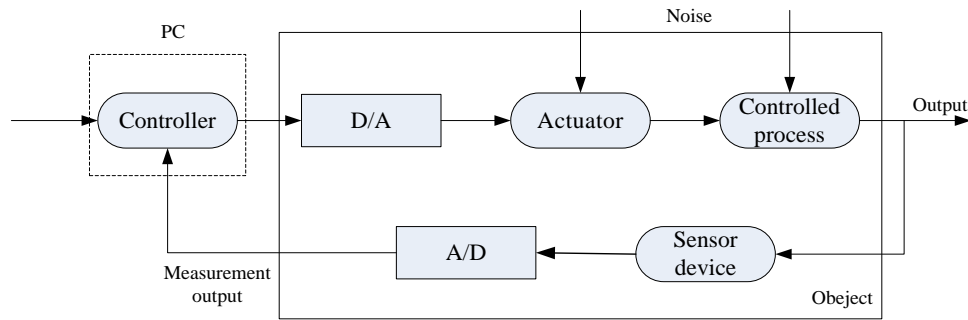
Figure 3.12 Block diagram of the feedback control system.

The concept of PID (Proportional-Integral-Derivative) controller was proposed by American scientist in early 1920s. Compared with other controllers or control systems, PID controller has several advantages, such as easy to use, convenient setting of parameters, good adaptability and robustness. It is rapidly and widely adopted in industrial applications and then gradually developed into a complete set of the control method. With the continuous improvement of computer technology, the current PID controller has been developed into the analog and digital ones. Analog PID belongs to the conventional control instrument of "hardware"; while digital PID is realized through the computer "software" programming, which has stronger flexibility and more convenient upgrading.

According to the principle of the atomic force microscope, in the topographical process of sample, the scanning device needs to be controlled by the computer to track the surface of the sample. Then, 3D topographical information of the sample can be obtained. The computer controller can calculate the amount of control according to the deviation of the sampling values. Hence, the traditional PID control algorithm is unworkable to meet the requirements. As shown in Figure 3.13, the digital increment PID controller has been presented. The process of analysis for designing a digital implementation of the PID controller is shown in the following. The deflection signal of cantilever is received by PSD and is transformed into its corresponding voltage signal through the preamplifier circuit, and then after the transformation of A/D converter, the digital signal is

calculated by the discrete PID control algorithm in the controller. The calculated data will be transformed into the analog signal through the D/A converter. Moreover, through the power amplifier, the nano displacement can be realized.
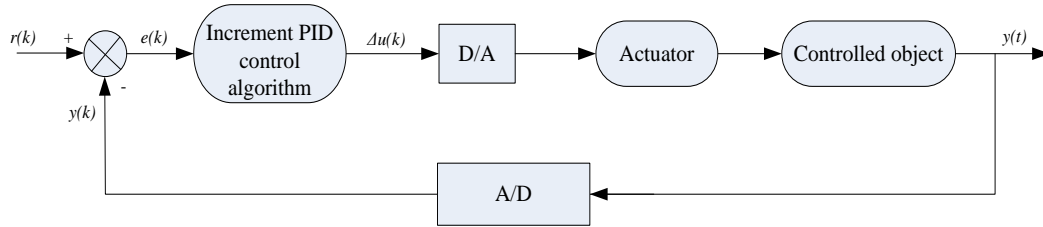
Figure 3.13 Block diagram of the increment PID controller.

The digital PID controller based on the software requires the standard form of the PID controller to be discretized. With a sampling time kT represented the continuous time, the integral term which approximations for the first-order derivatives made by backward finite differences is discretized, as follows

$$\begin{cases} \int_0^t e(t)dt \approx T\sum_{k=0}^{n} e(k), t \approx nT \ (\ n = 0,1,2,...); \\[2mm] \dfrac{de(t)}{dt} \approx \dfrac{e(k)-e(k-1)}{T} \approx \dfrac{\dfrac{e(k)-e(k-1)}{T} - \dfrac{e(k-1)-e(k-2)}{T}}{T} \\[2mm] = \dfrac{e(k)-2e(k-1)+e(k-2)}{T^2}; \end{cases} \tag{3.3}$$

Then the difference equation for the digital PID controller can be written as[94]

$$u(k) = k_p e(k) + k_i \sum_{j=0}^{k-1} e(j) + k_d \frac{e(k)-e(k-1)}{T} \tag{3.4}$$

Where $k_i=k_p/T_i$, and $k_d=k_p \times T_D$. T is the sampling period. k is the sampling number, and $e(k-1)$ and

e(k) are the deviation signals at the time *(k-1)* and the time *k*. Since the output of the digital PID controller is related to the output in the last time, *u(k)* is possible due to the jumping phenomenon for some unexpected reason. Then the suddenly jumping in the voltage output for the nano displacement platform will damage the probe and the sample. Hence, an increment PID control algorithm is implemented further.

From Eq. (3.4), we can obtain[94]

$$u(k\text{ - }1) = k_p e(k\text{ - }1) + k_i \sum_{j=0}^{k\text{-}1} e(j) + k_d \frac{e(k\text{ - }1) - e(k-2)}{T} \tag{3.5}$$

Then, Eq. (3.4) minus Eq. (3.5), the control increment can be expresses as[94]

$$\Delta u(k) = k_p \Delta e(k) + k_i e(k) + k_d \frac{e(k\text{ - }1) - e(k-2)}{T} \tag{3.6}$$

where $\Delta e(k) = e(k\text{ - }1) - e(k-2)$

Hence

$$\Delta u(k) = u(k) - u(k-1) = k_p[e(k) - e(k-1)] + k_i e(k) + k_d[e(k) - 2e(k-1) + e(k-2)] \tag{3.7}$$

The development of PID controller needs to estimate the values for finding out the optimal parameters, namely k_p, k_i and k_d. The proportional value reflects the instantaneous size of deviation (error). When k_p is too small, the ability of proportional control adjustment is weak. When k_p is appropriate, the deviation value of the system decreases so that the response speed and the accuracy increase. When k_p is too big, it tends to make the system unstable.

The integral reflects the "memory" of historical value of deviation and this control is used to

eliminate the system deviation. When k_i is too small, it can result in system instability. When k_i is in a certain range, the bigger its coefficient is, the higher the system accuracy is. When k_i is too big, it has a poor effect of integral control.

The derivative reflects the change of deviation value and this control is some kind of "forecast" for the change of deviation, thus it is used to generate advanced correction action. When the rate of change of deviation is relatively small, the derivative control is basically invalid. When the deviation value approximates to zero, namely the system is stable, and the derivative is zero. When the rate of change of deviation is relatively big, the derivative has a strong control effect. However, it is easily for the actuator to enter into the saturation, thus to fail the desired effect. The process of searching for the optimal k_p, k_i and k_d is given in Figure 3.14. The ranges of initial values are started as k_p [0.001-0.1], k_d [0.01-0.5], and k_i [0.01-1].
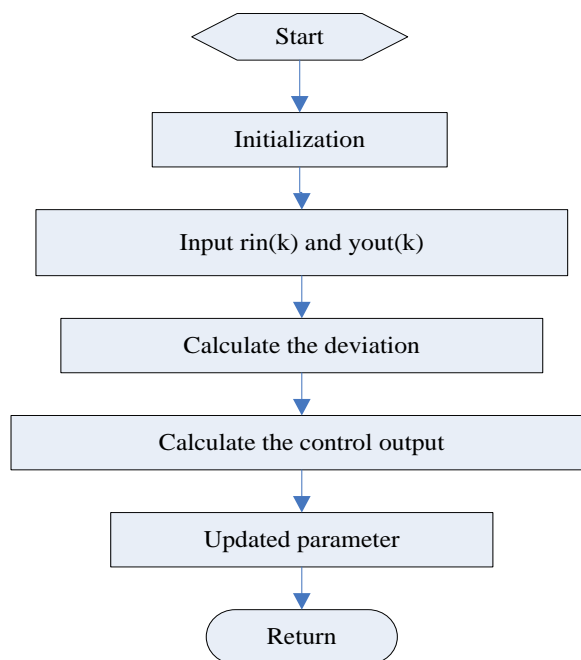
Figure 3.14 Sequence diagram of the increment PID control programme.

According to the increment PID control programme, the step signal of the discrete system was

simulated by Matlab. Then, the optimal parameters could be obtained as three criteria, such as the minimum overshoot, and the minimum error in the minimum response time.

(A)   (B)
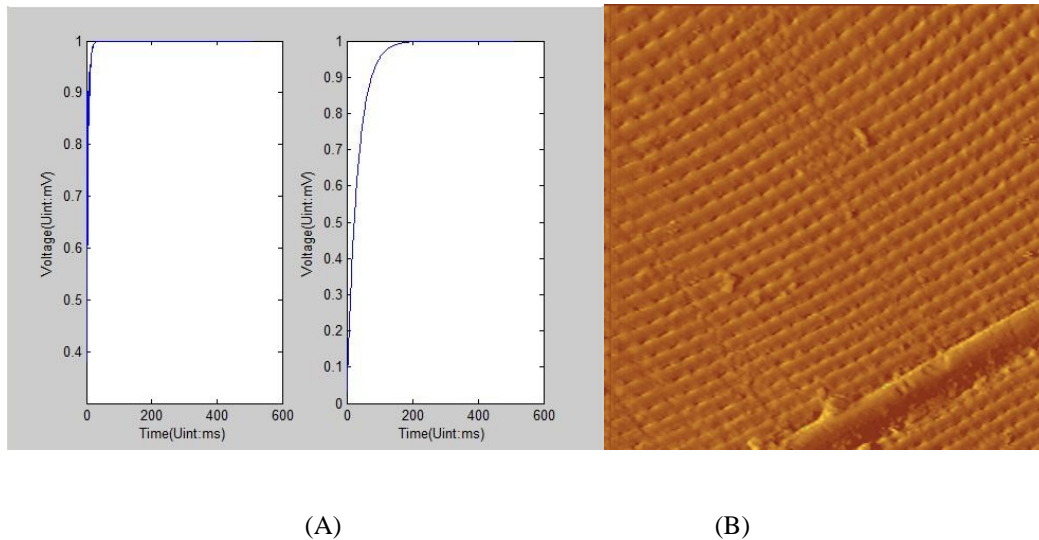
Figure 3.15 The simulation result and the experimental result. (A) The simulation result performed by MATLAB: the left is the input and the right is the output. (B) The experimental result.

The parameters k_p, k_i and k_d were assigned with different values in the reference range as mentioned earlier, and used to check the overshoot in system responses. Then, a good simulation result was obtained, as shown in Figure 3.15 (k_p=0.1, k_i=0.3 and k_d=0.01). However, when applying the obtained PID parameters in the experiments, the oscillation in the error signals is observed and the imaging performance is out of quality. As shown in Figure 3.16, there is a large irregular stripe covering the initial standard 2D grating, and a blurred, poorly contrasted pattern is displayed on the right-hand side of the diagram.
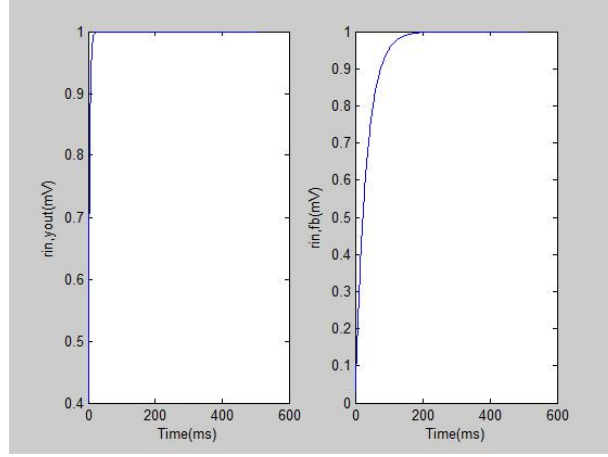
Figure 3.16 Simulation result performed by MATLAB: the left is the input and the right is the output.

(A)   (B)
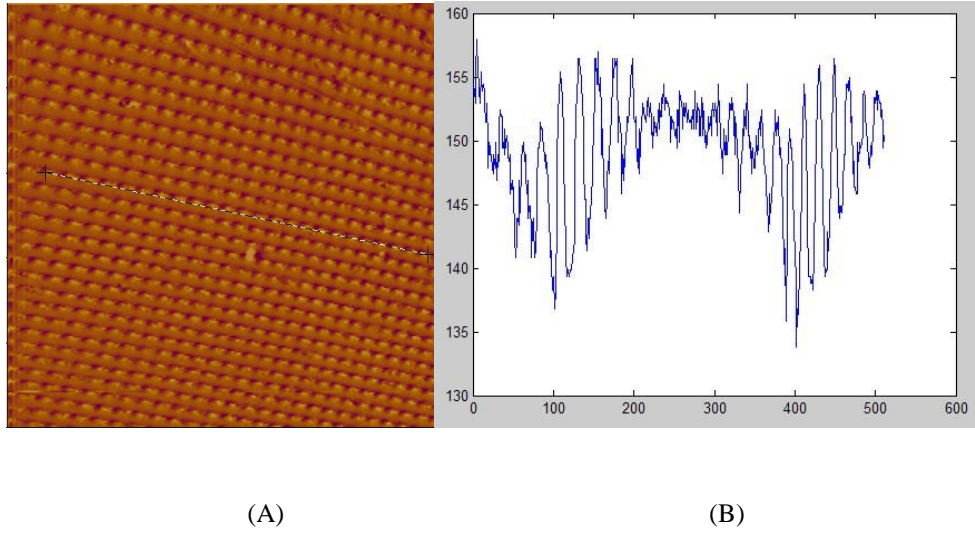
Figure 3.17 Topography of a 2D grating (A) and the cross section through the pattern (B).

Then, k_p=0.05, k_i=0.3 and k_d=0.01 were applied in the experiments. The tracking speed becomes fast that the steady state error is displayed smaller than the previous experiments, as shown in Figure 3.16. Besides, the standard 2D grating (material: silicon) was used as the sample in the liquid environment, as shown in Figure 3.17, which was scanned by the contact mode with AFM in two different liquids: water and culture (including about 30 different ingredients). In order to avoid the influence of the cantilever dynamics, the cantilever with the nominal spring constant of

k=0.2N/m, length of L=450μm, thickness of H=50μm, and the free resonance frequency of f=300kHz was used. The scanning area was 80μm×80μm, and the scanning mode was the contact mode.
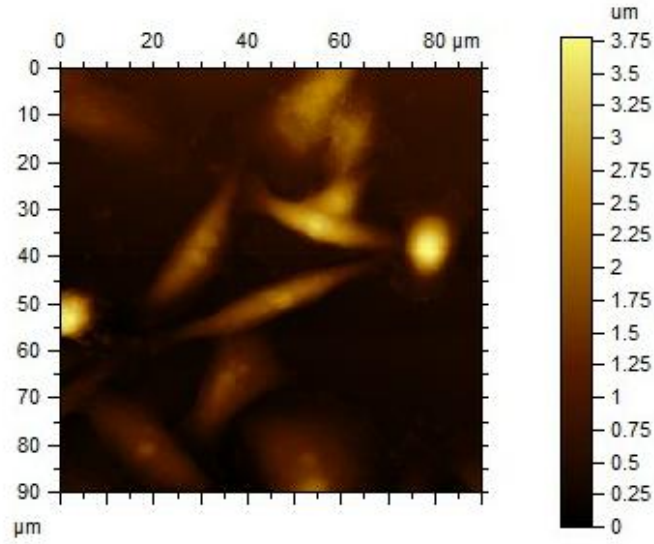
(A)
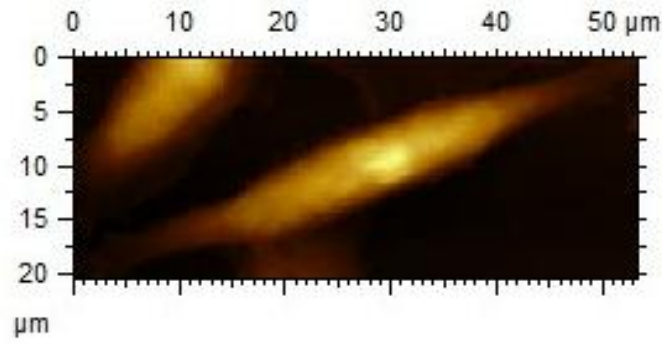
(B)

Figure 3.18 AFM images of colon cancer cells SW480 in the air, obtained in the contact mode with the cantilever (k=40N/m, f<300kHz).

Applying the obtained PID parameters to the topography of biological cells in the air conditions, the results were obtained as given in Figure 3.18. The colon cancer cells SW480 of about 25μm in length with the typical fusiform structure and the highest point of 3.08μm could be clearly seen in Figure 3.18(A). Because the cells were scanned in the air conditions and then they showed the fusiform type. The direct cellular damage exists in the imaging and it is formed by the shifts of solute-solvent, which causes the cell dehydration. In these studies, the PID parameters can be changed in real-time while the system is in operation.
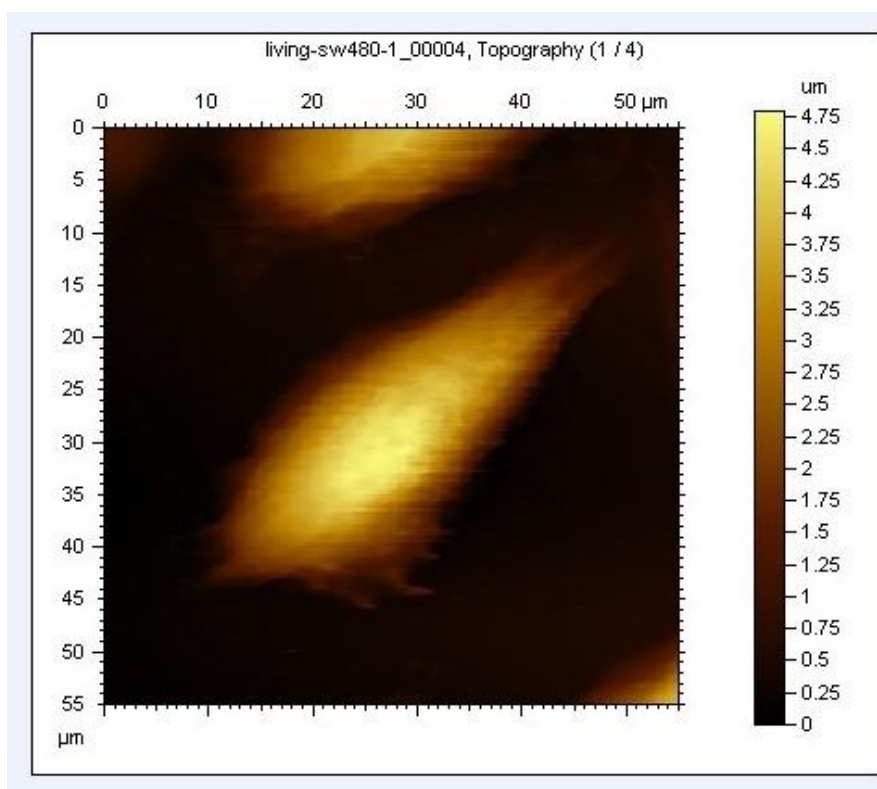
Figure 3.19 AFM image of colon cancer cells SW480 in culture, recorded in the contact mode with a soft cantilever (k=0.01N/m, f<300kHz).

Applying the obtained PID parameters to the biologic cells scanning in culture, the result was obtained as shown in Figure 3.19. The colon cancer cells SW480 of about 40μm in length with the typical fusiform structure of the highest point of 4.08μm can be clearly seen in the figure. The

topographical image has been improved in contrast and displayed more details of the banding pattern. A minimum overshoot in each movement of the nano displacement platform can avoid the excessive damage to the cells which performs more flimsy than the standard 2D grating samples. The fact that the feedback controller still reacts at the large size (close to $150\mu m^2$) offers an enough area to show the cell clusters. The experimental results show that the AFM system works well in both the liquid environment and the air conditions. The variable parameters of the PID controller can improve the image quality and the image contrast.

3.7 Development of Scanning Software

Based on the design of AFM structures, the human-machine interface system is developed under Microsoft windows 7. It mainly includes the programme development for A/D and D/A converters which have been described above, and the programme development for the PI devices and the control programmes for operations.

3.7.1 Software Development to Micro Feed Mechanism

This part is mainly used for the secondary development of three micro-displacement platforms. As shown in Figure 3.25, it is the flowchart of the control for the PI devices. Once the programme is launched, a modal dialog box with the selection of connection parameters is given. After setting the corresponding communication port and baud rate, click on the button 'Connect', the connection function will be executed, and the communication between the computer and the micro-displacement stage is established. The return value is zero for a successful communication. An integer variable is defined in this programme to store the connection state.
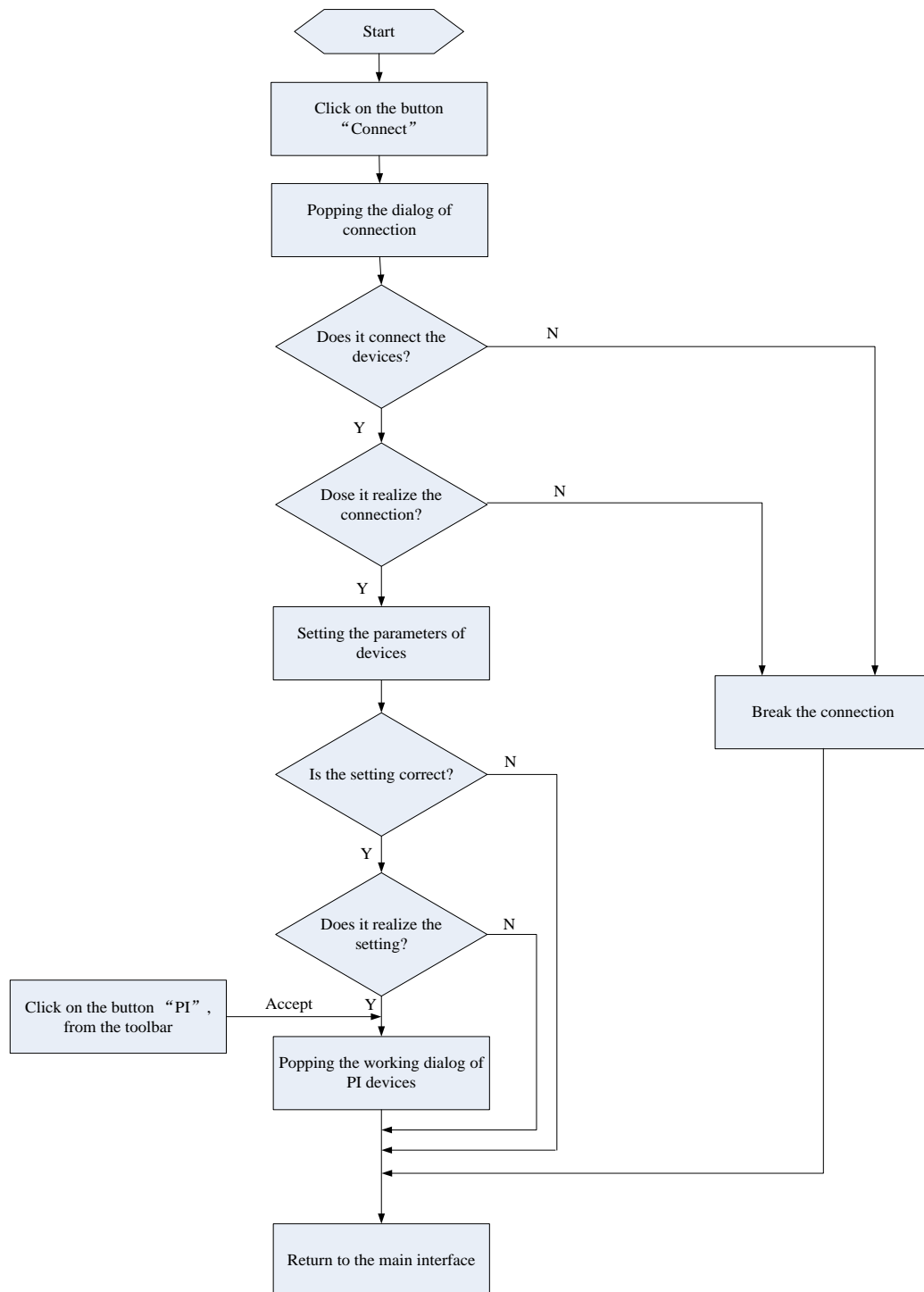
Figure 3.20 Flowchart of the control of micro feed mechanism.

Since the connection is accomplished, click on the button "PI" from the toolbar, then the working

dialog of PI devices pops up, as shown in Figure 3.21. Then, three micro displacement platforms can be operated to reach the place of destination. In general, the initial places of three platforms should be the same as the places recorded before we exited out of the application in the last time. If the position information is inconsistent, then the buttons of "Pos. Limit", "Neg. Limit" and "Reference" can be clicked to reset the platforms to the positive limit position which are the maximum displacements of three platforms, the negative limit position which are the minimum displacements of three platforms and the reference position set to 12.5mm by the manufacturers.
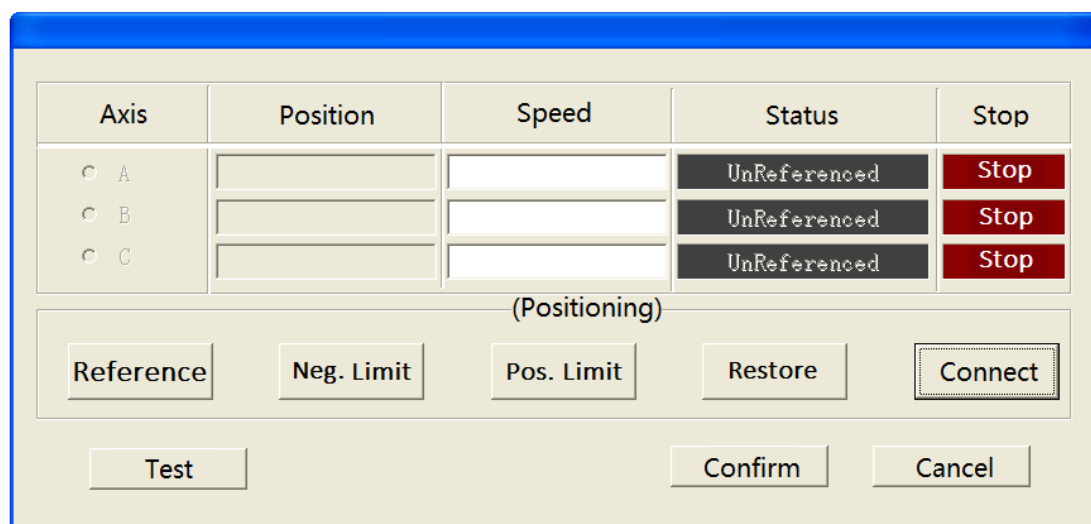
Figure 3.21 Schematic of the software of micro feed mechanism interface.

3.7.2 Design for Control Programmes

In the AFM feedback system, the control programmes are mainly divided into the following parts, namely the initialization, sample approaching, scanning, sample withdrawing and equipment releasing. The designs of those control programmes are briefly introduced below. As shown in Figure 3.22, it is the human-machine interface of the control programme, including the setting area of the scanning parameters, the display area of feedback data, the setting area of PI parameters, the display area of sample imaging in real time, the buttons of system functions, the display area of history images, and the display area of scanning curve with each line in real time.

From the setting area of the scanning parameters, the parameters including the scanning area, proportional gain, integral gain, *Setpoint* and scanning frequency can be set for the measurement and handling of samples.
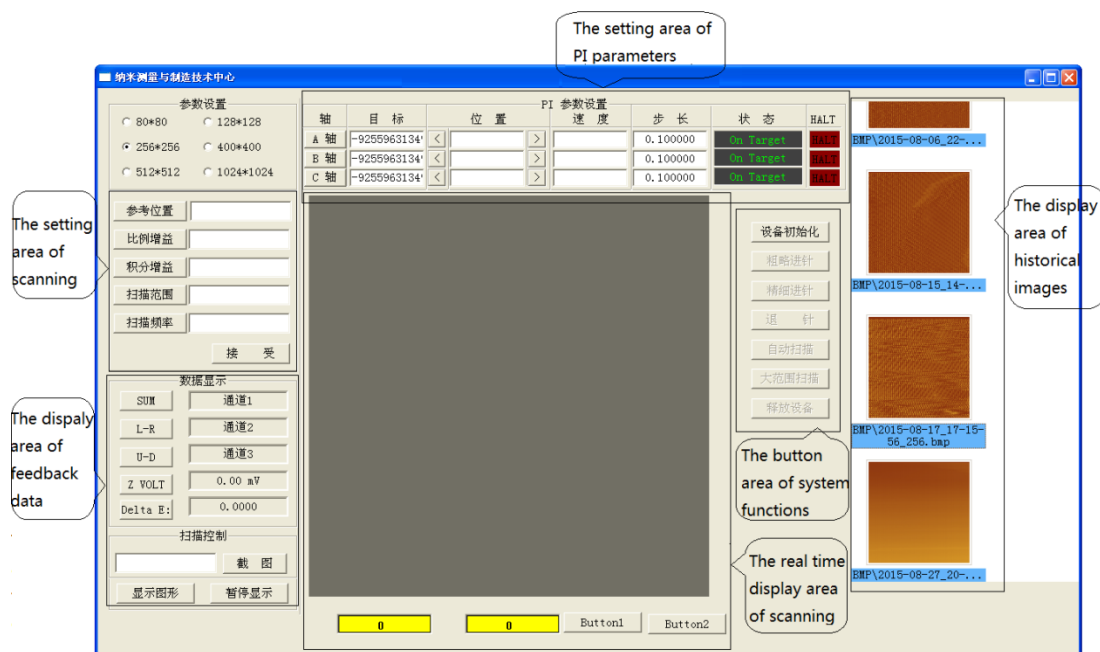
Figure 3.22 Schematic of the human-machine interface.

3.7.2.1 Design for the initialization programme

The initialization part decides whether the programme can start running smoothly or not. In this part, it is mainly used to initialize the A/D and D/A converters, and the corresponding initialization programme is provided by the manufacturers. In addition to defining and distributing the variables, and give an initial value, it needs to call the functions of USB7646B_OpenDevice() and USB7646B_ADInit() of A/D card to accomplish some important operations, including the device enabling and the setting of variables. While the initialization for D/A card, it requires to call the functions of PCI2303_CreateDevice() and PCI2303_InitDeviceProDA() to create the device object, judge whether the device object is valid or not, and select the relay to realize the output of D/A converter. Moreover, the micro displacement platforms also need to be initialized to make

them at the initial positions. Before the completion of the initialized operations, all of the function buttons are disabled.

3.7.2.2 Design for the sample approaching

The sample approaching programme aims to make the probe approach to the sample within a given distance of nanometers before the scanning of AFM. Therefore, the successful sample approaching is important since it directly determines if the AFM can accurately detect feedback signals and implement the work normally. As shown in Figure 3.23, it is the flowchart of the sample approaching of AFM system. When the system begins to make the sample approach to the probe, some local variables are required to be firstly defined and initialized for the data acquisition and processing of A/D converter. Then it is required to judge if the up-down voltage signal outputted by the PSD reaches a certain range. If it is not in the range, the control voltage on the Z direction of micro displacement is increased, which is from the conversion by D/A, then the nano displacement platform in Z direction is driven to move, thus to make the sample approach to the tip of probe gradually until it reaches a given distance, and this is the end of probe insertion programme. In the design of the control programmes, multithread programming and overvoltage protection are applied respectively, which can stop the sample approaching, sample withdrawing or release equipment before the completion of sample approaching and a maximum voltage output of 6V with the nano displacement platform in the Z direction will prevent the damage of probe.
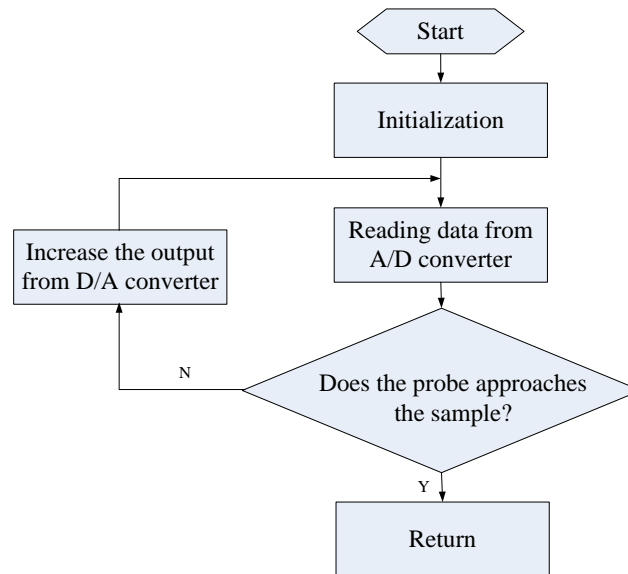
Figure 3.23 Flowchart of the sample approaching programme.

3.7.2.3 Design for scanning programme

The scanning programme begins after the completion of sample approaching. During the scanning process, the implement of sample imaging and adjustment of the position of sample in real time are performed through accurately detecting feedback signals and implementing series of data processing. Therefore, in the AFM system, real-time sample imaging can intuitively reflect the quality of feedback signals and the effects of system control. As shown in Figure 3.24, the scanning of AFM includes the fast scanning (X direction) and the slow scanning (Y direction), so the scanning programme also includes the control programmes of X direction scanning and Y direction scanning. Moreover, this thesis refers to the scanning from the initial point to the end point of each line as the trace scanning and refers to the scanning from the negative direction of each line as the retrace scanning.
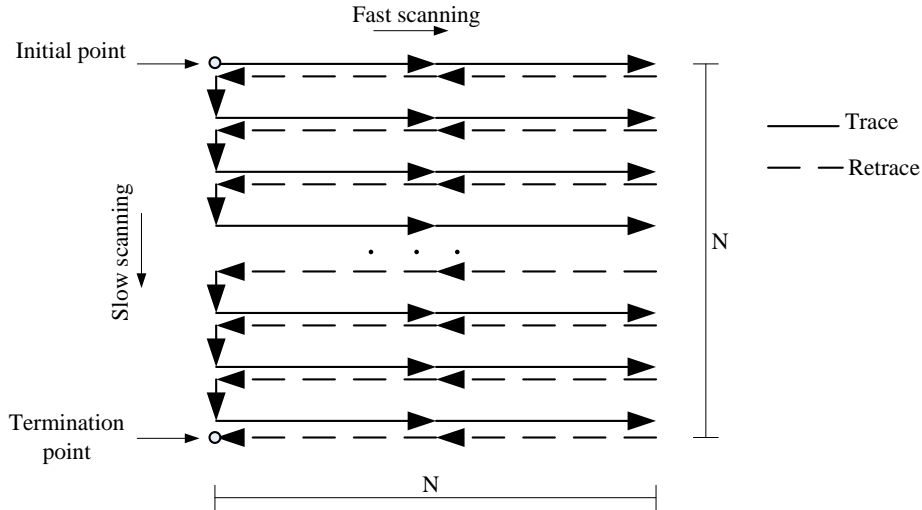
Figure 3.24 Schematic of the scanning path of AFM.

The local variables of F_ScanDir and S_ScanDir are defined to control the variables of fast scanning and slow scanning respectively. N×N is the scanning resolution which is set in the area of the scanning parameters. As shown in Figure 3.25, it is the flowchart of the scanning programme. At the beginning of scanning, the column loop is firstly started until the control variable in the slow scanning direction equals to 0, then the row loop is started until the control variable in the fast scanning direction also equals to 0. At this time, the scanning programme is implemented with the setting parameters until the probe reaches the termination point. After the completion of scanning, the sample can usually be withdrawn. If the scanned image is not good, the sample position can be readjusted and then the system continues to implement the sample approaching and scanning. The scanning suspension and the sample withdrawing can be implemented at any time and any place in the scanning process.
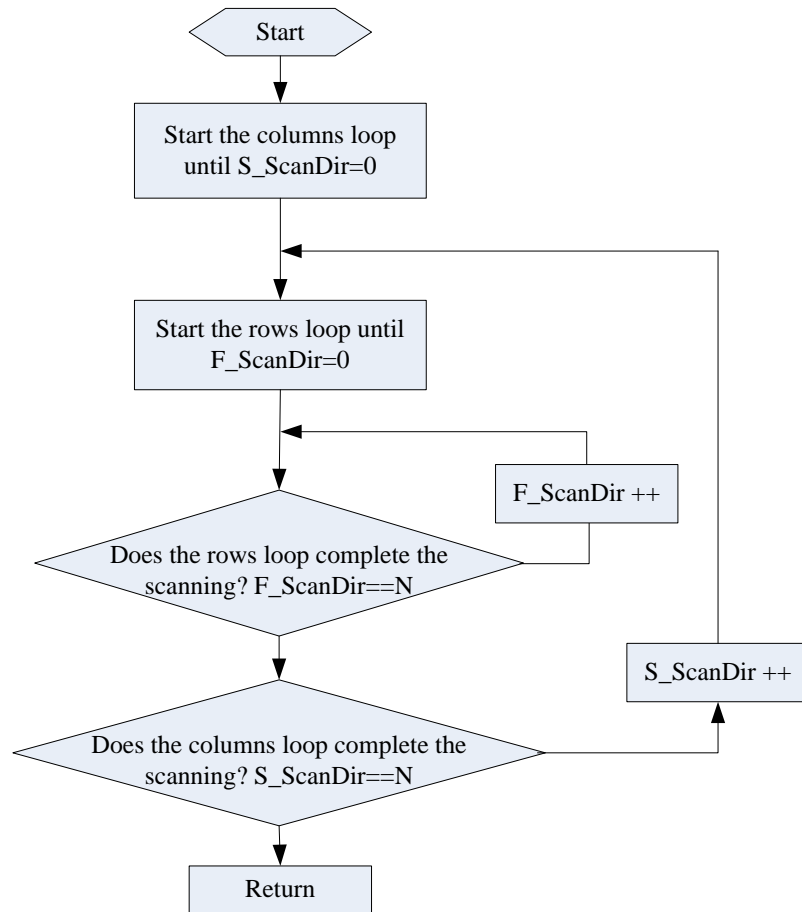
Figure 3.25 Flowchart of the scanning programme.

3.7.2.4 Design for the sample withdrawing and equipment releasing

The sample withdrawing makes the sample gradually get away from the probe in the *Z* direction. It is the opposite process of sample approaching. With respect to the control programme, the sample withdrawing is a little easier than the sample approaching, because it does not need to consider the collision of probe and sample.

When implementing the operation of releasing equipment, the operator ends up all tasks of AFM and makes the AFM system reset or return to zero. On the whole, the equipment releasing programme is almost the same as the sample withdrawing programme. Two global variables are defined in the programme of sample approaching and the scanning programme, respectively. The

initial position of sample withdrawing is given by the defined global variable. Furthermore, equipment releasing includes two parts. Operation of A/D mainly refers to calling the function of USB7648A_ADStop() to stop A/D acquisition and calling the function of USB7648A_CloseDevice() to shut down the A/D equipment. While the operation of D/A mainly refers to calling PCI2303_ReleaseDevice() function to release the D/A equipment.

3.8 Summary

In this chapter, based on the principle of atomic force microscope and its applications in the field of cytology, the liquid-AFM has been developed and optimized. This system aims to overcome the shortcomings in current research such as the insufficient area in the sample scanning, the inefficiency and less reliable in the scanning of living biological samples and the incompatible AFM probe unit that cannot be used in the air conditions and liquid environments in one system. Hence, a novel liquid-AFM probe unit has been established to decrease the evaporation of liquid, avoid the influence between the surface tension and the probe, remove the surface movement of liquid, eliminate the air bladder, and make the cells survive for a long time while they are measured and manipulated. This structure is suitable for the topography of the cell samples in the air condition and liquid environment. Furthermore, the increment PID control has been presented to avoid the damage of probe, and the optimal PID parameters for the scanning of biological cells have been simulated and experimented both in the air condition and in culture, thus to improve the working efficiency and the accuracy of micro/nano manipulation. Finally, a human-machine interface system with the control software has been developed. Multiple modular constructions have been realized in the software of control system such as the secondary development to A/D, D/A converters and PI devices, the control programmes with the sample approaching, the scanning control, the sample withdrawing and the equipment releasing. It lays a firm foundation for the nano handling and measurement of biological cells and the applications of the liquid-AFM for biological cells will be described in Chapter 4.

Chapter 4

Nano Handling and Measurement of Biological Cells Based on

Liquid-AFM

The morphological structures and functions of cells, the cell growth, development, maturity, proliferation, senescence, death and carcinogenesis, differentiation and their regulation mechanism are related to the mechanical properties of the cells. The force and deformation of the membrane have direct impact on the realization of their functions[95][96]. In the nano handling and measurement of biological cells in culture, one or two kinds of changes in different shapes can significantly mark the growth state of the living cells and provide more information to the clinical diagnostics. Therefore, the demand for the analysis of living cells on the micro/nano scale is an increasing trend for both fundamental biology and clinical diagnostics. In the previous chapter, a liquid-AFM has been developed and optimized to overcome the shortcomings in current research. The following sections describe several applications of the liquid-AFM for biological cells, including the cell imaging in different liquids, studying of mechanical properties of cells in culture and cellular shear adhesion force measurement.

4.1 Imaging of Cells Based on Liquid-AFM

In recent years, the sample imaging in liquid environments has gradually become an important research topic, especially for the biological cell imaging. The measurement of living cells can provide more accurate information on the clinical diagnostics. By comparison of the imaging in air conditions, several studies have shown that the sample imaging in liquid environments can

remove or reduce several influences between the probe and the sample when they are scanned in air conditions including the capillary force and electrostatic force[97]. However, there also exist some problems in the liquid imaging, for instance the refractive index of liquid and the inhomogeneity of the liquid concentration will restrict the sample imaging with high resolution and the beam path across the interface of air-liquid will be disturbed by the surface fluctuation of the liquid. The second problem has been solved by the novel design of liquid-AFM probe unit. Hence, the biological cell imaging in different liquids has been studied to improve the image quality. In this work, the model of forces acted on different liquids has been simulated and demonstrated in the experiments.

4.1.1 Materials and Methods

4.1.1.1 Materials used in the experiments

SW480 human colon cancer cells were observed and manipulated in the experiment. The cells were passaged simultaneously in the endothelial cell basal medium (RPMI-1640) with 10% FBS and cultured in a controlled environment of 5% CO_2 at 37.5℃. The cells were cultured on a non-coated cover-slip and used for the experiment under the same condition. Those cells were separated from the same batch, and cultured in the same conditions, so that the influence of each parameter in the different topographies can be obtained. The probe of the ContGB-G type made by Bruker corporation, with the spring constant of 0.2N/m, length of 450μm and width of 50μm, is used as the measurement tool.

4.1.1.2 Modeling of the measurement of cells in different liquids

To evaluate the drag force on the rectangular cantilever, many researchers have modeled the cantilever of AFM as an equivalent cylinder, as shown in Figure 4.1, and the resulting force acted on the cantilever in the scanning direction can be expressed as[98]

$$F_d = \frac{4\pi\rho\upsilon^2(DL)}{log(\frac{7.4}{Re_d})} \qquad (4.1)$$

where L is the length of the cantilever, D is the diameter of the equivalent cylinder, υ is the speed of probe in the scanning, ρ is the concentration of the liquid and $Re_d = \rho D\upsilon/\mu$ is the Reynolds number for the equivalent cylinder, and μ is the viscosity of the liquid.
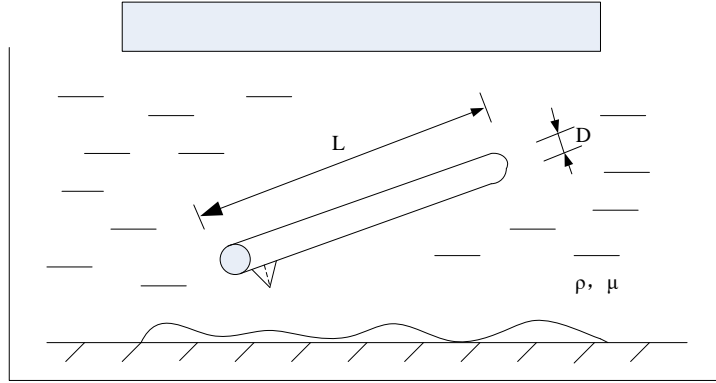
Figure 4.1 Schematic of cantilever in the liquid.

In the contact mode, the force acts on the cantilever is not only in the scanning direction but also in the friction direction when the probe approaches the surface of sample. Hence, the total resulting force acted on the cantilever when it is scanning the sample can be expressed as

$$F_T = F_d + F_f = \frac{4\pi\rho\upsilon^2(DL)}{log(\frac{7.4}{Re_d})} + \alpha F_n \qquad (4.2)$$

where α is the friction coefficient, F_n is the loading force decided by the parameter of *Setpoint*. Based on the above equations, the force acted on the cantilever is mainly influenced by the parameters of υ, ρ, μ and F_n. Hence, the different parameters are verified in the following experiments.

4.1.2 Experiments and Results

For the exploration of the imaging quality with different parameters, SW480 cells were used for the cell imaging in different liquids. Firstly, it can be seen from Figure 4.2 that the same cell was imaged in water, but with different scanning parameters. The parameters of k_p, k_i, *Setpoint* and the line rate had been assigned with different values in the reference range as mentioned in Chapter 3. Among them, Figure 4.2(A) shows the cell imaging with k_p=0.001, k_i=40Hz, *Setpoint*=0.84V (loading force=1.68×10^{-6}N) and line rate=0.6Hz, which results in the cell morphology of about 42μm in length with the typical fusiform structure of the highest point of 3μm and the image is clearly depicted but the brim has a tip toothed. Figure 4.2(C) shows the cell imaging with k_p=0.001, k_i=60Hz, loading force=1.68×10^{-6}N and line rate=0.6Hz, which results in the oscillation in the error signal that can be observed and the imaging performance in the brim is out of clearness. Figure 4.2(E) show the cell imaging with k_p=0.001, k_i=60Hz, loading force=1.2×10^{-6}N and line rate=0.6Hz, which results in a blurred, poorly contrasted cell image. The low *Setpoint* value causes the probe difficult to track the surface of the cell completely. Compared with the imaging qualities with different parameters, it can be found that the *Setpoint* value is the main influence in the cell imaging which affects the loading force F_n acted on the surface of the cell.

(A)

(B)

(C)

(D)

<center>(E)   (F)</center>
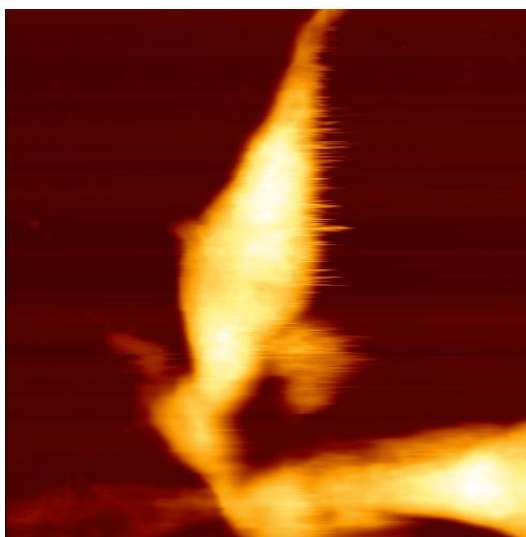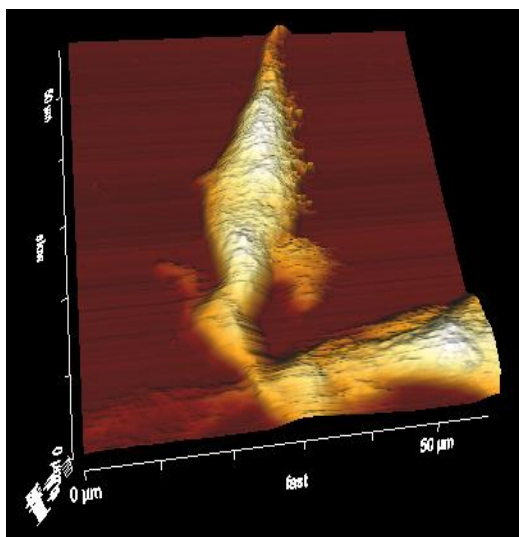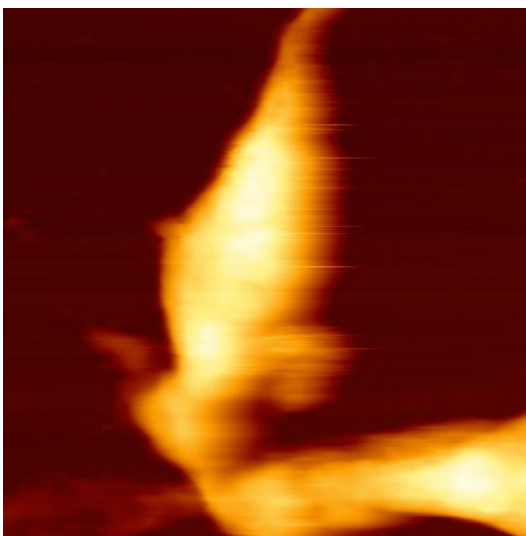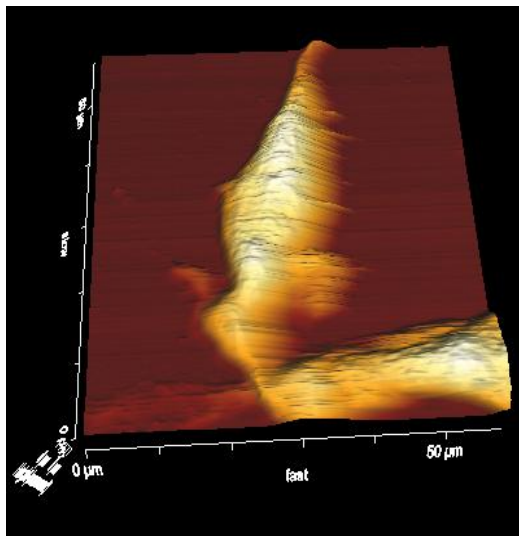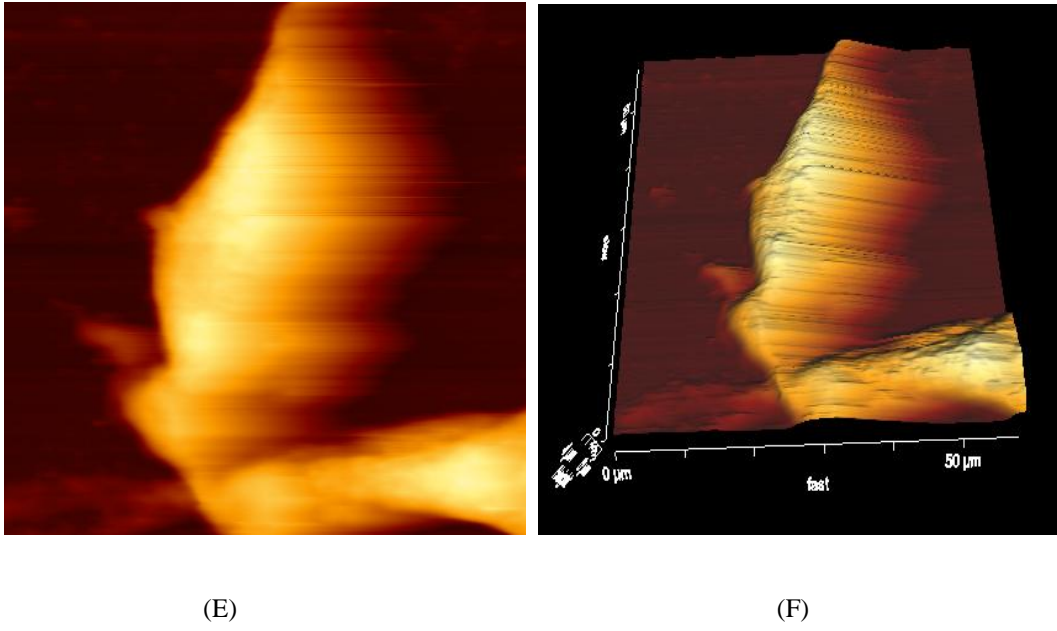
Figure 4.2 AFM image of colon cancer cells SW480 in the water, recorded in the contact mode. (A) Cell imaging with k_p=0.001, k_i=60Hz, loading force=1.68×10^{-6}N and line rate=0.6Hz. (C) Cell imaging with k_p=0.001, k_i=40Hz, loading force=1.68×10^{-6}N and line rate=0.6Hz. (E) Cell imaging with k_p=0.001, k_i=40Hz, loading force=1.2×10^{-6}N and line rate=0.6Hz. (B), (D) and (F) are the 3D views of the data of (A), (C) and (E), respectively.

Furthermore, applying the optimum PID parameters for the scanning of biological cells in different liquids, we obtained the results as given in Figure 4.3. Among them, Figure 4.3(A) shows the cell imaging with k_p=0.001, k_i=60Hz, loading force=1.68×10^{-6}N and line rate=0.6Hz in FBS. Figure 4.3(C) shows the cell imaging with k_p=0.003, k_i=70Hz, loading force=1.68×10^{-6}N and line rate=0.6Hz in RPMI-1640. Figure 4.3(E) shows the cell imaging with k_p=0.001, k_i=40Hz, loading force=1.68×10^{-6}N and line rate=1.0Hz in water. Compared with the imaging qualities in different liquids, the concentration and the viscosity of the liquid can also affect the cell imaging which conforms to all the discusses above. Then, the variable parameters of the PID controller can be used to eliminate or reduce the system deviation so that the response speed and the accuracy increase. Besides, the speed of probe in the scanning can also affect the image quality. As shown

in Figure 4.3(E), the tracking speed becomes slow and the steady state error is high at the higher line rate up to 1.0Hz. Hence, the experiments show that suitable parameters of the PID controller can also improve the image quality and image contrast.

(A)

(B)

(C)

(D)

<div align="center">

(E) (F)

</div>
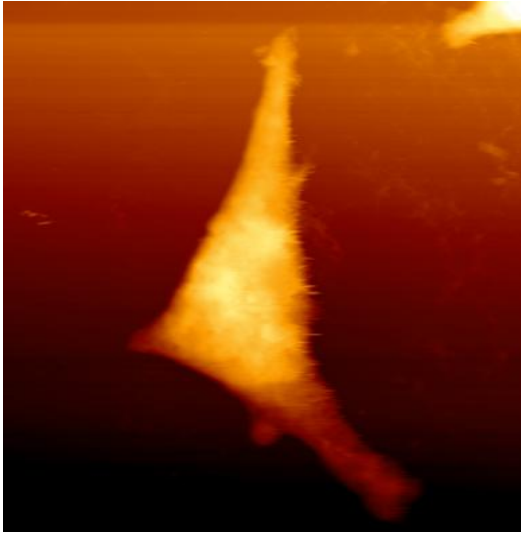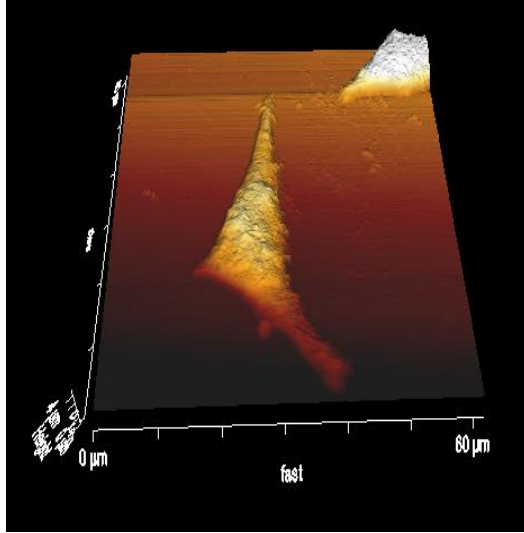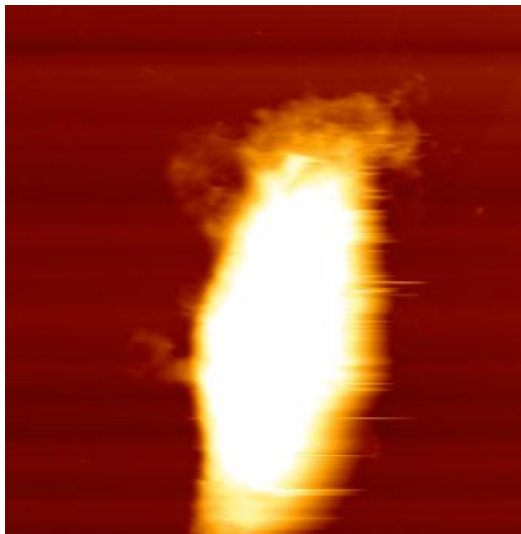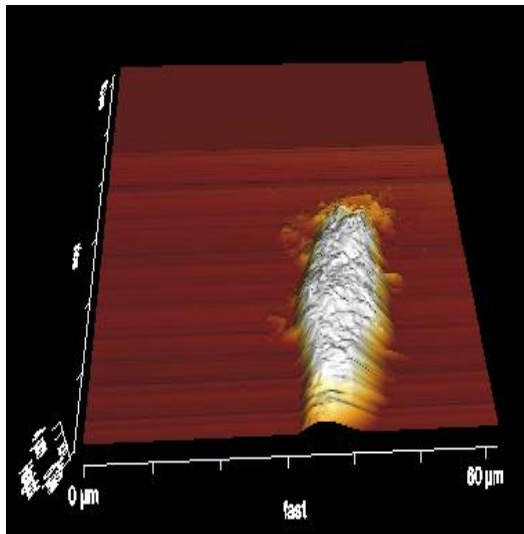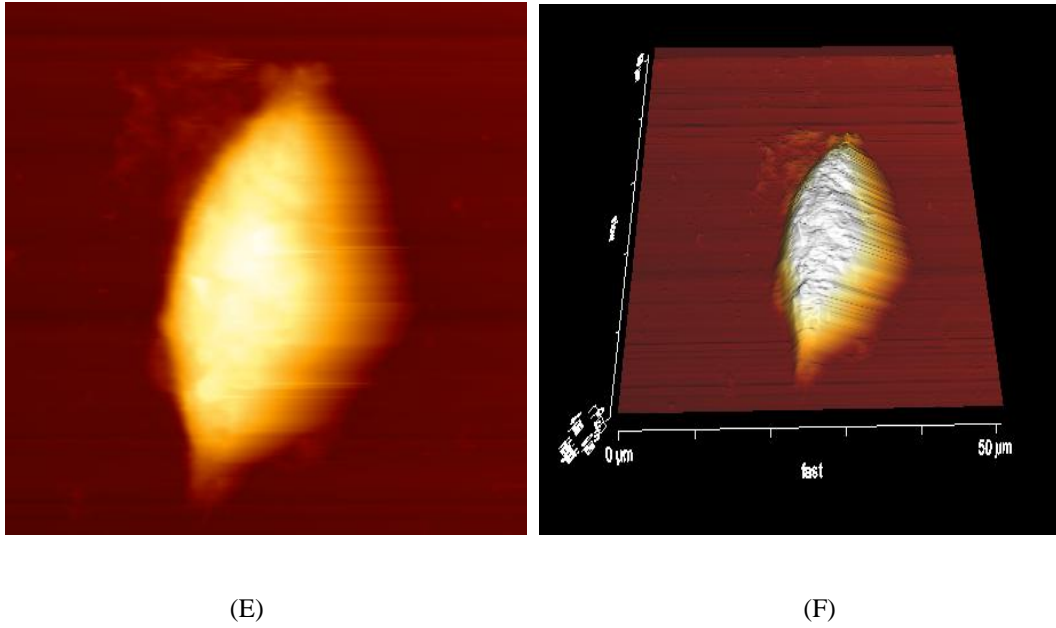
Figure 4.3 AFM image of colon cancer cells SW480 in different liquids, recorded in the contact mode. (A) Cell imaging with k_p=0.001, k_i=60Hz, loading force=1.68×10^{-6}N and line rate=0.6Hz in the FBS. (C) Cell imaging with k_p=0.003, k_i=70Hz, loading force=1.68×10^{-6}N and line rate=0.6Hz in the RPMI-1640. (E) Cell imaging with k_p=0.001, k_i=40Hz, loading force=1.68×10^{-6}N and line rate=1.0Hz in the water. (B), (D) and (F) are the 3D views of the data of (A), (C) and (E), respectively.

4.2 Study of Mechanical Properties of Cells Based on Liquid-AFM

Up to now, the studies of mechanical properties of biological cells have paid more attentions to the cell detection and observation. It can accurately measure the changes of the cell physiological state after being given various drugs. Hence, it is significant to obtain the mechanical properties for the research of cytology such as the early cancer detection, the test for the targeted therapy and the clinical diagnosis. Rogowska et al used the OCT (Optical Coherence Tomography) elastography to research the mechanical properties of phantoms and atherosclerotic arterial samples[99]. They found that OCT represents a potentially attractive and significant technique for the measurement of the tissue mechanical properties. Karimi et al used a series of uniaxial tensile

test techniques to investigate several mechanical properties of the human umbilical vein and umbilical artery such as the Young's modulus, the maximum stress and the hyperelastic material coefficient based on the UV owing to its long-term patency for CABG (Coronary Artery Bypass Graft), and those investigations have implications for interventions and surgeries[100]. However, none of these techniques can reach the nano scale in the manipulation. AFM is known both as a tool for the imaging of cells on the nano scale and as a force sensor for the measurement of mechanical properties based on the interaction between the cantilever and sample. Achterberg et al used AFM to investigate the changes of mechanical properties of dermis when the skin was aging or the tissue was remodeling[101]. The Young's elastic modulus E of human dermis is tended to increase with the age in 26-55 years old donors. Zhu et al reported a new method to determinate the mechanical properties of soft scaffold based on AFM nano indentation[102]. The data from the measurements can provide a new insight to understand the cell fate regulation.

4.2.1 Materials and Methods

4.2.1.1 Cell culture

The present work studies for the tumor necrosis factor-related apoptosis-inducing ligand (TRAIL)-induced apoptosis for the cancer cells. Two types of cancer cells were observed and manipulated in the experiment, such as SW480 human colon cancer cells and the same type of cancer cells with the immune expression of TRAIL. Those cells were passaged simultaneously in the endothelial cell basal medium (RPMI-1640) with 10% FBS (Fetal Bovine Serum) and cultured in a controlled environment of 5% CO_2 at 37.5℃. The cells were cultured on a non-coated cover-slip and used for the experiment under the same condition. The final concentration of TRAIL is 300ng/ml, and the cancer cells and cells with TRAIL were cultured for 16 to 20 hours. Those cells were separated from the same batch, and cultured in the same conditions, so that the different topographies and shear adhesion forces could prove that the TRAIL did work on the cells.

4.2.1.2 Modeling of the mechanical properties measurement of cells

Through the analysis of mechanical properties of cells, Young's modulus is one of the most important parameters of the mechanical properties to evaluate the cell physiological state. It is originated from the applications that the ability of resisting deformation of the cellular surface can be described by the viscoelastic responses[103]. Hence, based on the contact surface morphology, many different mechanical models have been established by the researchers to calculate Young's modulus under different indentation depths. Two of major mechanical models were used to evaluate the mechanical behaviors of living cells including the sphere mechanical model and the pyramid mechanical model, and the force acting on the cellular surface can be expressed as[103]

$$F_{sphere} = \frac{1.4906 \cdot E \tan \theta}{2(1-\upsilon^2)} \delta^{1.5} \qquad (4.3)$$

$$F_{pyramid} = \frac{3ER^{0.5}}{2(1-\upsilon^2)} \delta^2 \qquad (4.4)$$

where E is the Young's modulus of living cells, δ is the indentation depth, R is the radius of curvature of the tip, θ is the opening angle of the tip, and v is the Poisson's ratio. The acting force on the cellular surface can be calculated based on different indentation depths due to the different shapes of the tip. In the experiment, the tip is pyramid and the top of tip is sphere. Hence, two of the mechanical models have been combined to evaluate the mechanical behaviors of living cells in our experiments, and the force can be expressed as[104]

$$F_e = \begin{cases} \dfrac{1.4906 \cdot E \tan \theta}{2(1-\upsilon^2)} \delta^{1.5}, & \delta \leq d \\[4mm] \dfrac{3ER^{0.5}}{2(1-\upsilon^2)} (\delta - d)^2, & \delta > d \end{cases} \qquad (4.5)$$

where d is the indentation depth changes in the experiment. the variation trend at the 99nm in the probe of the ContGB-G type made by Bruker corporation, with the spring constant of 0.2N/m, length of 450μm and width of 50μm, is used as the measurement tool[104].

4.2.2 Experiments and Results

After the cell indentation was modeled, the Young's modulus of the cell was calculated based on the geometrical shape of probe tip in different indentation depths. The samples in experiments were SW480 human colon cancer cells grown on an unsupported cover-slip in culture. Initially, an inverted microscope was used to observe cancer cells. Then, the probe was moved to the selected location showing only the non-overlapped cells in the scanning area, avoiding any damage of single cells in the manipulation. In the cell indentation experiments, the cell was manipulated by the nano displacement platform and the AFM probe after the cell imaging, and an indentation force-displacement curve was obtained with a good expression of the whole indentation process. As shown in Figure 4.4, it is the schematic of the force-displacement curve in one indentation. The vertical axis of the curve shows the interaction force between the probe and the sample as the probe penetrates into the surface of cell until it is pulled away from the surface, and the surface of cell is smooth with minimal deformation.
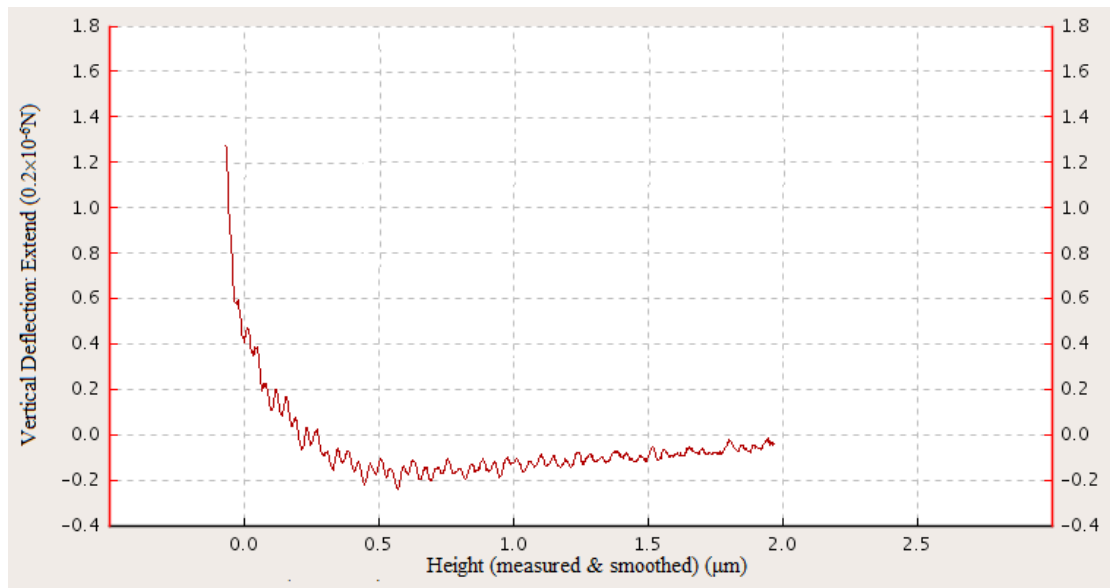
Figure 4.4 Force-displacement curve in one indentation.
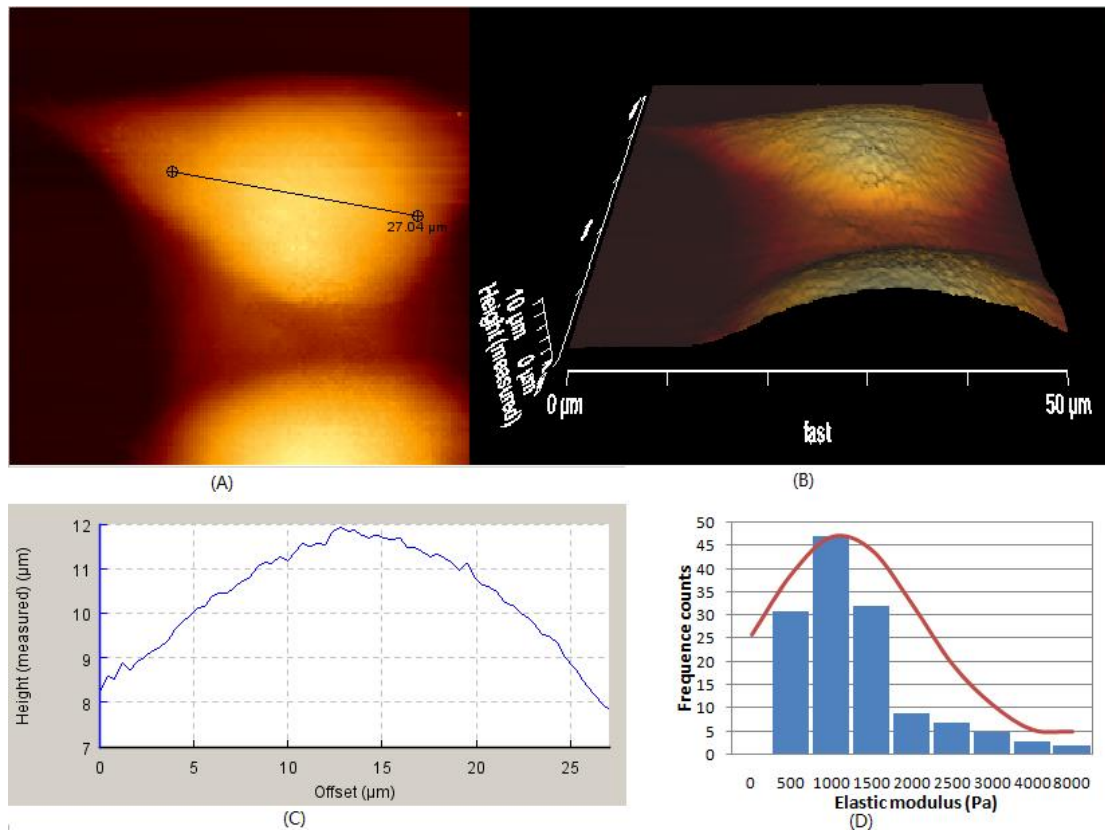
Figure 4.5 Nano scale topography of the SW480 colon cancer cells obtained by AFM in culture. (A) Topography image of two SW480 cells, obtained in the contact mode, and the area of cell is about 416.25μm². (B) 3D topography image of the cells. (C) Cross section plot of a single cell in the upper part of figure. It is oval in shape, which is 27.04μm long, 19.60μm wide and 3.2μm high. (D) Histograms showing the Young's modulus-frequency count distribution of SW480 cells from 136 force curves, and the mean standard deviation of the elastic modulus is 352.08±241.81Pa..
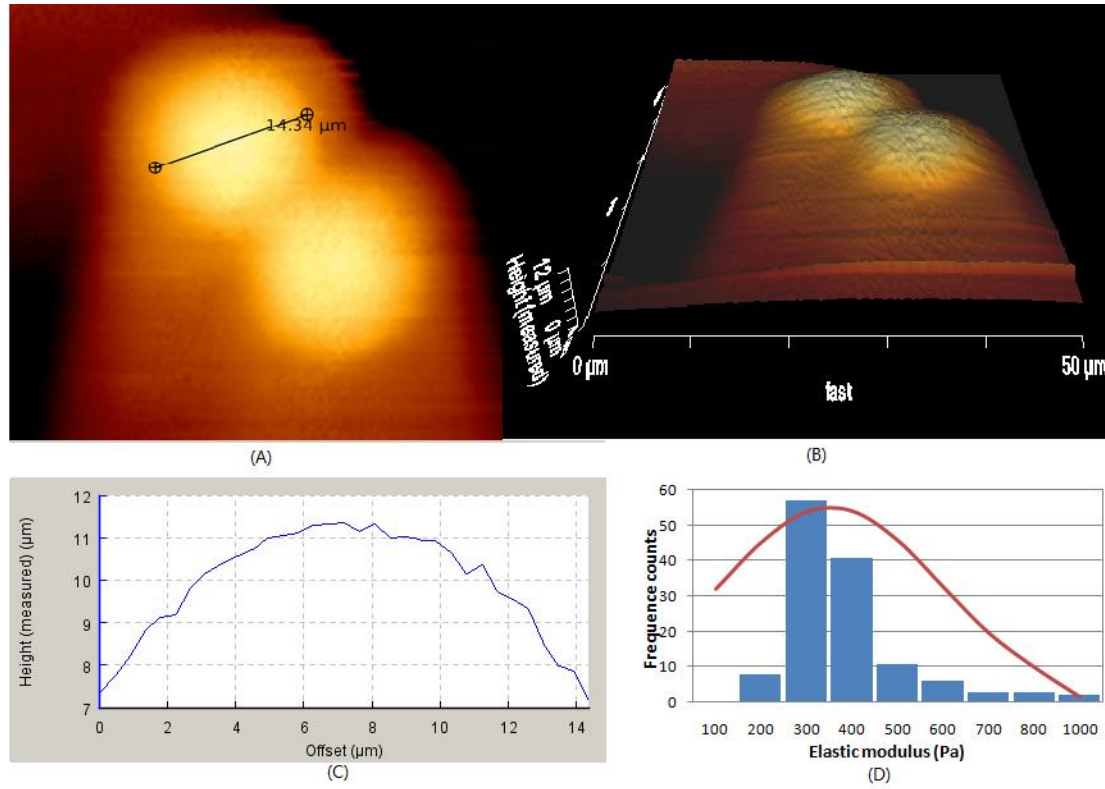
Figure 4.6 Nano scale topography of a SW480 colon cancer cell with TRAIL obtained by AFM in culture. (A) Topography image of a single SW480 cell with TRAIL, obtained in the contact mode, and the area of cell is about $254.47\mu m^2$. (B) 3D topography image of the cell. (C) Cross section plot of the single cell. The cell in the upper part of figure is round with the radius of $14.34\mu m$ and the height of $4.3\mu m$. (D) Histograms showing the Young's modulus-frequency count distributions of SW480 cells with TRAIL from 131 force curves, and the mean standard deviation of the elastic modulus is $1121.59 \pm 943.54Pa$.

In the experiments, the cell samples with 30%-40% of cell confluence were collected for the topographical measurement of cells. The scanning rate was 0.4Hz and the image size was 512×512 pixels by the contact mode. Figures 4.5 and 4.6 show the topographical images of SW480 cells without and with TRAIL (Figures 4.5(A) and 4.6(A)) and their cross section plots. The experiments reveal a phenomenon in the measured topography of two cells. These findings indicate that the cells treated with TRAIL show the round shapes, and the apoptosis of SW480 is

appeared. Moreover, there might be some proteinaceous adhesive secretions around the cell surface and interfered with the cell imaging. Hence, the edge fuzzy phenomenon exists in the cell scanning. The cross sections of the cells are shown in Figures 4.5(C) and 4.6(C), and the highest point of the cell can be observed. An appropriate indentation location toward the highest point was selected in this study. The histograms of Young's modulus-frequency count distributions are shown in Figures 4.5(D) and 4.6(D). The average Young's modulus of SW480 colon cancer cells is 1203 ± 253Pa at the indentation depth of 110nm, and the Young's modulus of SW480 colon cancer cells with TRAIL is 364 ± 79Pa. It clearly shows that the viability of SW480 cells with TRAIL is much smaller than that of the cells without TRAIL. Hence, from the results shown, a significant change of the Young's modulus of the cell is found, which is associated with the TRAIL action. The underlying reason for the decrease of Young's modulus of the cell can be attributed to the disruption of the viability of cells. For evaluating the TRAIL-induced apoptosis precisely, a novel sensitive and fast cellular shear adhesion force measurement method based on the AFM was presented in Section 4.3.

4.3 Cellular Shear Adhesion Force Measurement Based on Liquid-AFM

Cell adhesion refers to the cell-cell and cell-matrix interactions, which is not only a main approach for the communication between cells but also an important biological phenomenon for the maintenance of morphology and functions in multi-cellular organisms[105][106]. For the research of artificial organs, the cell-cell adhesion and cell-substrate adhesion are closely related to the biological compatibility of artificial implants. Meanwhile, the cell-substrate adhesion is the key factor critical for the success of the implantation operation of artificial organs. Thus, great attention has been paid to the cell-cell adhesion, cell-matrix adhesion, related cell morphology structure, function, deformation ability and adhesion of cells[107][108][109].

To understand the mechanical properties of single cells as well as their variations, it is necessary to establish a proper method for the measurement of cell-cell adhesion or cell-matrix adhesion in

vivo and overcome the limitations of current methods[110]. There were several methods developed for the measurement of cell adhesion, including the mechanical method, isotope, PPFC (Parallel-Plate Flow Chamber), cell isolation, micro fluidic method, micropipette, optical tweezers and atomic force microscope[111][112][113]. The mechanical method evaluated the cell adhesion through calculating the percentage of tumor cells[114]. Isotope, PPFC and cell isolation methods detected cells in groups[115]. Currently, the micropipette and micro fluidic methods are the two significant approaches to determine adhesion forces of cells[116]. However, as a result of the complicated deformation features of cells, it is difficult to obtain the precise value of an adhesion force. Optical tweezers could manipulate cells accurately on the pN-scale. However, during the manipulation, cells could be injured due to the high-intensity laser beam[117].

The AFM is used as a tool for the imaging of cells on the nano scale[118]. It can implement the mechanical detection of a single cell with high precision based on the optical lever, and obtain the cell morphology in real-time. The probe cantilever can detect the morphology character on the cell surface as a terminal executor. Meanwhile, as a manipulator, it can also acquire various mechanical properties on the cell surface. Applying lateral forces to characterize cell detachment forces by AFM has been investigated in numerous studies. They used AFM cantilevers to detach cells and characterize detachment forces[119][120][121][122]. However, current studies for the detection of the cell adhesion force with an AFM are unable to measure the shearing adhesion force of living cells and obtain the morphology character at the same time. Moreover, the shearing adhesion force was usually calculated by the deflection of cantilever with one direction. There might be some extent errors in the lateral direction and without including the effects of pushing speeds. Thus, in this work, a simple and sensitive method to measure the cellular shear adhesion force by AFM is presented. The AFM was used both as a tool for the imaging of cells on the nano scale and as a force sensor for the measurement of the adhesion force between the colon cancer cell and the substrate. The method displaced the cell using the AFM cantilever tip along the sample surface and measured the resulting deflections with the lateral signal and vertical signal of

the cantilever. An optical feedback system based on a CCD (Charge-Coupled Device) camera was used together with an AFM to manipulate cells in real-time, so that it was able to perform the morphology measurement of some specific targeted cells. Moreover, different pushing speeds of probe were firstly used in experiments to study their influences. The experimental results have shown that the method can provide an effective way for the measurement of the horizontal shearing adhesion force between the cell and substrate, and for the exploration of adhesion forces of cancer cells using both the AFM imaging and manipulation systems. The method is described in detail in the following sections.

4.3.1 Materials and Methods

4.3.1.1 Force modeling of the cantilever

During the operation to manipulate cells, the nano scale tip of AFM will suffer from the various forces such as the Van der Waals force, electrostatic force, capillary force, friction force, surface tension and Coulomb force. All of the forces can make the twist and bend deformations of the cantilever. A model for the deformation of the cantilever in three dimensions has been established for the forces along with the three orthogonal coordinate axes (F_x, F_y and F_z), as shown in Figure 4.7.
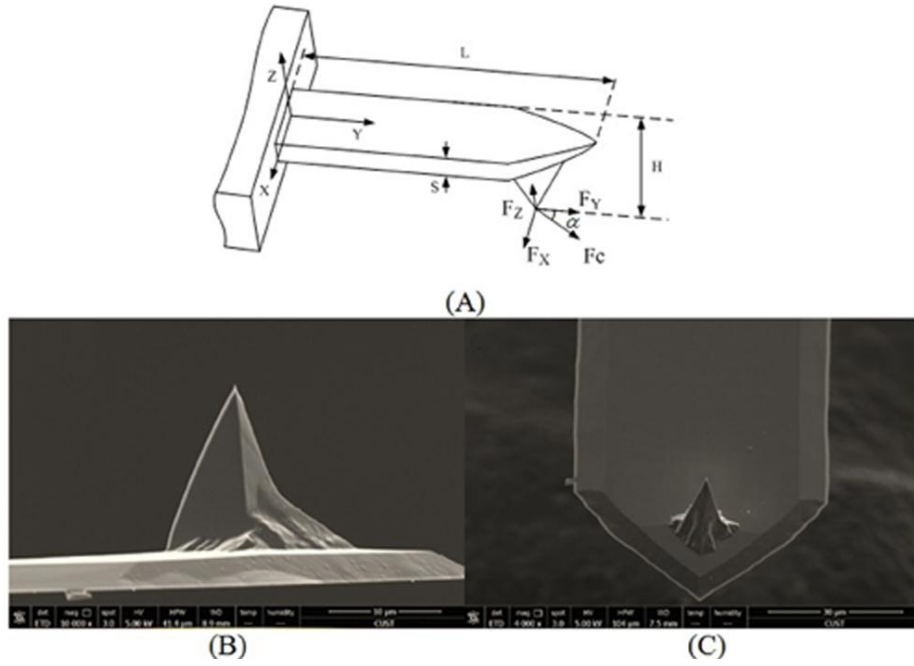
Figure 4.7 Modeling of a cantilever-tip in three dimensions. (A) AFM cantilever deformation model in three dimensions. (B) SEM side view of the tip of the AFM cantilever used for the single cellular shear adhesion force measurement. (C) SEM front view of the AFM cantilever.

The cell manipulation task is implemented by the developed AFM system, and the cellular shear adhesion force acts on the probe tip and makes it bending due to the adhesion force between the cell and substrate. When the torsional force of the cantilever is greater than the cellular shear adhesion force, the cell will be separated from the substrate. Thus, the cellular shear adhesion force can be obtained by the cantilever deflection.

In the components of the three forces along with the three orthogonal coordinate axes, the force F_x will produce the twist of the cantilever around its central axis, and it can be expressed as[123]

$$F_x(H + \frac{S}{2}) = k_t\theta \qquad (4.6)$$

where H is the height of probe, S is the thickness of cantilever, k_t is the torsion spring constant of cantilever, and θ is the twist angle from the rest position. The torsion strength of cantilever is[124]

$$k_t = G\beta wS^3 / L \tag{4.7}$$

where G is the shearing elasticity modulus of the cantilever material, w is the width of cantilever, L is the length of cantilever, and β is the constant calculated by S/w. Here, L=450μm, H=18μm and k_t=1.71×10^{-7}N.m/rad can be obtained.
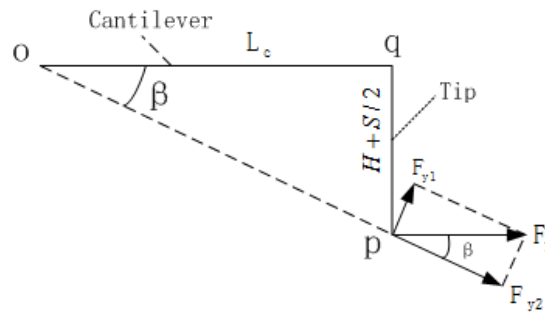
Figure 4.8 Model of F_y acting on the cantilever.

As shown in Figure 4.8, the torque is generated on the cantilever by F_{y1} which is the component of the force F_y and perpendicular to the OP. According to the triangle OPQ, the following equations are obtained:

$$\sin\beta = \frac{(H + S/2)}{\sqrt{L^2 + (H + S/2)^2}} \tag{4.8}$$

$$op = \sqrt{L^2 + (H + S/2)^2} \tag{4.9}$$

Hence, the torque T can be calculated as

$$T = op \times F_{y1} = F_y \times \sin\beta \times op = F_y \times \frac{(H + S/2)}{\sqrt{L^2 + (H + S/2)^2}} \times \sqrt{L^2 + (H + S/2)^2} = F_y(H + S/2) \tag{4.10}$$

where β is the torque angle of cantilever in the vertical direction. Moreover, there is no torque generated by F_{y2} which is along with the other component of force F_y. When the probe acts on the cell, the force F_y in the Y axis direction will make the cantilever bend in the vertical plane, and it can be calculated by

$$F_z L + F_y (H + S/2) = k\delta L \tag{4.11}$$

where L is the length of cantilever, k is the force constant of cantilever, and δ is the vertical deflection of cantilever induced by the force F_y.

When the probe acts on the cell, the cantilever will be deflected and detected by the PSD through the optical lever collecting the reflected laser signal. The PSD will output two signals. One is the up-down signal in the vertical direction representing the deflection of cantilever in the Z direction, and the other is the left-right signal in the horizontal direction representing the twisting deflection of cantilever. Then the offsets can be expressed as

$$\begin{cases} \delta = k_v S_v \\ \theta = k_h S_h \end{cases} \tag{4.12}$$

where k_v and k_h are the deflection and torsional sensitivities of the optical lever detection system, S_v is the vertical signal output, and S_h is the horizontal signal output of PSD. A large displacement of the light spot introduced by the optical lever can be detected using the PSD. Since the light intensity distributions are different, the deflections of cantilever can be measured through the differential signals from the up-down and left-right outputs.

When the cellular shear adhesion force reacts on the probe tip, the deflection of cantilever can be measured by PSD. Assume that the sample is pushed away from the substrate by cantilever with the angle a, the relationship between F_x and F_y can be expressed as

$$F_x = F_y \tan \alpha \qquad (4.13)$$

With the modeling of the manipulation of cells under pushing, the 3D force can be obtained. Hence, the resultant force of cantilever F can be calculated by

$$F = \sqrt{F_x^2 + F_y^2 + F_z^2} \qquad (4.14)$$

In order to realize the accuracy of manipulation, the relation constants in each equation need to be obtained and calibrated. Firstly, a standard grating is used to calibrate k_v, and the relationship between the PSD vertical signal and the vertical deflection of cantilever, as shown in Figure 4.9. Moreover, a hard probe with the spring constant of 30N/m and the length of 129μm was used in this experiment to avoid the influence of ambient noise. According to Eq. (4.11), the parameter k_v can be calculated based on the linearly regressed fitting, and here k_v=72.6nm/V.
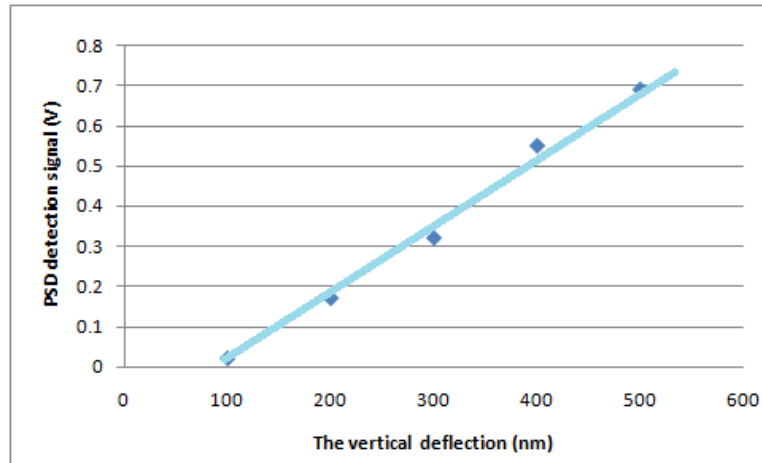
Figure 4.9 The relationship of the cantilever vertical deflection and the PSD detection signal.

Secondly, when the vertical deflection angle equals to the twisting angle, the PSD signal outputs should be equal. Moreover, the two angles are so small that θ is approximately equal to $\tan\theta$. Hence, the relationship between k_v and k_h can be expressed as

112

$$\frac{\delta_z}{l} = \frac{k_v S_v}{l} = \frac{k_h}{S_h} \qquad (4.15)$$

where l is the cantilever length used in the calibration experiment. For the PSD with the same sensitivity in both deflections, it can be calculated as $k_h = k_v / l$. Hence, $k_h = 0.56 \times 10^{-4}$ rad/V.

According to the thermal noise measurement method, the thermal energy calculated from the absolute temperature is equal to the energy measured from the oscillation of the cantilever. The frequency measured in the experiment is used to calculate the spring constant as

$$k = \tau f^3 \qquad (4.16)$$

where k is the spring constant, τ is the coefficient based on the tip type, and f is the measured resonant frequency. Here, $k = 0.6$ N/m. According to Eq. (4.14), the force value can be calculated, and the cellular shear adhesion force between the cell and substrate can also be obtained by the force modeling of the cell described in the following.

4.3.1.2 Modeling of the force on a cell

After the modeling of the force on the cantilever, the force on the cell can also be modeled. A cell can be seen as a rheological body model covered with soft membranes. When a cell is manipulated, the probe can apply a horizontal push force to the cell. According to the condition of static equilibrium, the cellular shear adhesion force can be expressed as[125]

$$F_c = \int_{A_c} \tau_c dA_c \qquad (4.17)$$

where F_C is the cellular shear adhesion force, A_c is the adhesion area between the cell and substrate, and τ_c is the shear adhesive stress. The adhesion force between the substrate and sample in unit area can be calculated by Eq. (4.17).
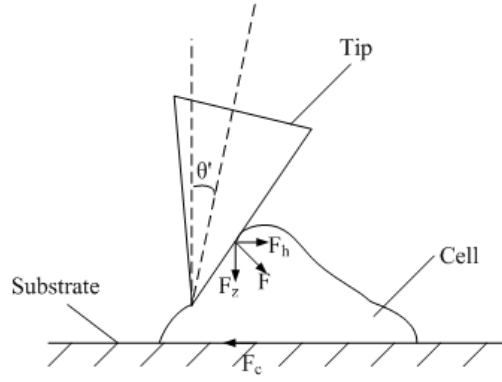
Figure 4.10 Model of probe-cell interaction.

When the probe acts on the cell, it has a certain distance to the substrate. Thus, the deformation of the cell mainly occurs in the upper domain of its surface. Considering the stress relaxation phenomenon of the cell, the cellular shear adhesion force can be approximately equal to the horizontal component of the cantilever twist force, and the force is applied to the cell, as shown in Figure 4.10. The relation between the cellular shear adhesion force and the horizontal component of resultant force of cantilever can be expressed as

$$F_c = F_h - F_z \cdot \eta \tag{4.18}$$

where $F_h = \sqrt{F_x^2 + F_y^2}$ is the horizontal component of resultant force of cantilever. η is the friction coefficient between the cell and the non-coated substrate. It is calculated by each of the two measurements of cellular shear adhesion force due to the correlation of the area of cells and F_c, here $\eta \approx 0.9$ [125].

As the pushing force acts only on the cell parts close to the probe and the probe displacement is zero in the Y direction, the pushing force is considered too far to affect the measurement of cellular shear adhesion forces. In this case, the friction between the probe and the cell is neglected.

If the cell is further pushed away from the substrate surface, the adhesion force will cause the

cantilever twist in the opposite direction until it is completely detached from the surface, and there are no additional forces acting on the *Z* axis since the probe is non-contact with the substrate during the manipulation. Hence, according to the superposition principle of forces, when the horizontal component of the cantilever twist force equals to the cellular shear adhesion force, there is a balance between the forces on the cell-probe.

4.3.2 Experiments and Results

4.3.2.1 Cell manipulation with different working speeds

In the cell manipulation, the probe was set to a distance of about 1μm from the substrate. According to the Saint-Venant's principle[126], the horizontal component of the cantilever twist force was approximately equal to the cellular shear adhesion force when there was a distance between the manipulating position and the substrate. The image of cell populations captured by CCD camera is shown in Figure 4.11.

(A)   (B)
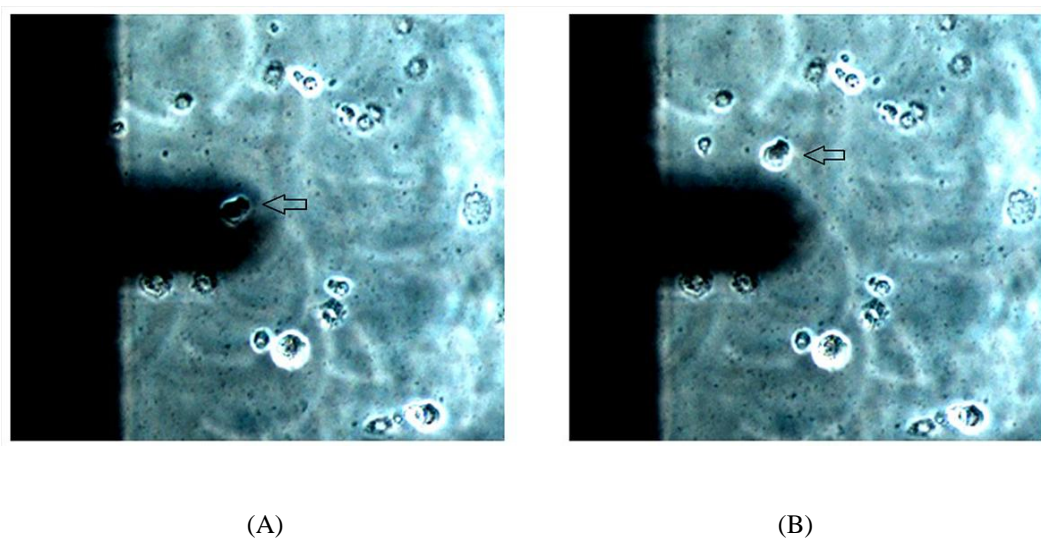
Figure 4.11 The image of cell populations captured by CCD. (A) CCD image of cell populations before manipulation. The AFM tip was moved to the target single cell. (B) CCD image of the cell population after manipulation.

The cells under the probe were used for scanning and manipulation by AFM, and those cells were independently grown on the unsupported cover-slip and easily manipulated. After the manipulation, the cell was separated from the substrate and floated in the culture indicated by the arrow, as shown in Figure 4.11(B). Furthermore, the maxima of probe deflections both in the up-down and left-right directions were selected and calculated by the manipulated model as established above. In this work, the probe pushed the different surfaces along the highest cross section with the PZT from the right to the left direction at the speeds of 15μm/s, 20μm/s and 30μm/s, respectively. The cantilever was deformed in the vertical direction and the torque direction due to the effects of cellular shear adhesion force and the angle α between the probe lateral direction and the manipulating direction. The up-down and left-right signals detected by PSD are shown in Figure 4.12, and the cellular shear adhesion force can be calculated by Eq. (4.18).
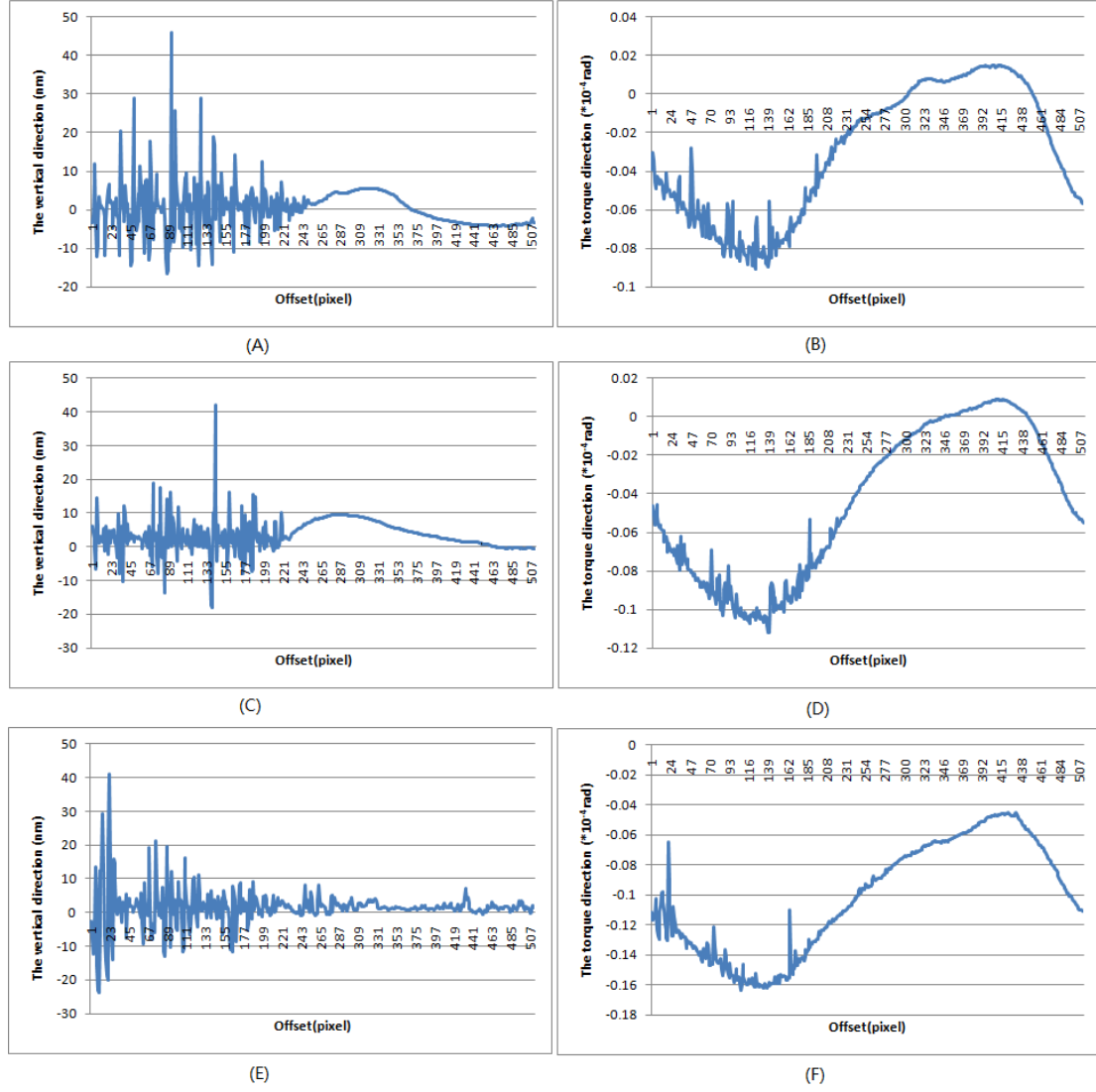
Figure 4.12 Experimental results. (A) The left-right signal detected by PSD when the probe speed is 15μm/s. (B) The up-down signal detected by PSD when the probe speed is 15μm/s. (C) The left-right signal detected by PSD when the probe speed is 20μm/s. (D) The up-down signal detected by PSD when the probe speed is 20μm/s. (E) The left-right signal detected by PSD when the probe speed is 30μm/s. (F) The up-down signal detected by PSD when the probe speed is 30μm/s.

By comparison with these measurements, it clearly indicates that the faster the probe manipulates the cell, the fewer the outside influence on the results. The impact of cell adhesion between the

117

cell and probe can be reduced by the increase of pushing speed. However, the faster speed might cause the oscillation during the manipulation, and due to the viscosity of culture, the horizontal component of the twisted direction will generate a certain deflection in the initial state which will affect the measurement of the lateral force. Thus, a suitable manipulation speed is more important to reduce the extra effect without any distortion in the experiment.

4.3.2.2 Cell manipulation in different locations

According to the highly precise imaging for the cell, various locations of the cell can be manipulated on the nano scale. Moreover, the trisection locations in the middle part and the both sides of different similar cells were manipulated respectively at the speeds of 20μm/s, as shown in Figure 4.13. Among them, the cellular adhesion force measurements in the both sides of the cell were implemented on the same cell. It can be seen that the maximum deflection of the probe manipulated on the middle part is far greater than that of the other two sides. Since the cell was separated from the substrate and floated in the culture, the measurement in the middle side must reflect the holistic shear adhesion force of the single cell. Furthermore, the cell manipulation in both sides of cells was not completely the same in the measurements. After the manipulations in both sides, the cell was not separated from the substrate due to the effect on the major part of the cell, then the force curve of the two output signals showed the difference with the manipulation in the middle part. Moreover, the measurement of the cell adhesion in the upper portion of the cell is twice as much as the measurement in the lower portion. It may reveal that the cancer cells have the metastasis tendency after cultured for 16 to 20 hours. The cell adhesion is the most important factor for the research of the cell metastasis. On the basis of mechanic research of physical translocation with a novel perspective on the metastatic process, it is important for preventing metastasis in the patients diagnosed with early cancer lesions[127].
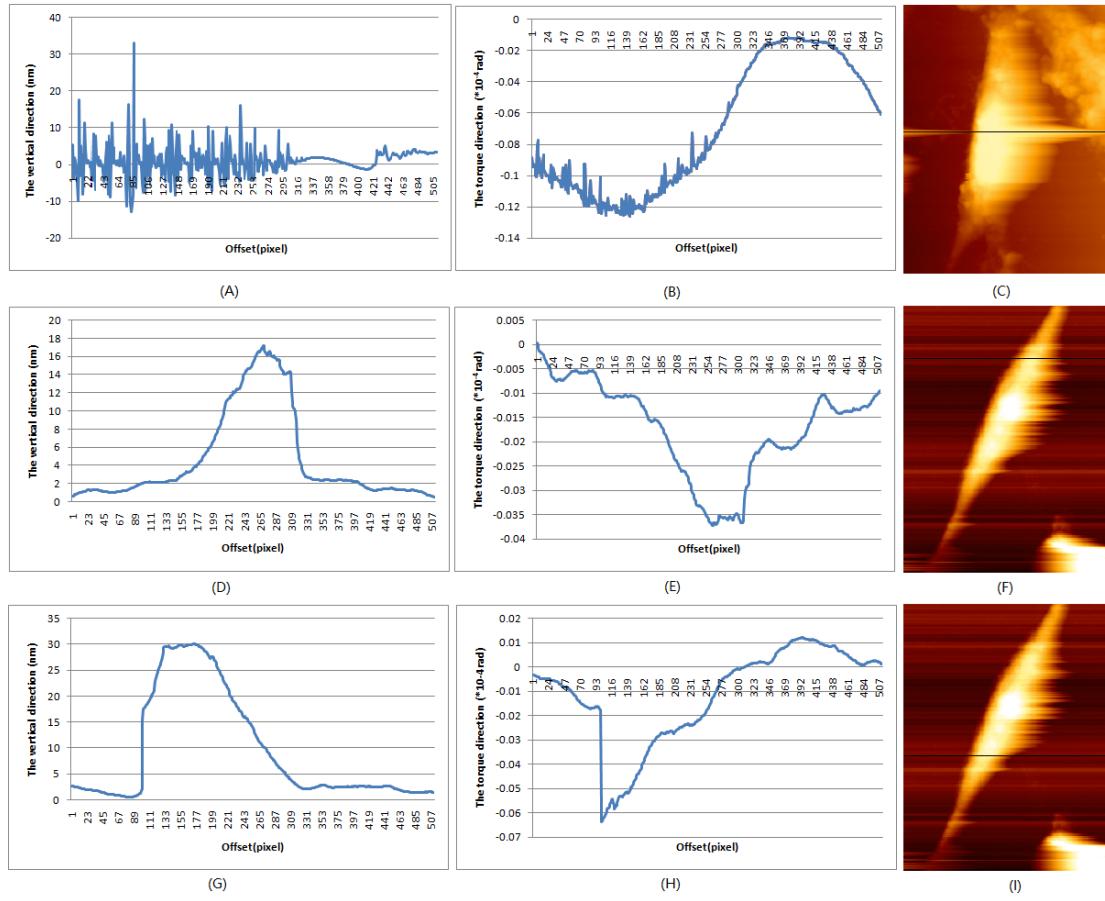
Figure 4.13 Experimental results. (A), (B) and (C) are the left-right signals and up-down signals detected by PSD when the cell was manipulated in the middle part, and the schematic diagram of the manipulation, respectively. (D), (E) and (F) are the left-right signals and up-down signals detected by PSD when the cell was manipulated in a relatively slender part on one side, and the schematic diagram of the manipulation, respectively. (G), (H) and (I) are the left-right signals and up-down signals detected by PSD when the cell was manipulated in a relatively large part on the other side, and the schematic diagram of the manipulation, respectively.

4.3.2.3 Cell manipulation for different types of cells

Cell manipulation can study the metastasis of cancer cells, and identify the cell viability. The experimental conditions were kept the same with the cell culture during the measurement. Figure

4.14(A) shows the cellular shear adhesion force measurements of twenty SW480 cells. The cell adhesion can be quantitatively expressed by the adhesion force of the unit area. Thus, combined with the morphology character of cells on the nano scale, the cellular shear adhesion force of the unit area can be calculated, and the adhesion changes on different surfaces can be obtained. Figure 4.14(B) shows the corresponding measurements of each cell adhesion force per unit area. It clearly shows that the adhesion forces of unit area are performed in the same level when the cells are cultured in the same batch.

(A)   (B)
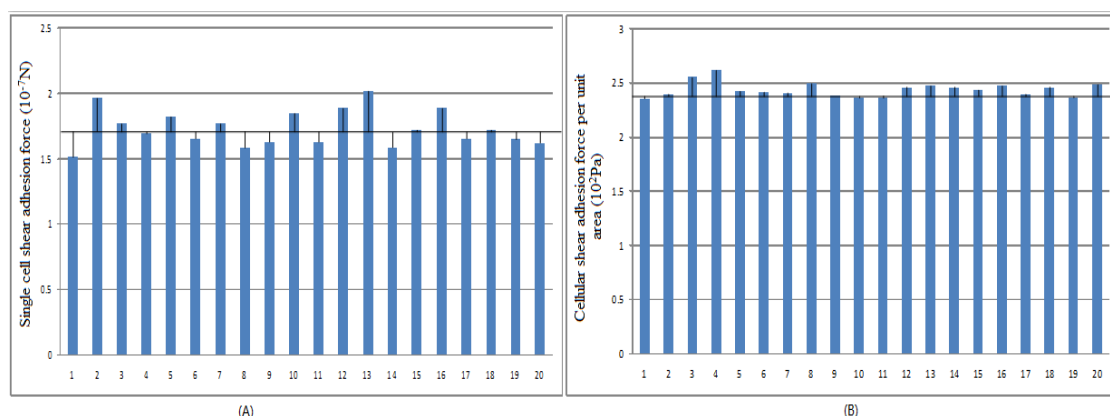
Figure 4.14 Cellular shear adhesion distributions. (A) The cell adhesion force measurements of twenty cells. (B) The corresponding measurements of each cell adhesion force per unit area.

The experimental environment was kept to the same conditions during the culture and measurements. Figure 7 shows the average shear adhesion force measurements with three types of samples on each substrate from 20 force curves. The shear adhesion forces of cancer cells were $1.7\pm0.3\times10^{-7}$N on the non-coated cover slip. On the other hand, the shear adhesion forces of the same type of cancer cells with the TRAIL of 300ng/ml were $0.71\pm0.2\times10^{-7}$N on the same cover slip, and the cancer cells with the TRAIL of 200ng/ml were $0.87\pm0.2\times10^{-7}$N. The results show that the shear adhesion force is decreased when the cells are cultured with TRAIL, which agrees well with the previous research. The proposed method of cellular shear adhesion force measurement is

easy to perform and quantitatively identify the viability of single cells. Moreover, combining with the high resolution images of cells before and after cantilever manipulations, the cells of interest can be presented with more information in single cell analysis.
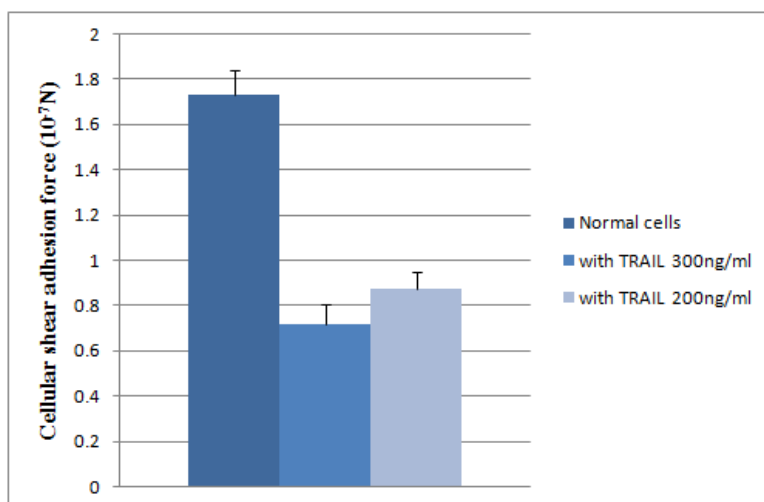
Figure 4.15 Average adhesion force measurement with the deviation of two kinds of samples on each substrate.

Cell adhesion is a biological phenomenon to maintain the morphology structure and functions of cells. It is mainly mediated by the adhesion molecules on the cell surface involved in signal transduction and recognition of normal cells to maintain the integrity of tissues. In cancer cells, the adhesion force is weakened, and changes in adhesion between the cancer cell and the substrate are important factors for the invasion and metastasis of cancer cells[128]. The other methods for measuring the shear adhesion force deformed cells in AFM only using the back of cantilevers to detach cells. Because of the heterogeneous density inside of the biological cell, samples were occasionally not detached by the probe in the pushing direction, which ignored the other

directional components of the deformation force and the impact of pushing force. Moreover, the visual feedback with an optical microscope or an environmental scanning electron microscope (ESEM) could not present an accurate position of the cell and obtain the morphology character at the same time. With this method, a model for the deformation of the cantilever in three dimensions was established for the forces along with the three orthogonal coordinate axes, and the probe with the elastic deformation property was placed horizontally adjacent to the cell. Based on the superposition principle and the transferability of the force, cells and probes were subjected to a critical status for the detachment through a horizontal force introduced by PZT. When the probe was twisted by the force for the detachment between the cell and the substrate, the maximum horizontal component of the twisted force was used to calculate the cellular shear adhesion force. In the measurement, the accurate manipulation on the nano-scale can be performed based on the cell morphology, especially for the different locations of the cell manipulation which is potentially beneficial to the mechanic research of physical translocation with a novel perspective on the metastatic process. Thus, the cellular shear adhesion force per unit area can be obtained and analyzed, combined with the adhesion changes on different surfaces. It reflects the physiological state of cells more accurately in molecular level.

Furthermore, in this work, the experimental results show that the cellular shear adhesion force will be reduced when the cells are cultured with the immune expression of TRAIL, as shown in Figure 4.15. TRAIL expressed by in vitro can protect from tumor metastasis and suppress the growth of cancer cells. In addition, the cell indentation research also shows that the elastic modulus of

SW480 cells without TRAIL is much smaller than that of the cells with TRAIL, and it reflects that the viability of SW480 cells with TRAIL will be reduced due to the declined shear adhesion force and the gradually-hardened cell surface. In the experiment, two different concentrations of TRAIL have been used to study their impacts on the shear adhesion force of cells. In this method, the variation tendency of shear adhesion forces and the morphology changes can be performed simultaneously on the nano-scale. Before the measurement of the shear adhesion force of the cancer cell, the cell was adhered to the substrate for more than 16 hours, so that the shear adhesion force between the cell and the substrate was almost unchanged, and the measurement deviation was minimized. With this method, the cellular shear adhesion force can be obtained.

4.4 Summary

There are recently a number of emerging methods for the characterization of living biological samples in vitro. The progress in the disease treatment and cancer cell study has been made. However, there is still lack of low-damage, efficient, straightforward methods for the biomechanical analysis of individual single cells. To solve those problems, the biological cell imaging in different liquids was studied to improve the image quality. Moreover, in this chapter, the AFM was used both as a tool for the imaging of cells on the nano scale and as a force sensor for the measurement of the adhesion force between the cell and the substrate and the mechanical properties of biological cells in culture. After the cell imaging, the measurement of cellular shear adhesion forces can be made based on the different positions of the cell on the nano scale. Moreover, different pushing speeds of probe and various locations of cells were used in experiments to study their influences. In this study, the measurement of the cell adhesion in the upper portion of the cell is different from that in the lower portion. It may reveal that the cancer

cells have the metastasis tendency after cultured for 16 to 20 hours, which is significant for preventing metastasis in the patients diagnosed with early cancer lesions. Furthermore, the cellular shear adhesion forces of two types of living cancer cells were obtained based on the measurements of AFM cantilever deflections in the torsional and vertical directions. The results demonstrate that the adhesion force of cancer cells is twice as much as the same type of cancer cells with TRAIL. The method can also provide a way for the measurement of the cellular shear adhesion force between the cell and the substrate, and for the simultaneous exploration of cells using the AFM imaging and manipulation.

Although AFM has become the versatile tool according to the functions for biological cell handling, imaging and force feedback, the trapping and manipulation of cells with less damage are still not achieved by the single instrument. Hence, the integrated manipulation for biological cells based on liquid-AFM and optical tweezers is proposed. For effective manipulation and better observation of biological cells, the key technical properties and the application extensions of optical tweezers for biological cells are studied in the followed chapters.

Chapter 5

Force Characterization of Biological Cells Based on Single Optical Tweezers

An optical tweezers system is the instrument that can trap and move the micro/nano objects without physical contact based on the transfer of photon momentum. The rapid and precise manipulation of living cells can benefit the cytology, such as the cell microsurgery, the cell-cell interactions, and especially the isolation and collection of particular cells[129][130]. For the integration of liquid-AFM and optical tweezers, according to the basic components of the traditional optical tweezers, a single optical tweezers system was developed to manipulate the biological cells by the nano displacement platform in the liquid AFM system and the light beam phase shift. Moreover, the dynamics analysis of the trapped cell is used to determine the movement velocity of the cell which is the most important parameter to test the physical properties of cells. However, little research has been reported on the synergy of dynamic analysis for the prediction and interpretation of the movement velocity of the cell with the analysis in the Z direction. Hence, a new experimental method integrated with the positioning in the Z direction was used to improve the fluid force method for the calibration and characterize the mechanical forces exerted on the optical traps and the living cells.

5.1 Development of Single Optical Tweezers

Optical tweezers can be considered as the optical trap, which is formed by a laser beam, after the expanding and collimation, entering into the objective lens with a high magnification and high

numerical aperture. Meanwhile, optical tweezers also needs to use the optical microscope to observe the dynamic changing process of the particles. For instance, using the optical microscope can obtain the capture, fixation and movement of the biological cells when they are manipulated by the optical tweezers. The core of optical tweezers generally consists of five parts, including laser, optical path adjusting system, operating system and real-time visual feedback system, as shown in Figure 5.1.
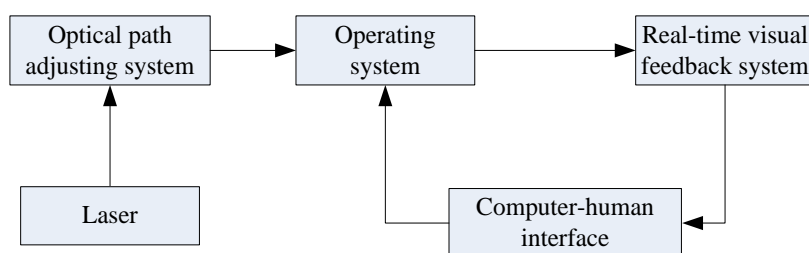
Figure 5.1 Block diagram of the traditional optical tweezers.

According to the principle of optical tweezers, the optical trap can be formed by the focusing system to trap the cell and other particles. The laser passes through an optical path adjusting system, and it is reflected by a mirror which can totally reflect the laser with 532nm wavelength. Then, the objective lens is used to focus the laser in the sample plane, thus to capture and move the biological cell. Among them, the nano displacement platform is implemented to control the movement of platform and an eyepiece and CMOS camera are used to integrate the objective lens into a real-time visual feedback system, as shown in Figure 5.2
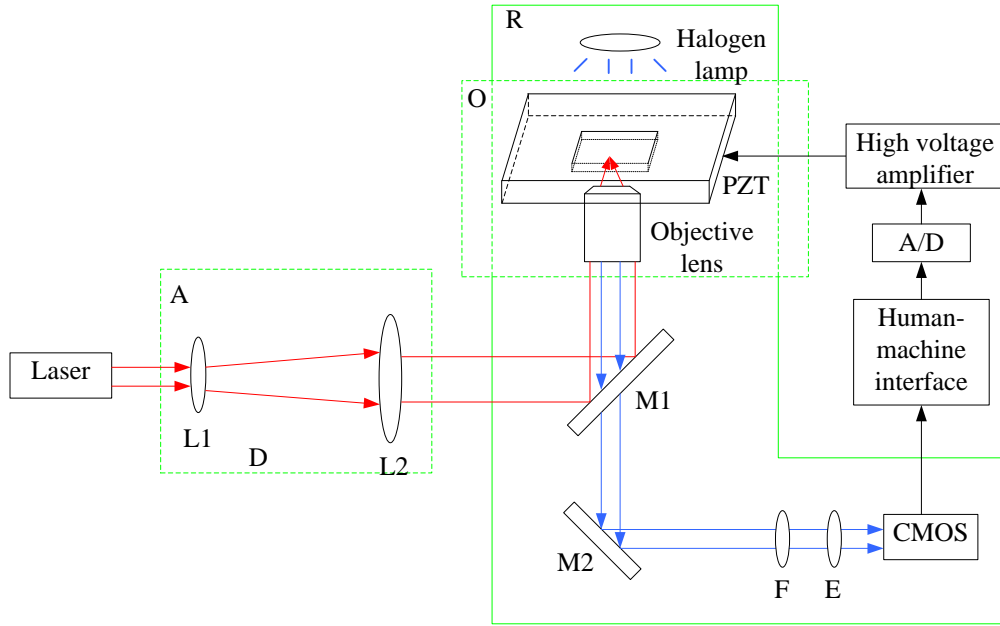
Figure 5.2 Configuration of optical tweezers. A: optical path adjusting system; O: operating system; R: real-time visual feedback system; L: lens; M: mirrors; F: optical filter; E: eyepiece.

5.1.1 Light Source of Optical Tweezers

After the focusing of objective lens, laser can form an optical trap near the focus. In order to ensure the accurate and nondestructive manipulation of the particle, it is required to select the laser that has an appropriate wavelength and power parameters with stable and reliable performance as the light source of optical tweezers. At present, the high-power continuous laser with the single mode is mostly used in relevant applications of optical tweezers.

Figure 5.3 Photograph of laser with the 532nm wavelength.

In the system, the laser can output a Gaussian beam with linear polarization. The beam has a 1mm waist diameter, less than 1mrad divergence angle, and the adjustable power of 0-1086mW, as shown in Figure 5.3. Light with the short wavelength has a small diameter of light spot after passing through the objective lens, which is helpful for capturing the particle. However, the shorter the wave length of laser, the larger the energy of single photon, which causes the adverse effects on the capture. Therefore, in the case of selecting the wavelength of laser, it is required to keep away from the light absorption bands of the cells, or they will be damaged. In the manipulation experiments of the cell by using optical tweezers, the laser with the wavelength of 533nm-1064nm was selected, which was the most suitable for the cell manipulation experiments.

In order to make the full use of the energy of laser on the exit pupil of objective lens, the expanding and collimation system is used to adjust the size of light spot and reduce the angle of divergence. In the design of optical tweezers, it is required to add a small hole at the back of laser so as to filter the stray light at the edge of laser to improve the quality of light spot and adjust the size of light spot coordinated with the beam expanders.

5.1.2 Optical Path Adjusting System

In order to improve the quality of light spot and generate a steeper light field gradient, the laser is required to implement expanding and collimation for the beam before the incidence to the objective lens and focusing of the beam, thus to compress the divergence angle of beam, reduce the waist radius, increase the gradient of light spot, and stably capture the cell. According to the demands of the optical path, the adjusting system includes the focusing lens, the optical filter and other optical elements to adjust the deflecting direction and the intensity of laser, as shown in Figure 5.4.
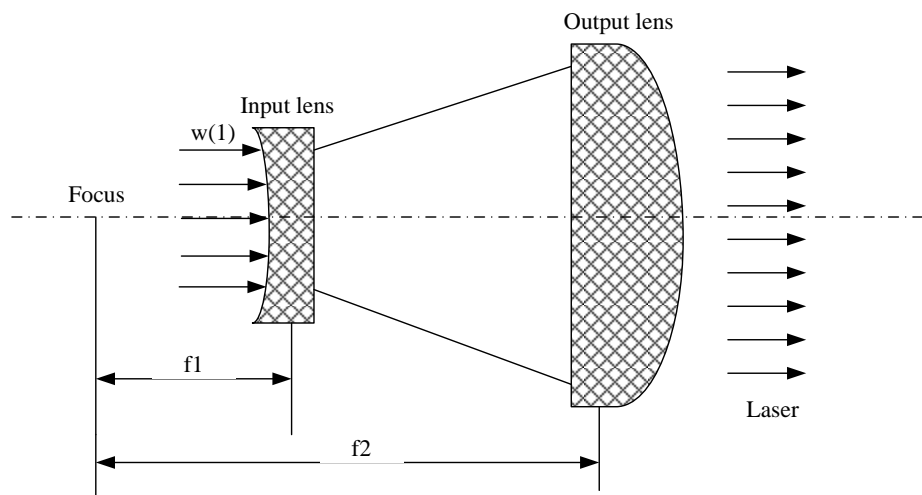
Figure 5.4 Overview of optical path adjusting system.

Although the divergence angle can make Gaussian beam focus better, we still need to take measures to further improve its calibration in the precision measurement. Thus, the Gaussian beam is aligned and expanded, and further the divergence angle is compressed and the spot size is expanded. Meanwhile, the alignment with the spatial filter can raise the spatial coherence, and make the light energy distribution more uniform. When the laser passes through an attenuator assembled with a half wave plate and polarizer, the energy of laser can be adjusted that the polarization state can also be detected. The Gaussian beam keeps on the same characteristic when

it goes through the lens, and satisfy the following relations[131]

$$\frac{1}{R^{'}} = \frac{1}{R} - \frac{1}{f^{'}}$$ (5.1)

$$\omega^{'} = \omega$$ (5.2)

where w is the waist radius of Gaussian beam, and f is the confocal parameter of Gaussian beam. With the short focal length lens, the Gaussian beam is focused, and got a tiny waist spot. After that, a long focal length lens is used to improve the direction of laser, and make it have a good alignment effect. The waist spot after the focusing just falls on the focal plane of long focal length lens system. The alignment rate can be expressed as[131]

$$M = \frac{\theta}{\theta^{'}} = M\sqrt{1 + \left(\frac{l\lambda}{\pi\omega_0^2}\right)^2}$$ (5.3)

where ω_0 is the waist radius of incidence laser, θ is the divergence angle, l is the distance between the lens and the waist radius of incidence laser. The new waist will fall in the focal plane of the output lens, which is longer than the input. M is the alignment magnification of telescope (geometry compression ratio). The confocal parameter after alignment can be expressed as[131]

$$d = M^2\pi\omega_{10}^2\frac{1}{\lambda}$$ (5.4)

so that the divergence angle of the output laser will reduce to *1/M*, and the confocal parameters is increased to *M²*.

5.1.3 Operating System of Optical Trap

The objective lens is the key part of the whole system, and the gradient force of optical trap is

formed by using it to focus the laser. With the action of gradient force, the particle will be restricted near the focus. Meanwhile, the objective lens is the most important component of optical tweezers both in the visual feedback and the device for the cell manipulation.

Through the expanding and collimation system, laser enters into the objective lens and focuses on the sample plane. Then the cell can be stably captured on the sample stage by the focused laser. Hence, the following issues need to be considered for the use of the objective lens:

1) Since the parameters of numerical aperture of the objective lens decide the maximum angle of laser focusing, the objective lens with a large numerical aperture is usually selected so as to obtain the required convergence angle. The objective lens selected for optical tweezers is usually the oil immersion objective lens, which needs to add a drop of oil between the front surface and slide when it is used, so as to improve the numerical aperture of objective lens by increasing the refractive index of medium between the slide and the objective lens.

2) The size of numerical aperture is in inverse proportion to the working distance. Thus, in consideration of convenient placing, operation and observation of the samples, the optical tweezers need to be designed as an inverted type, which has a similar imaging part with that of an inverted microscope.

As shown in Figure 5.5, it is the oil immersion objective lens which is used for this system. The mechanical tube length of objective lens is 160mm, which requires that the actual distance between the objective lens and eyepiece is also 160mm, thus to clearly observe the state of cells on the focal plane. The other parameter is required that the thickness of standard slide for the experiments needs to be 0.17mm. Before the experiments, add a drop of cedar oil on the front surface of objective lens, with a refractive index of 1.52, lower the object stage to make it fully contact with slide, and avoid the production of bubbles and the influences on experimental performances. Meanwhile, the objective lens is a part of microscope imaging system, as shown in

the dotted portion *R* in Figure 5.2.
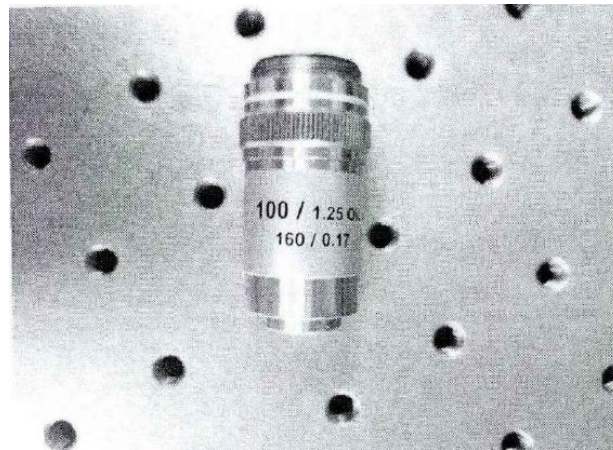
Figure 5.5 Photograph of the objective lens which is used in the optical tweezers.

5.1.4 Real-Time Visual Feedback System

In order to implement the detailed recording and the analysis for the motion process of the particles, the observational system of optical tweezers with high resolution is required and the whole monitoring system must have the functions for the real time observation and the continuous record of the particle motion. In general, the experimental operation process is recorded with the computer in real time. Sometimes, an ocular lens with the filter is used to make the operation more easily and reduce the damage caused by the high-intensity laser

| (A) | (B) |
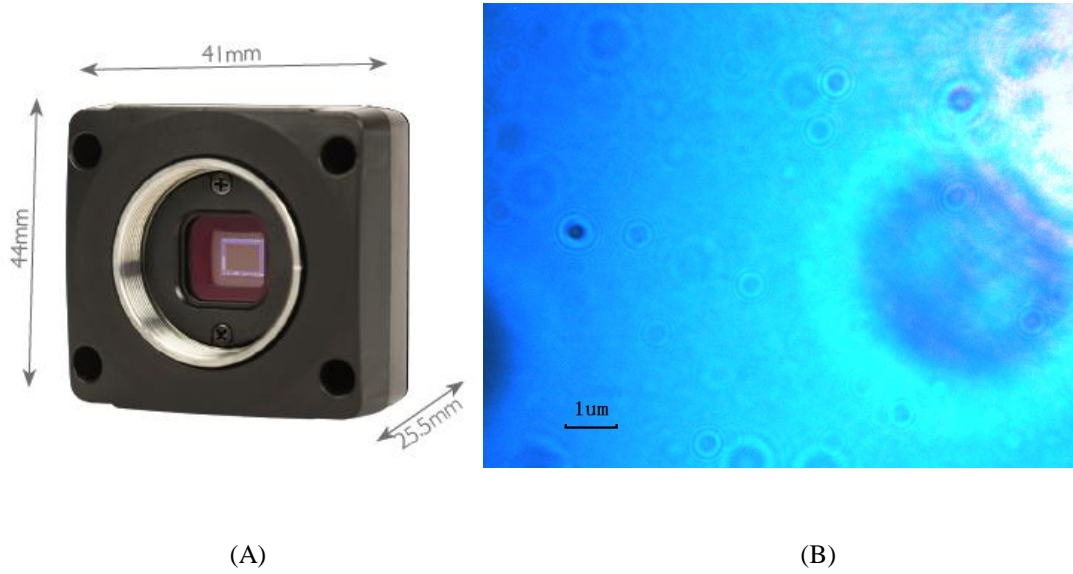
Figure 5.6 Overview of CMOS (A) and the imaging of the yeast cell obtained by CMOS (B).

As shown in Figure 5.6(A), the system uses the color CMOS 500 megapixel camera with maximum frame rate of 18fps, the number of effective pixel of 2592×1944. Thus, each pixel occupies an area of about $3.9\mu m \times 3.9\mu m$. In addition, the blue monochromatic cold light is applied as the light source so as to avoid the damage of cells, as show in Figure 5.6(B). The particle restricted by optical tweezers can move along with the position of the light focus. In the experiments of optical tweezers, it is required to accurately control the position of particle and manipulate the particle. Moreover, accurate and effective manipulation of optical trap is also the premise of measuring particle displacement and stress. Thus, it is vital for the optical tweezers to stably control the position of optical trap. The following section will introduce the manipulation method with the platform and optical tweezers.

5.2 Manipulation Method of Optical Tweezers

After the realization of stable capture, the placement manipulation of particles on the submicron scale by optical tweezers is the premise of implementing the cell tests. There are two methods for

optical tweezers to manipulate and control the particle, one is to keep the position of optical trap unchanged, and use the platform to drive the samples to realize the manipulation of the particle; the other is to change the position of optical trap through moving the laser beam and the moving distance of optical trap is the displacement of the particle.

5.2.1 Cell Movement by the Platform

In general, the common method for verifying if the biological particle is captured is to make sure that the position of optical trap remains unchanged, and slightly vibrates object stage. Then the relative motion of free cells and the cell restricted by optical tweezers can be observed by the real-time visual feedback system.

In the single optical tweezers, the micro/nano feed mechanism applied in the liquid-AFM has been used to control the sample moving on the micro/nano scale. After the area is selected, in order to implement the capture experiments for the target cell, the motion of nano displacement platform can be used to stably capture the target cell. This platform realizes the control of the movement speed and the displacement. In addition, the optical trapping force imposed on the cell can be obtained according to the motion and the escape velocity of cells, thus to quantify the stiffness of optical trap.

<div align="center">(A)   (B)</div>
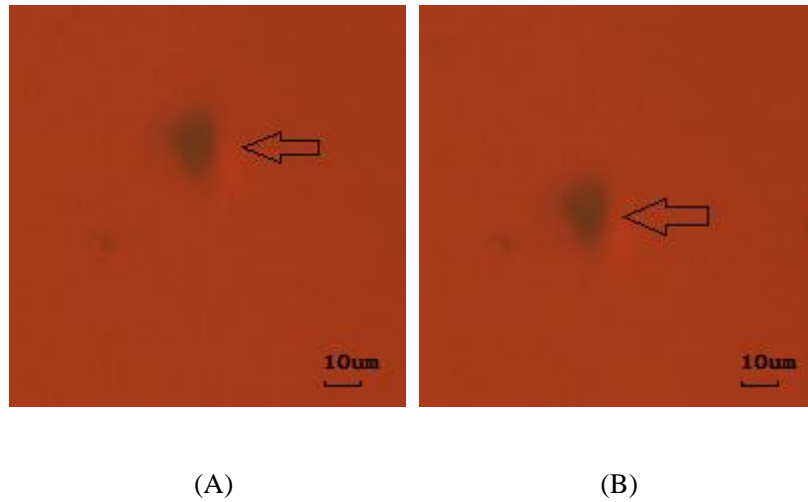
Figure 5.7 Schematic of the cell movement by the platform from (A) to (B) in the vertical direction.

Figure 5.7 shows the manipulation of the cell by using nano displacement platform. The cell near the light spot in the figure was stably captured by optical tweezers and the particle pointed by arrow moved along with sample stage from the top to bottom. By comparison, the captured cells do not move along with the sample stage and remain at the position of optical trap, so this system can manipulate cells through the mobile sample stage.

5.2.2 Cell Movement by the Laser Beam

The other method to implement the manipulation of particles is to keep the sample stage still and move the laser beam to realize the relative movement of optical trap and particle, thus to reach the purpose of particle manipulation. There are two modes to realize the transverse positioning of optical trap, namely translating the reflector and turning the mirror. The principle of both modes is to change the direction of transmission of light beam to make the light enter into the objective lens and change the focus position in the focal plane, thus to realize the purpose of manipulating particle. Figure 5.8 shows the movement of mobile light beam and focus position, after the laser enters into the objective lens.

(A)

(B)
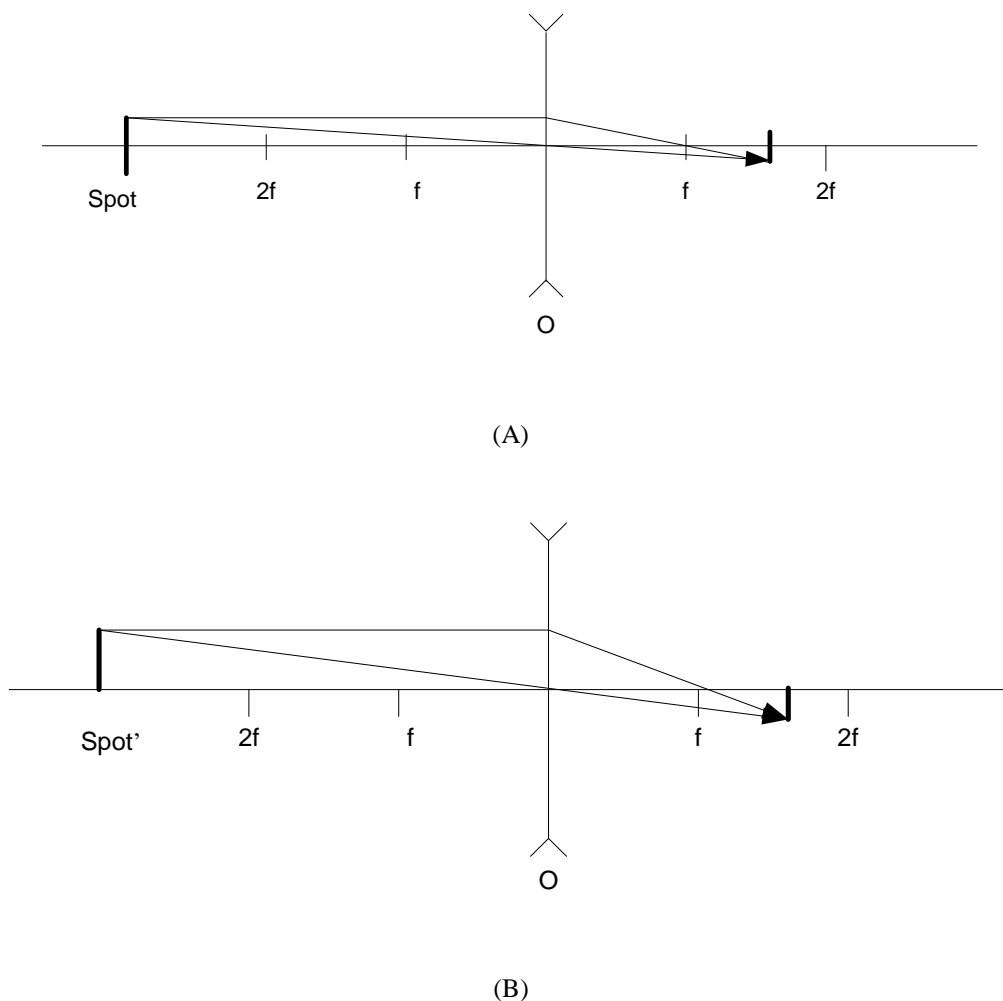
Figure 5.8 Schematics of the laser focus position when it is moved. The focus is moved by the laser phase shift. (A) The spot is placed beyond the two focal lengths, and it focuses between the focal lengths. (B) The focus is moving down with the movement of the spot.

Figure 5.9 shows the operation of the cell realized by the movement of laser beam. It can be seen clearly that the cell was moved from the middle of visual field to the edge of the left side, with the change of position of optical trap. The yeast cell indicated by the arrows is stationary as the reference cell and the trapped cell was moved by the laser phase shift from the right to the left.
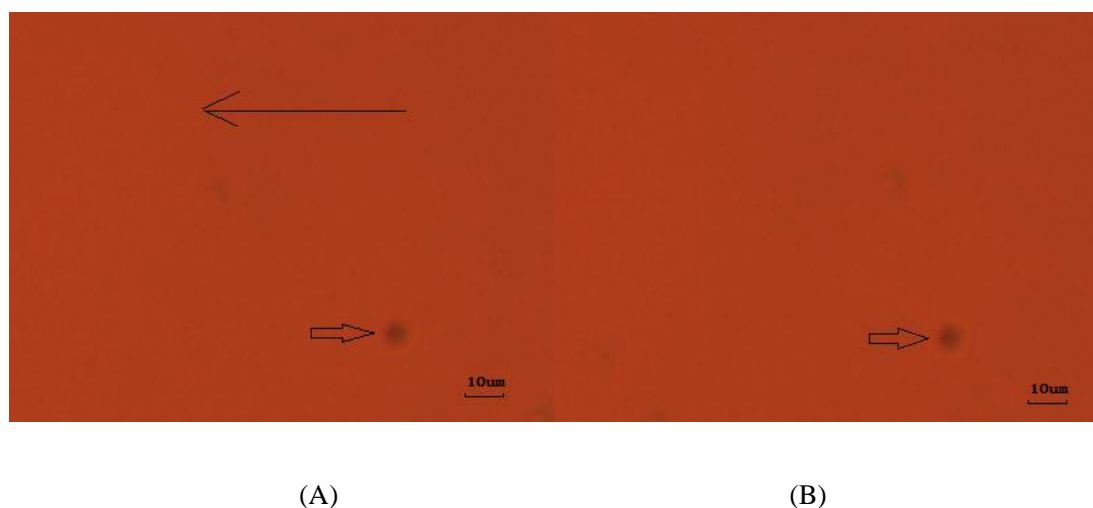
Figure 5.9 Cell movement by the laser beam from the right (A) to the left (B).

5.3 Measurement of the Cellular Escape Velocity

5.3.1 Yeast Cell Samples and Preparation

As a kind of microorganisms with the biggest direct edible amount by human, yeasts belong to unicellular fungi, which have stronger vital force and can survive in aerobic or anaerobic environment. Yeast cells have the typical structure of eukaryotic cells, such as cell wall, cell membrane, cell nucleus, cytoplasm and mitochondria, without flagella. The optical refractive index on its surface is 1.34, with an oval shape and the size of 6-10μm. Since the method of yeast cultivation is simple, rapid in the growth speed and easy in survival, it is widely used in biological research, especially in demonstration experiments where yeasts are usually selected. Moreover, in genetics and molecular biology, yeasts are important research objective. When preparing samples, the prepared dried yeasts are mixed with distilled water and white granulated sugar. At the temperature of 20℃, the yeast cells breed at the fastest speed. Thus, the yeast cells shall be placed in the environment at the temperature of about 20℃, so as to make them grow in a good condition. The breeding stage of yeasts is 2-5 days and the stage to keep a stable quantity of cells is about 8 days. In general, the yeast cells in breeding stage are applied to implement the experiment.

137

Because too long time in liquid will make the metabolite increase gradually, together with some dead cells, which will affect the manipulation of optical tweezers on the yeast cells.
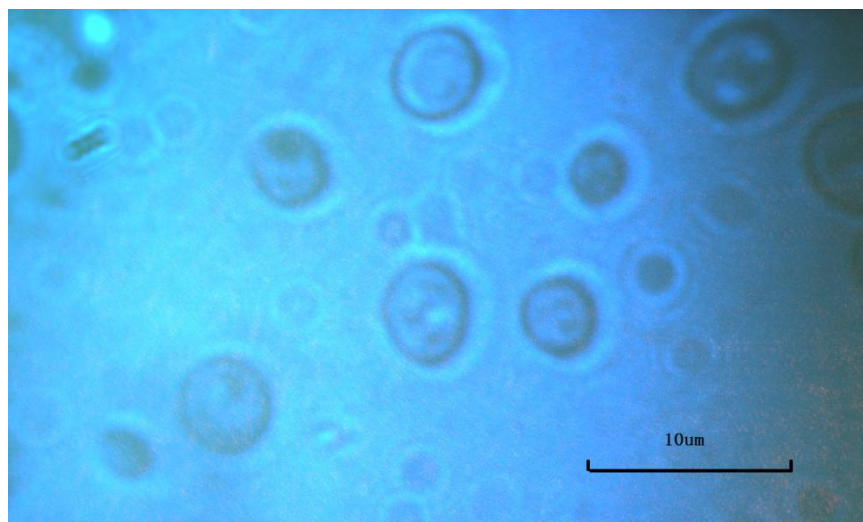
Figure 5.10 Prepared yeast cells under the optical tweezers.

Figure 5.10 shows that the prepared yeast sample is placed on the slide with a thickness of $0.17\mu m$ under the optical tweezers. Since the working distance of numerical aperture of the objective lens is very short, and if the slide is too thick, laser cannot focus in liquid that affects the utilization rate of numerical aperture, and the cell cannot be captured. To make it convenient for optical tweezers to have enough space for the cell manipulation and get better experimental results, the quantity of yeast cells in suspension and the scatter cells need to be reduced in the visual field. Thus, before the experiments, it is required to dilute the prepared suspension of yeast cells. According to the ratio of suspension of yeast cells and distilled water of 1:4, a sucker has been used to absorb appropriate amount of prepared suspension mixed with water and blow the diluted liquid to make yeast cells scatter completely, thus to implement the capture experiments of optical tweezers.

5.3.2 Methods

As described in Chapter 2, theoretical calculation could not substitute direct measurements, since the optical force is sensitive to small geometric deflections. Hence, the experimental methods such as the drag force method, the power spectrum method and the equipartition theory have been presented. Among them, the drag force method is the most frequently used to calibrate the optical stiffness in the optical tweezers operation. Huang et al used the method of fluid mechanics to make the particle trapped with relative uniform motion, then the relative speed of the particle was calculated when the particle and the resistance reached equilibrium states[132].

However, little work has been reported on the dynamic positioning analysis of the drag force method in the Z direction. When the particle deviates from the initial balance position due to the drag force of medium and reaches a new balance between the drag force and viscous force of light, the drag force could be calculated through the Stokes' law. Then an improved Stokes' law can be expressed as[133]

$$F_T = F_D = \frac{6\pi r \mu V_{max}}{1 - \frac{9}{16}(\frac{r}{h}) + \frac{1}{8}(\frac{r}{h})^3 - \frac{45}{256}(\frac{r}{h})^4 - \frac{1}{16}(\frac{r}{h})^5} \qquad (5.5)$$

where r is the radius of the particle, h is the distance from the focus sample, μ is the viscosity of the liquid, V_{max} is the maximum escape velocity of cell. Here, h is introduced into the Stokes' law and the algorithm of IFA (Image Focus Analysis) is used to obtain the distance. In this algorithm, the blurring level around pixels is decided by the distance between the planes of focus and objective lens. To obtain the different focus distances corresponding to the different blurring levels, continuous images of cells were acquired every 1μm, and the Laplacian function was used to analyse the blurring levels, which can be expressed as[134]

$$f(n) = \sum_{x} \sum_{y} [C(x, y)]^2 \tag{5.6}$$

where $C(x,y)$ is the result after the image processing by Laplacian function, and its template for the processing can be expressed as

$$\begin{bmatrix} 1 & 1 & 1 \\ 1 & -8 & 1 \\ 1 & 1 & 1 \end{bmatrix}$$

The search space corresponding to the distance is shown in Figure 5.11. From the focus plane to either the left edge or right edge, the clarity of images can be calculated by Laplacian function, as shown in Figure 5.11. Hence, the distance from the focus sample for each cell image can be judged from the result of Figure 5.12. The new experimental method integrated with the positioning analysis in the Z direction can characterize the mechanical forces applied to the living cell in the optical trap more precisely.
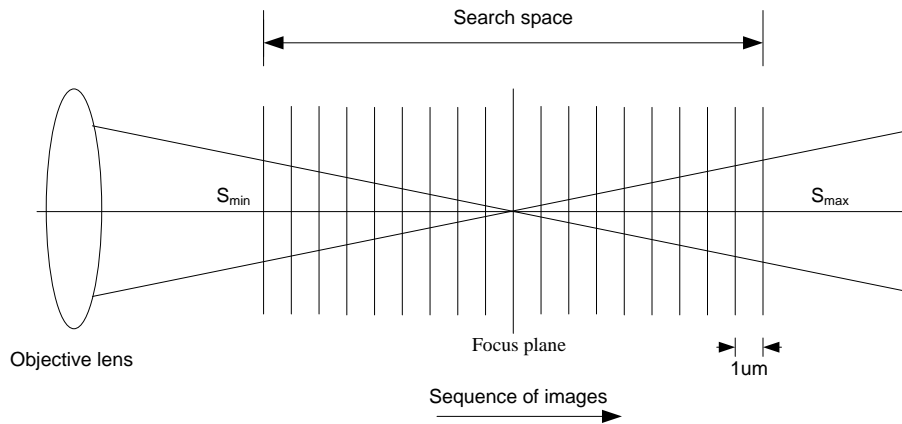
Figure 5.11 Schematic of the judgment of the image blurring level in each focus. The distance from the focus plane to either the left edge or right edge is about 1μm.
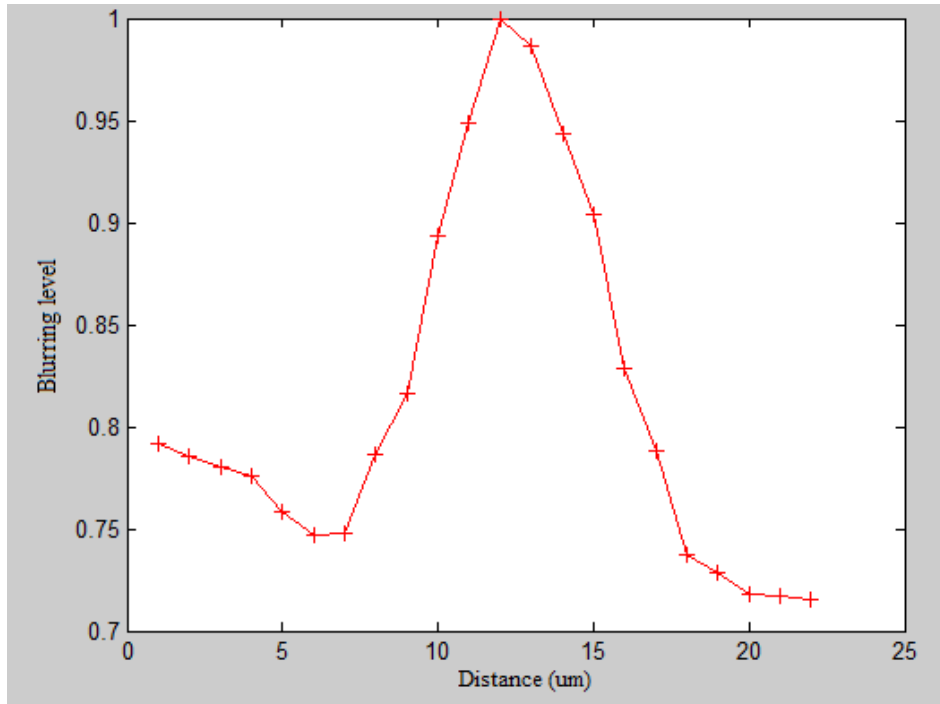
Figure 5.12 Corresponding focus curve calculated by the Laplancian function in the sequence of cell images.

5.3.3 Experiments and Results

In the experiments, the laser was focused on the sample plane, and the yeast cells were placed on the slide and they were driven to move with respect to the focus. The different optical trapping forces were calculated by the different drag velocities. When the drag velocity exceeded a speed limit, the cell came out of the focus. Then the drag force caused by the critical velocity was the cellular escape velocity. The output of the laser power was 100mW, and the oil-immersion objective lens with the NA of 1.25 and 100× magnification was used for the measurement of cellular escape velocity.

The yeast cells were used for the movement experiments in culture. The CMOS camera was set to record the whole manipulation process in real time. As shown in Figure 5.13, through the method of background superposition, the trajectory of that yeast cell can be seen clearly. The arrow points

the movement direction. From the image focus analysis, the height in the *Z* direction was about 1μm. The numbers of 1, 2, 3 showed the location of yeast cell at different times, and the time interval was 0.5s. Meanwhile, the operational velocity of the nano displacement platform was increased constantly as time increases until the yeast cell disengaging from the laser focus. The experiments were conducted under 20 ℃. Hence, the coefficient of culture viscosity was 0.963mPa/s, obtained by the capillary viscosimetry. The cellular escape velocity can be calculated by Eq. (5.5)[133].
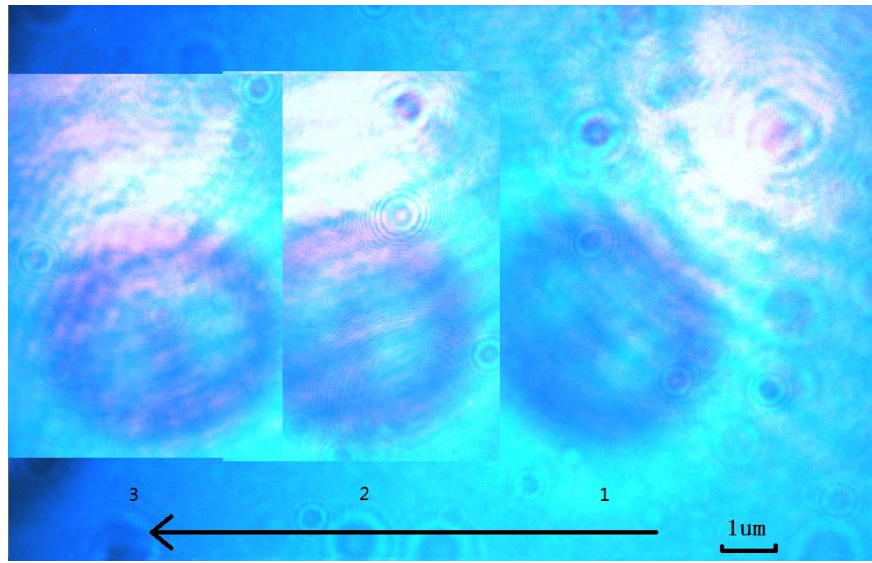
(A)
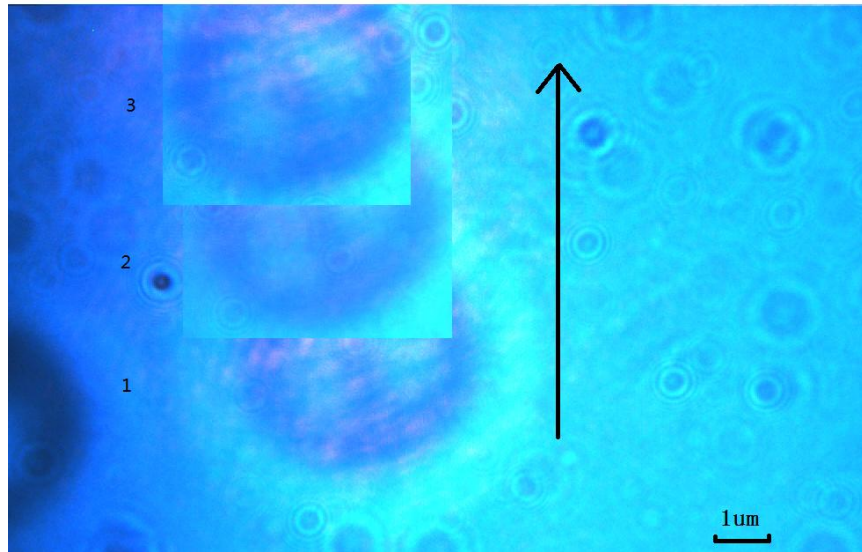
(B)
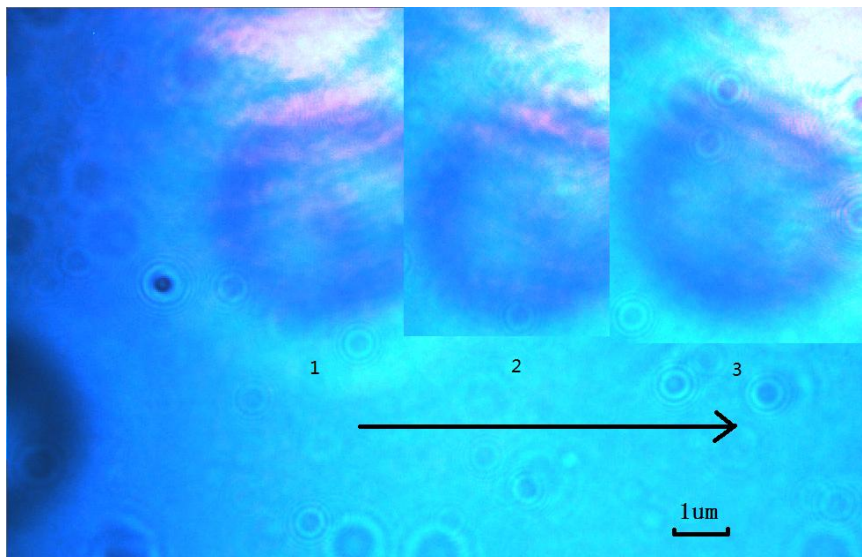
(C)

Figure 5.13 Schematics of the yeast movement. (A) The yeast cell has been dragged from the right to the left at the speed of 10.4μm /s. (B) The yeast cell has been dragged from the bottom to the top at the speed of 10.2μm/s. (C) The yeast cell has been dragged from the left to the right at the speed of 9.8μm/s.

As shown in Figure 5.13, the yeast cell is driven from the right to the left (A), the bottom to the top (B) and the left to the right (C), respectively. The cellular escape velocity can be calculated as 10.4μm/s, 10.2μm/s and 9.8μm/s, respectively. Hence, the mathematic model of least square surface fitting is utilized for the optical stiffness that the stiffness coefficient of the trapping force is k=(16.25±0.83)pN/μm, as shown in Figure 5.14, which is similar to the numerical computations by the RO model.
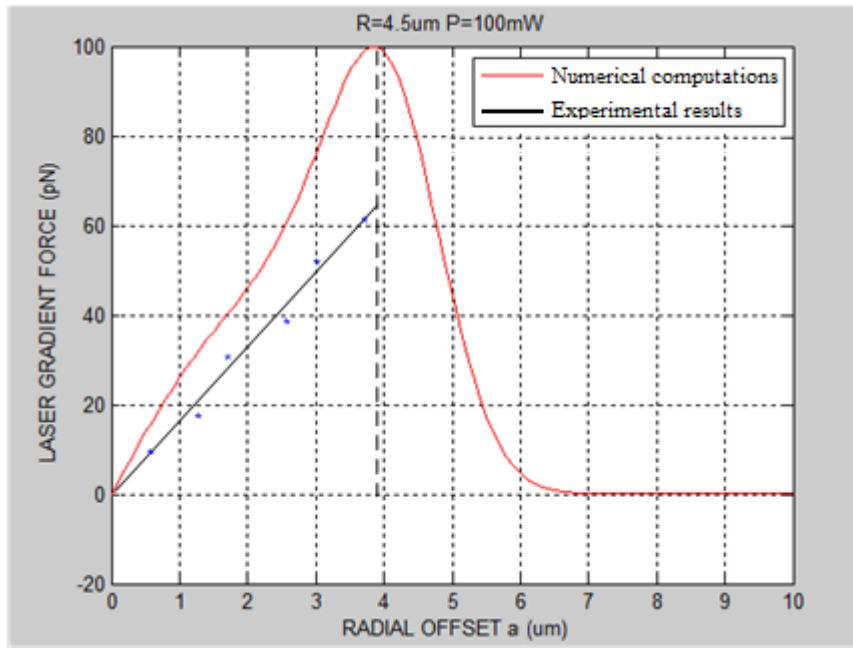
Figure 5.14 Comparison of the stiffness coefficient of the trapping force obtained by the numerical computations and the experimental results.

As shown in Figure 5.15, it is the drag experiment for yeast cell with different heights in the Z direction. From the image focus analysis, the height in the Z direction is about 5μm, and then the cellular escape velocity is about 4.4μm/s.
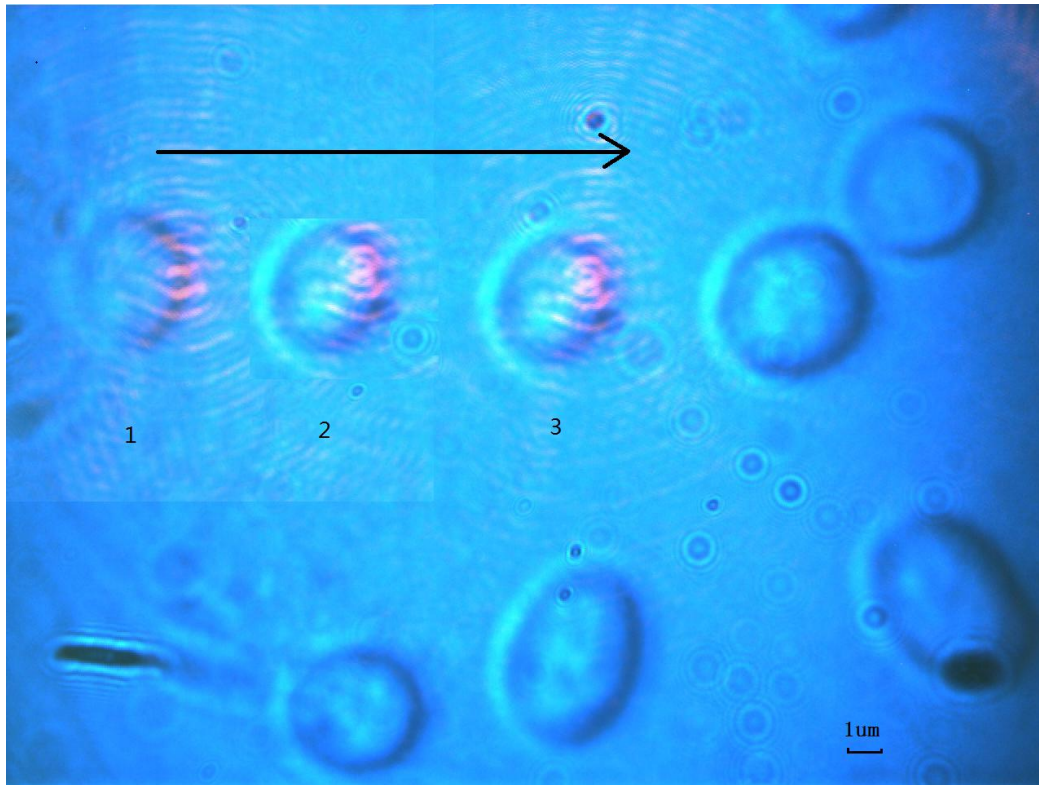
Figure 5.15 Schematic of the yeast movement with different positions in the Z direction.

Compared with the images of yeast cells on the different positions, they become apparent that the cell near the focus shows bigger than that placed higher from the focus, and the cellular escape velocity also appears quite different. Hence, the new experimental method includes the positioning analysis in the Z direction and can improve the fluid force method for the calibration and characteristic of the mechanical forces exerted on the optical trap and the living cell. Moreover, the algorithm of image focus analysis can help us precise position the yeast cell. When we perform an experiment, the cell must be placed on the same level. In addition, the environment is also the important condition for the cell testing. The background noise will severely affect the success of the cell trapping due to the trap force acted on the cell on the pN-scale. Hence, the yeast cells placed on the slide will be stilled for half an hour before the experiments and the whole experimental processes need to be conducted under quiet conditions.

Nowadays, the identifications of cancer cells are of the intriguing interest for researchers, especially for the early detection and diagnosis of cancer. The morphology of biological cells has no obvious changes in the early disease until to the terminal cancer. Actually, the cytoskeleton of the cancer cell has already changed at the early stage of cancerous tissue, which causes the different refractive-index distributions on the surface of the cell. Hence, the measurement of cellular escape velocity can provides a powerful tool for the early detection and diagnosis of cancer.

5.4 Summary

This chapter introduced the basic structure of optical tweezers, and an inverted imaging optical tweezers system was established. Moreover, the static drag force method of measurement was used to measure the cellular escape velocity in culture, and further obtained the trapping stiffness similar to the numerical computations by the RO model described in Chapter 2. Among them, the new experimental method included the Z direction analysis and was used to improve the fluid force method for the calibration and characterize the mechanical forces exerted on the optical traps and living cells. Different focus distances were selected to check the validity of the new measurement method, and the algorithm of image focus analysis was used to calculate the distance. The experimental results have shown that the cellular escape velocity of the biological cells in different levels of sample plane appears quite different. In conclusion, the key technical properties and the applications of optical tweezers can realize more effective manipulation and better observation of biological cells due to its inherent advantages, including remote contact, less mechanical damage and accurate manipulation. The cellular escape velocity provides a powerful tool for the early detection and diagnosis of cancer which improves the nano handling and measurement technology by liquid-AFM. However, due to the focus of one trap on the object surface, the traditional optical tweezers cannot achieve the manipulation of multi-objects in a high efficiency and it cannot isolate the particular type cells which usually exist in the mixture of

several different morphologies of samples. Hence, a sensitive and highly efficient polarization-controlled three-beam interference optical tweezers is developed in the followed chapter.

Chapter 6

Capture and Sorting of Multiple Cells by Polarization-Controlled

Three-beam Interference

6.1 Introduction

In recent years, the optical technology has been actively developed to play an important role in bioscience, especially in targeted drug delivery[135], trapping of macromolecules such as RNA and DNA[136][137] and living cellular adhesion measurement[138]. Moreover, in the research field of biophysics, the particular type cells usually exist at the mixture of several different morphologies of samples, which need to be isolated and purified for further observation and analysis, such as the recent research of CTLs (Cytotoxic T Lymphocytes) to find and kill cancer cells[139]. How to find CTLs and control them close to the cancer cells are both important for the work. Hence, the optical trapping has been presented with the features of remote manipulation and less damaging.

In contrast to the current experimental methods based on one beam optical trap that it just manipulates one particle in one operation, there is a need to trap a number of particles simultaneously using the basic theory of optical tweezers. Some techniques to create spatially distributed multiple optical traps on various applications have been reported such as the SLM which uses computer generated diffraction patterns[140], fast laser-scanning which is usually created by time-sharing of a single laser beam[141][142], and multiple light sources which are usually generated by diffractive elements or and LBI (Laser Beam Interference)[143]. The most approaches so far are those of using the spatial light modulator based on the high numerical aperture objective

lens to create computer-generated holography optical traps, which could independently trap micro/nano particles in 3D. However, such methods are limited to manipulate small number particles in real-time due to their complex and expensive constructions. Those still prevent the multiple optical traps from being used as the general research instrument.

LBI is a promising technology for the volume creation of a large regular array of optical traps with easily constructed and inexpensive micro-lenses. This method does not require strongly focused beams and provides a way to generate periodical and quasi-periodical optical traps with adjustable periods and less damaging, so that simultaneous spatial manipulation of a large number of particles can be achieved[144]. However, compared with the current approaches, most of studies for the creation of multiple optical traps are limited to only create a pattern of linear interference fringes or a few dot traps without the adjustment of the formation. Furthermore, the trapping force is only adjusted by the changing of laser intensity and it is not stable due to the output variations.

Addressing these shortcomings, a novel adjustable three-beam interference method was presented. It combined the optical tweezers to generate hundreds of optical traps in one focus, with its simple form requiring several interfering laser beams whose spatial frequency components lie on the vertices of an equilateral triangle. The resulting interference pattern has a sinusoidal modulation of its intensity distribution along the lattice vector directions. Incorporating additional beams can make these maxima better defined, but more importantly, it can introduce an axial intensity modulation such that these maxima are localized in the 3D. The different sizes of cells could be manipulated by the adjustable periodic structures focusing on the yeast suspensions. We demonstrated the trapping of yeast cells in an interference array of dots with regular triangle structures, and provided the force analysis of yeast cells in the laser interference fields. From the real-time visual feedback by CCD, the different sizes of cells were manipulated by laser interference with different polarization angles in the same case.

6.2 Interaction of the Periodic Structures of Gradient Laser Field with Yeast Cells

6.2.1 Generation of the Periodic Structures of Gradient Laser Field

In this work, three-beam laser interference was used to generate laser interference patterns in the sample plane, as shown in Figure 6.1. The theoretical equations based on the three-beam laser interference were derived with proposed polarization modes. Laser interference pattern can be seen as the superposition of the electric field vectors when two or more coherent beams focus on one point.
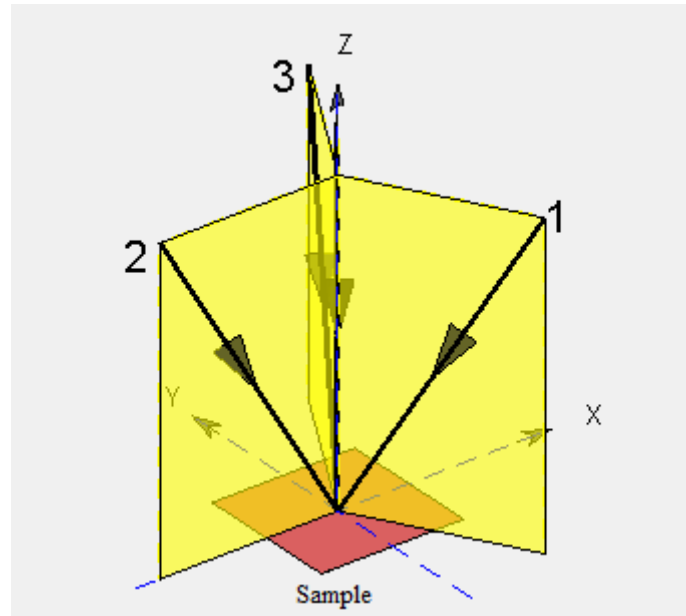
Figure 6.1 Schematic set-up for the three-beam laser interference system.

The electric field vector E_n of each coherent beam can be expressed as[145]

$$E_n = A_n p_n \exp[i(k_n \cdot r - \omega t + \delta_n)] \qquad (6.1)$$

where A_n is the amplitude of each beam, p_n is the polarization vector, k_n is the wave

number, r is the position vector, the wave surface of plane wave is the plane when $k_n \cdot r$ equals to the constant. ω is the angular frequency, i is the imaginary number, and δ_n is the initial phase. In the adjustable three-beam interference experimental setup, the three beams are allowed to form a symmetrical configuration with the same incident angles and the azimuthally angle φ_n is fixed as $0°$, $120°$ and $240°$, respectively. Therefore, p_n and k_n (n=1, 2, 3) can be expressed as

$$\begin{cases} p_1 = -(\cos\theta\cos\psi_1) \cdot x - \sin\psi_1 \cdot y - (\sin\theta\cos\psi_1) \cdot z \\ p_2 = (\frac{1}{2}\cos\theta\cos\psi_2 + \frac{\sqrt{3}}{2}\sin\psi_2) \cdot x - (\frac{\sqrt{3}}{2}\cos\theta\cos\psi_2 - \frac{1}{2}\sin\psi_2) \cdot y - (\sin\theta\cos\psi_2) \cdot z \\ p_3 = (\frac{1}{2}\cos\theta\cos\psi_3 - \frac{\sqrt{3}}{2}\sin\psi_3) \cdot x + (\frac{\sqrt{3}}{2}\cos\theta\cos\psi_3 + \frac{1}{2}\sin\psi_3) \cdot y - (\sin\theta\cos\psi_3) \cdot z \end{cases} \quad (6.2)$$

$$k_n = k(\sin\theta\cos\varphi_n \cdot x + \sin\theta\sin\varphi_n \cdot y - \cos\theta \cdot z)$$

where x, y and z are the unit vectors in the three directions of coordinates. θ_n is the incident angle, ψ_n is the polarization angle, $k = 2\pi/\lambda$ is the wave number, and λ is the wavelength of light.

According to Eqs. (6.1) and (6.2), the intensity distribution of three-beam interference can be expressed as

$$I(r) = \sum_{n=1}^{3}\sum_{m=1}^{3} |E_n||E_m|\cos\langle E_n \cdot E_m \rangle = \sum_{n=1}^{3}\sum_{m=1}^{3} A_n p_n \cdot A_m p_m \cdot e^{[i(k_n - k_m)r]} \quad (6.3)$$

with the spatial period[145]

$$d_0 = \frac{\lambda}{2n_m \sin\theta} \quad (6.4)$$

where n_m is the refractive index of the surrounding medium.

The distributions of interference patterns generated by computer simulation with different polarization modes are shown in Figure 6.2. The intensity distributions of interference patterns can be changed by the polarization mode, such as regular triangle distributions, elliptical distributions and circular distributions. Compared with other multi-beam interference methods, three-beam interference has the advantage of generating no modulation which can be easily controlled in the interference field. Hence, the polarization angle becomes a potential parameter for controlling the intensity distribution of the interfering field. By changing the polarization angle of three interference beams, various intensity distributions are obtained, as shown in Figure 6.2.
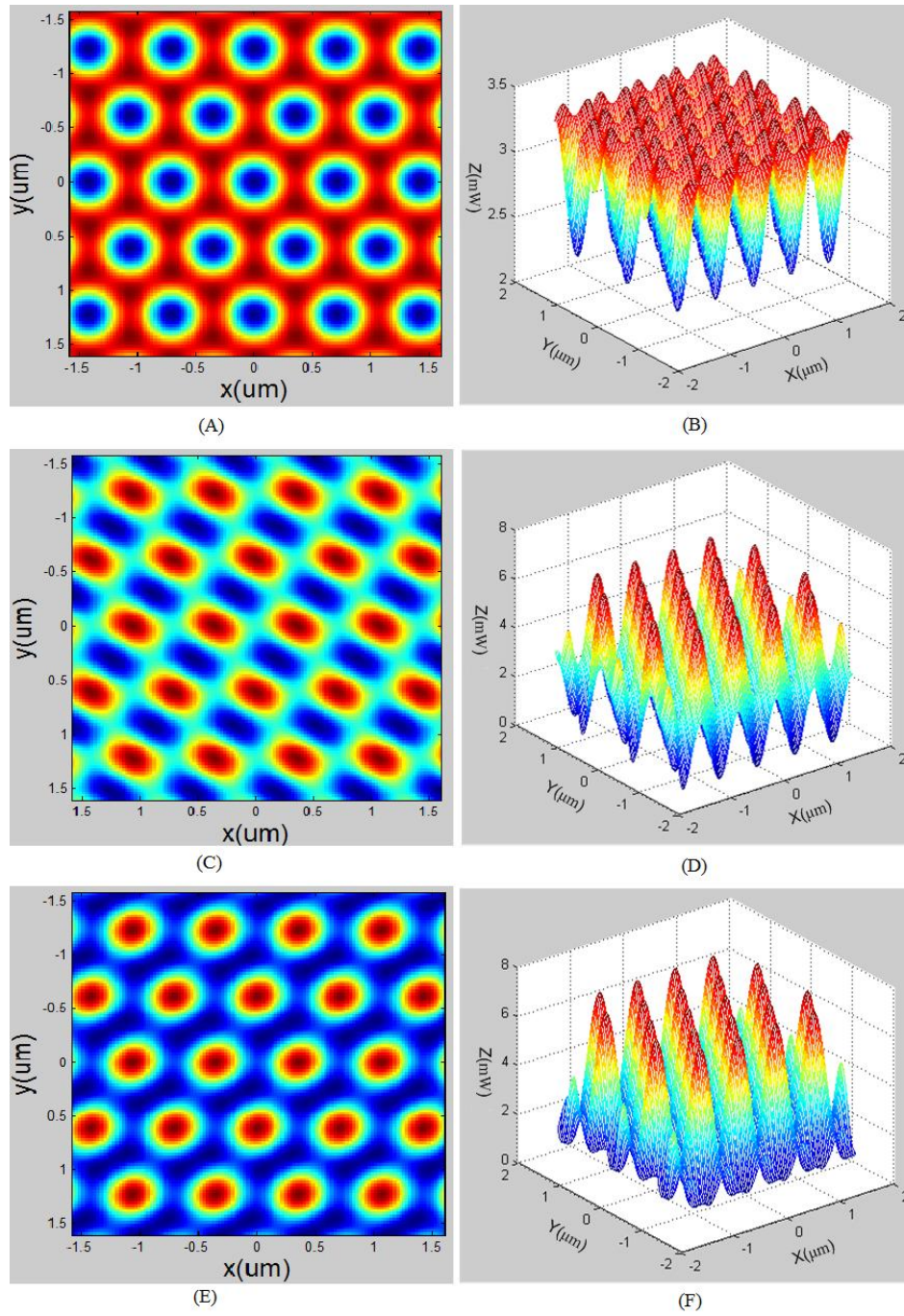
Figure 6.2 Computer simulations of laser interference. (A), (C) and (E) 2D intensity distributions for three-beam interference with the polarization modes of TE-TE-TE, TE-TM-TM and TE-TE-TM, respectively. (B), (D) and (F) 3D intensity distributions for three-beam interference with the polarization modes of (A), (C) and (E), respectively ($\lambda = 532\text{nm}, \theta = 30°$).

153

In addition, the angles between three beams in the adjustable three-beam interference experimental setup are also varied, as shown in Figure 6.3. If the three beams have the same polarization, the intensity distributions in Figure 6.3 are calculated using three beams, which give an approximation to the optical field in the regions close to the optical axis and the image plane, and are shown to be consistent with the experimental results in different azimuthal and incident angles. Those different shapes of the interference pattern are used to form different trap shapes, which can realize the selection of the specific cell type. However, the azimuthal angle in the interference system is difficult to be adjusted in real time, and the incident angles of three beams are also needed to provide the equilibrium conditions along the axial direction, or the interference plane is not leveled and the interference structure is not appeared with the uniformly periodic distributions. Hence, the azimuthal angles keep their locations at the fixed values, respectively. The polarization angle becomes the prime parameter for modulating the intensity of the interfering field in real time. Then, the gradient force will be changed with the polarization angle in the interfering field.
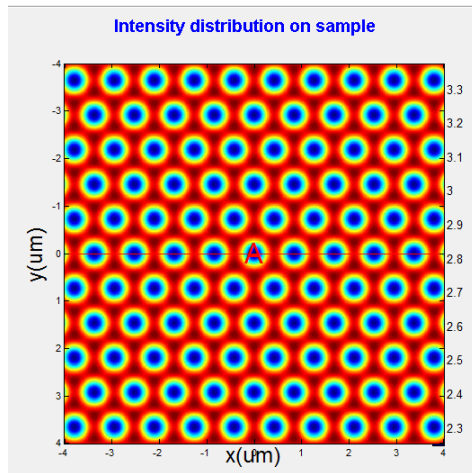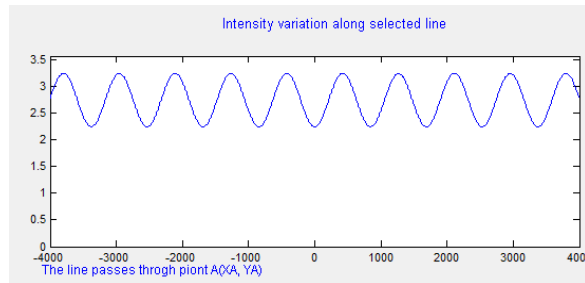
(A)   (B)
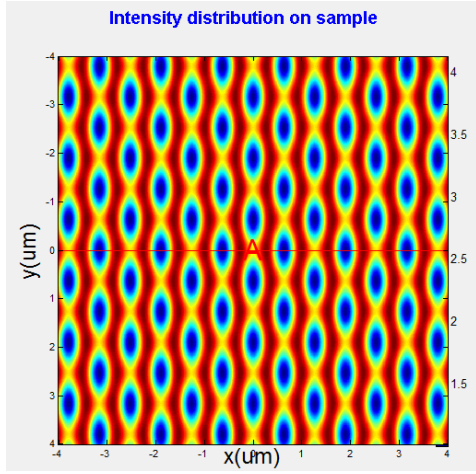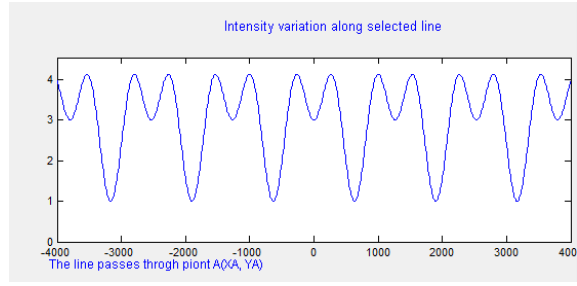
(C)   (D)
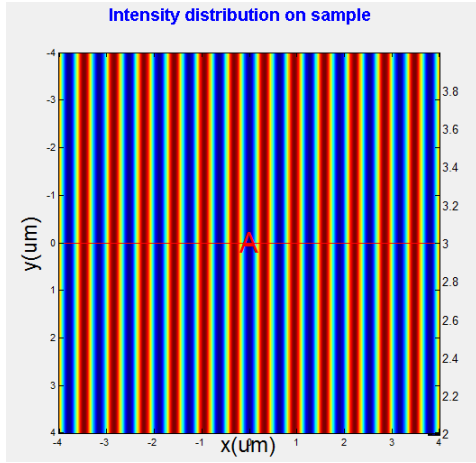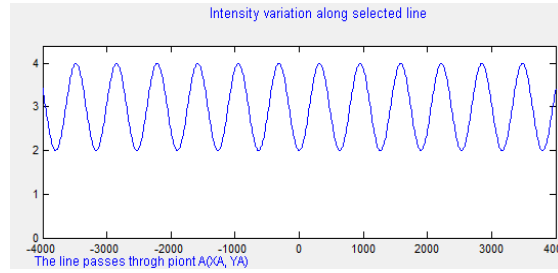
(E)   (F)

Figure 6.3 Three-beam laser interference patterning with simulations: (A) azimuthal angles of $\varphi_1 = 120°$, $\varphi_2 = 240°$, $\varphi_3 = 360°$ and the incident angles of $\theta_1 = \theta_2 = \theta_3 = 30°$; (B) azimuthal angles of $\varphi_1 = 180°$, $\varphi_2 = 270°$, $\varphi_3 = 360°$ and the incident angles of $\theta_1 = \theta_2 = \theta_3 = 30°$; (C) azimuthal angles of $\varphi_1 = 180°$, $\varphi_2 = \varphi_3 = 0°$ and the incident angles of $\theta_1 = \theta_2 = 30°, \theta_3 = 0°$; (D), (E) and (F) the cross-sectional views of (A), (B) and (C), respectively.

6.2.2 Gradient Force in the Interference Field

In the previous work, it demonstrated that only the gradient force existed in the transverse direction without any component of the light pressure force when the standing wave acted on a particle[146]. The gradient force could originate from the interaction of the light-induced dipole moment between the electrical component of light and the particle[147]. In this section, we discuss the influence and the orientation of gradient when the particle is placed in the three-beam interference field, and the sample is considered as a spherical particle. According to the report of Rohrbach et al., the polarizability of particle can decide the strength of both forces. Only the gradient force acts on the particles placed into the interference field, they can move towards the maximum intensities of the periodic interference structures[148].
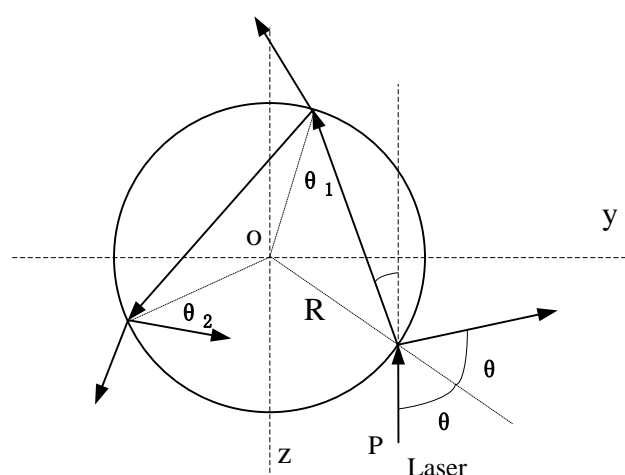
Figure 6.4 Schematic of the laser incident upon the lower side of the particle[149].

As shown in Figure 6.4, it is the typical transparent particle assumed to be located close to the central axis of a stream of photons. On the surface of the particle, part of the photons are reflected and another are refracted which are deviated from the initial direction and incident onto the upper surface of the particle. Then the photons continues to be reflected and refracted in the next location. Hence, due to the reflected or transmitted photons at the lower or upper parts of the

particle surface, the gradient force can be expressed as[149]

$$
\begin{aligned}
F_{grad} = & -\int_0^{\pi/2}\int_0^{2\pi} I\,(\rho,z\,)\frac{n_0}{2c}\sin(2\theta)|r_1|^2\,r^2\cos(\phi)\times\sin(2\theta)d\phi d\theta \\
& +\int_0^{\pi/2}\int_0^{2\pi} I\,(\rho,z\,)\frac{n_s}{2c}\sin(\theta-\theta_1)|t_1|^2\,r^2\cos(\phi)\times\sin(2\theta)d\phi d\theta \\
& +\int_0^{\pi/2}\int_0^{2\pi} I(\rho,z)\frac{n_s}{2c}[\sin(3\theta_2-\theta)-\sin(\theta-\theta_1)]\times|t_1|^2|r_1|^2\,r^2\cos(\phi)\sin(2\theta)d\phi d\theta \\
& +\int_0^{\pi/2}\int_0^{2\pi}\frac{I(\rho,z)}{2c}\left\{n_0\sin[2(\theta-\theta_1)]-n_s\sin(\theta-\theta_1)\right\}|t_1|^2|t_1|^2\,r^2\cos(\phi)\sin(2\theta)d\phi d\theta
\end{aligned}
\tag{6.5}
$$

where n_s is the refraction index of the particle, n_0 is the refraction index of the surround, r is the radius of the particle and c is the speed of the laser in the surround. In the equation, the power reflectance for the lower surface of the particle can be written as[150]

$$
|r_1|^2 = \frac{(n_0 n_s)^2[\cos^2(\theta)-\cos^2(\theta_1)]^2}{\left\{n_0 n_s[\cos^2(\theta)+\cos^2(\theta_1)]+(n_o^2+n_s^2)\cos(\theta)\cos(\theta_1)\right\}^2}
\tag{6.6}
$$

Moreover the power transmittance can be written as

$$
|t_1|^2 = 1 - |r_1|^2
\tag{6.7}
$$

The intensity profile of the beam $I\,(\rho,z\,)$ can be written as the lowest-order Gaussian mode[150]

$$
I\,(\rho,z\,) = \frac{2P}{\pi W^2}\exp[\frac{-2\rho^2}{W^2}]
\tag{6.8}
$$

where ρ is the gradient distance from the axis of the laser. W is the width of the laser which given by[149]

$$W = W_0[1 + (\frac{z}{z_0})^2]^{1/2} \tag{6.9}$$

where z and z_0 are the distance measured along the beam's direction of propagation with $z=0$ and

$I(\rho, z) = I_{max}/2$, respectively.

Hence, the TE-TE-TE mode, TE-TE-TM mode and TE-TM-TM mode were programmed in Matlab with Eq. (6.5) for the numerical computation purposes. Each dot in the interference field was used as one incident beam in the simulation. Figure 6.5 shows the force in a sphere cell as a function of the interaction between the dot center and the central axis of cell. The radial offset a is the relative offset between the beam center and the central axis of cell. W_0 is the width of each dot in the three-beam interference pattern. The parameters for the particle and the beam were chosen as n_s=1.5468 and n_0=1.333. The laser power for each dot was 20mW, the wavelength of the laser was 532nm and the radius of the particle was 2.5µm. As shown in Figure 6.5, the laser gradient force acted on the cells can be changed by the different sizes of dots in the interference field. The comparison of the laser gradient force curves with different widths of dots shows that the gradient force can be much larger when the size of cells is approximately equal to W_0. The gradient forces also act over a smaller range around the dot center. Moreover, the trapping force will start falling when the offset is greater than 3µm which has almost the same conclusion as that in the following section. Hence, the neighboring optical trap will not influence the particle due to the rapidly decreased trapping force.
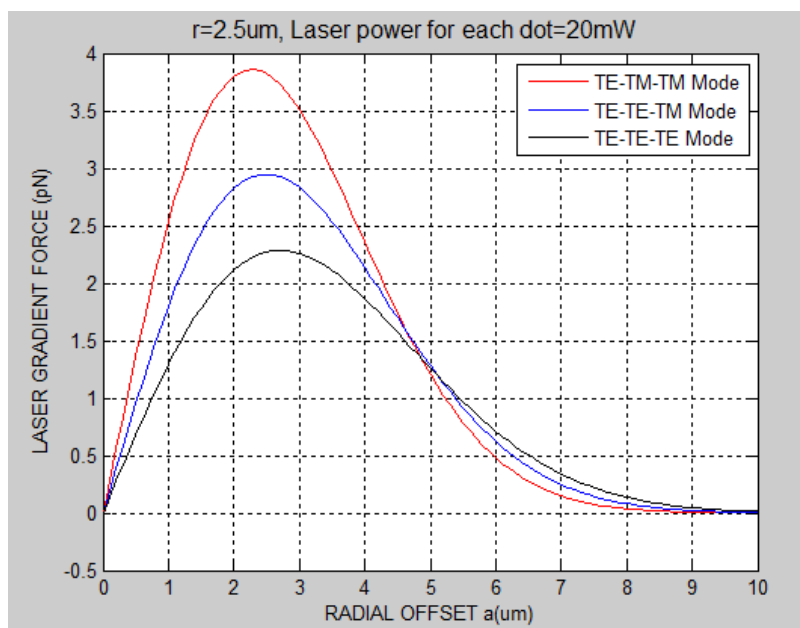
Figure 6.5 Laser gradient force versus the radial offset. The cell located in the interference field experiences a centering force pulling it into the alignment with the central axis of dot.

6.3 Experimental Setup

The polarization-controlled three-beam interference experimental set-up is shown in Figure 6.6. It is essentially based on two blocks: an adjustable three-beam interference system for producing the periodic structure and a real-time visual feedback system for monitoring and photographing the capture and movement of cells.
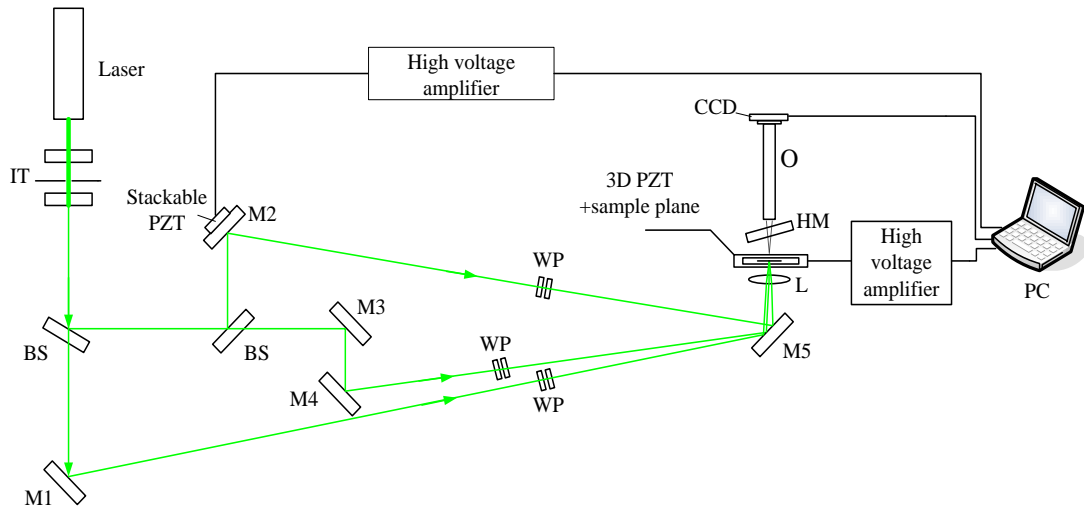
Figure 6.6 Beam geometry for polarization-controlled three-beam interference experimental set-up. The three interfering beams are placed symmetrically around the z axis and with the angle θ. IT, inverted Kaplerian telescope system; M, mirror; BS, beam-splitter; WP, half-wave plate and polarization prism; L, lens; O, microscope; CCD, charge-coupled device; PZT, piezoelectric ceramic transducer; PC, personal computer.

A semiconductor continuous laser with output power from 0 to 2W made by CNI (Changchun New Industries Optoelectronics Technology) operating in the TEM_{00} mode at 532nm is used as the light source. It can provide both the distinct periodic structure in the visible spectral range with a long coherence length and the necessary gradient force by the intensity, as shown in Figure 6.7. The beam diameter at the aperture is about 2mm and its divergence is less than 1.5mrad.

Figure 6.7 Photograph of the semiconductor continuous laser.

Firstly, due to the non-uniform Gaussian beam interference produced in the same non-uniformity distribution of periodic structures, an inverted Kaplerian telescope system including two positive focus lenses with different focal lengths and a pinhole of 50μm was used to improve the quality of laser. Unlike the general application, the focal length of f_1 is larger than that of f_2. In the experiment, the f_1=100mm and f_2=35mm lenses were used, and the magnification was 1/2.85 times. Moreover, due to the uneven intensity distribution in the input Gaussian beam, a diameter of 50μm pinhole is used in the experiment to improve the spatial quality of the beam, as shown in Figure 6.6.
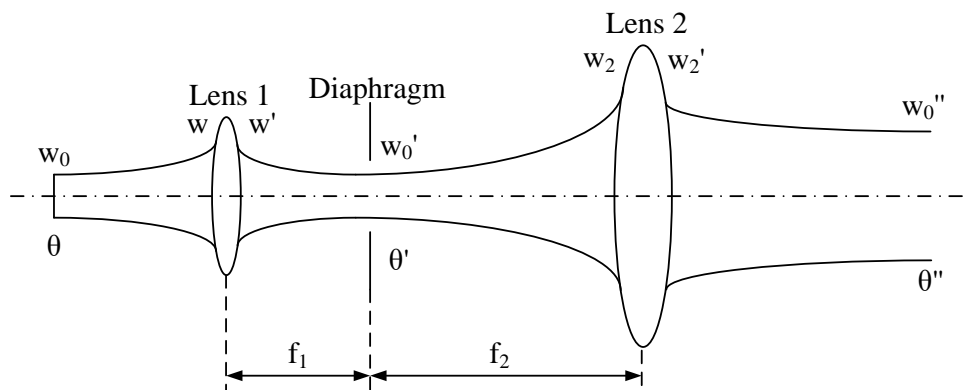
Figure 6.8 Schematic of the inverted Kaplerian telescope system.

The emerging beam from the alignment and filtering system has a diameter close to 1mm and is split by two 50:50 BSs (Beam Splitters) into three beams and focused by the 10cm focal length lens L on the sample plane.

In the experiment, the interference pattern in the sample plane was formed into about 100μm spots overlapping in space. Meanwhile, a 3D PZT (piezoelectric ceramic transducer) controller together with the sample stage was used to operate the sample moving on a flat surface and make the sample matching to the three-beam focus, and a stackable PZT stuck with the mirror 5 was used to achieve the accuracy of phase shift and stabilize the interference gradient force on the sample plane, as shown in Figure 6.8.
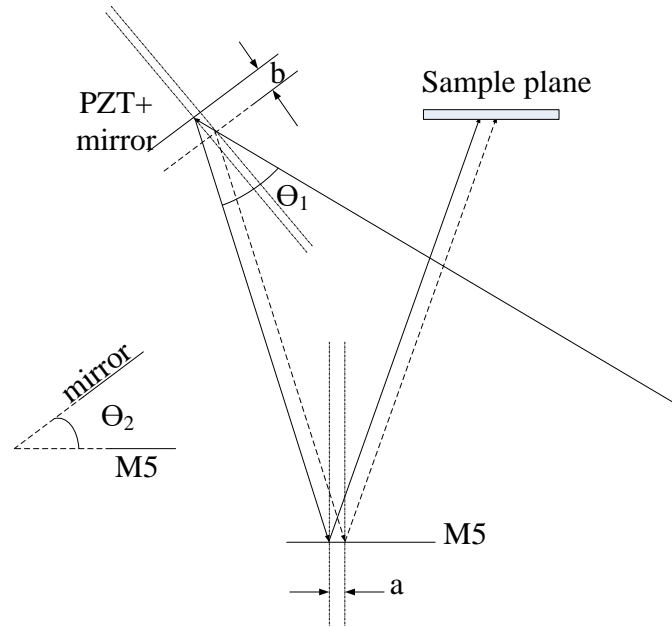
Figure 6.9 Schematic of the phase shift on the sample plane.

Figure 6.9 shows the phase shift in the sample plane, and the beam incident angle equal to $\theta_1/2$, the lens and base angle is θ_2. If the PZT moves b, then the base beam shift a can be calculated as following

$$a = \frac{\dfrac{b}{\cos^{\theta_1}\!\big/2} \cdot \cos\theta_1}{\tan(\dfrac{3\theta_1}{2} - \theta_2 - \dfrac{\pi}{2})} \qquad (6.10)$$

The stackable PZT is ferroelectric crystal, which consists of many tiny grains that inset irregularly. Thus, because of the artificial polarization, it will emerge the piezoelectricity effect. Along the direction of the polarization, it has a rotational axis of symmetry. In terms of the essence of PZT, the crystal lattice of dielectric distortion through the polarization has been made under the action of the electric field. These effects represent mechanical strain in the macroscopic electromechanical coupling. The output displacement and the driving voltage of piezoelectric ceramics can be calculated as[151]

$$\Delta h = D(v)V \qquad (6.11)$$

where $\Delta h = \dfrac{\Delta\theta}{2\pi} \cdot \lambda$ is the stretching quantity , which represents the phase shift ($\Delta\theta$) of a single wavelength (λ), $D(v)$ is the piezoelectric coefficient, V is the voltage exerted on the PZT. It is an excellent phase shift device, which has many advantages, such as easy adjust, stabilization and small size .

In applications, PZT can produce some characters like the hysteresis or the creep which affects the accuracy of the phase shift. In order to precisely control the PTZ operation in the experiments, we need to know the quantitative relationship between the voltage and displacement by PZT, and how to determine the best linear interval of PZT in the repeatability experiments. As shown in Fig. 6.10(A), the phase shift of the interference pattern introduced by the PZT is implemented with a voltage of 0-60V and the CCD detection in real-time. Fig. 6.10(B) shows the phase shift between two adjacent voltage values 5V.
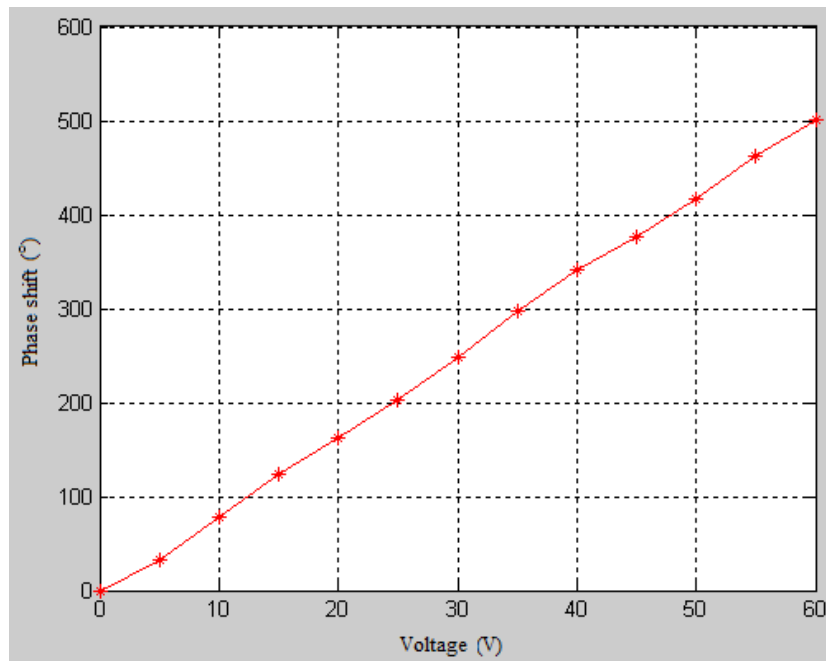
(A)
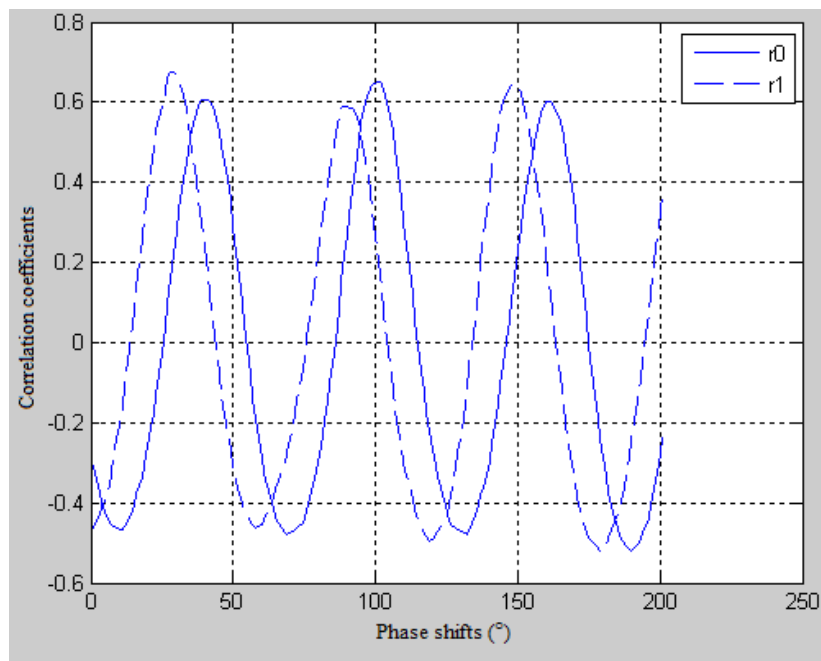
(B)

Figure 6.10 Phase shift of the interference pattern induced by the PZT. (A) Phase shift with voltages from 0V to 60V. (B) Phase shift between two adjacent voltage values 5V.

164

The observation part consisted of a flat mirror HM for the reflection of 532nm laser beam, and the microscope O for imaging the sample plane on a CCD camera. Finally, the images were transmitted to the computer. Three polarizers were chosen as the modulation devices to change the output energy and the polarization angles. The various interference patterns were formed by different combinations of polarization angles when they had the same incident angles. According to the real-time visual feedback by the CCD camera, the computer was able to obtain the information of sample cells. Then, the matching interference pattern was adjusted by changing the laser polarization angles. As shown in Figure 6.11, it is the photo of the polarization-controlled three-beam interference experimental set-up.
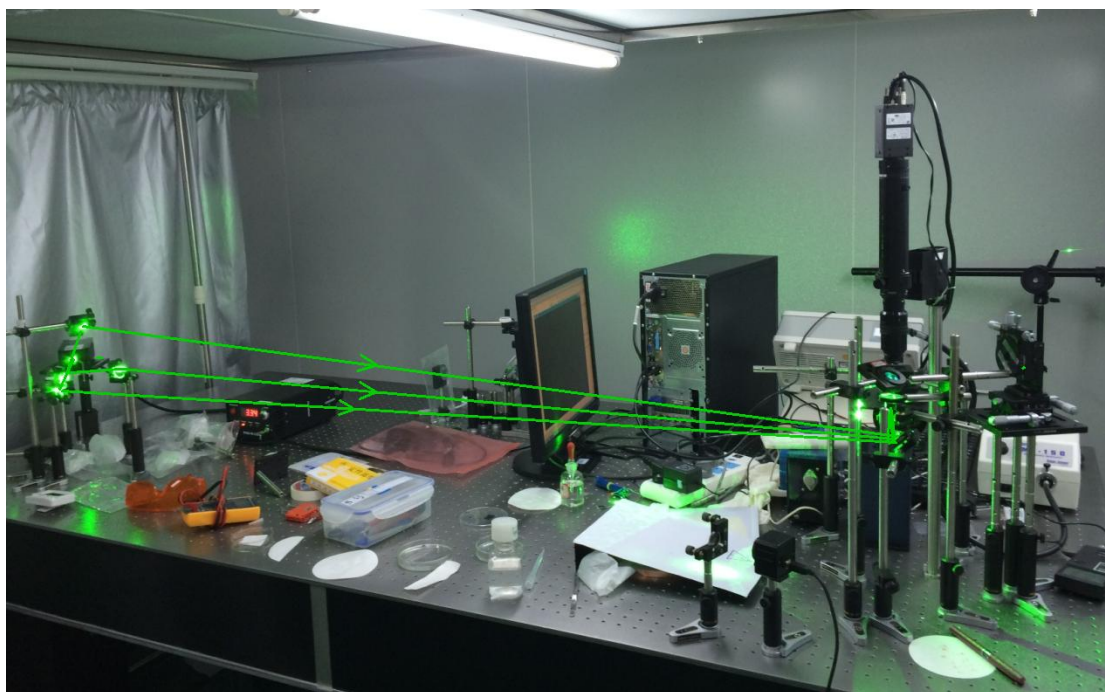
Figure 6.11 Photograph of the polarization-controlled three-beam interference experimental set-up.

6.4 Results and Discussions

6.4.1 Optical Trapping and Manipulation of Yeast Cells

The yeast cells with spherical shapes were manipulated in culture for the experiment. All of pelleted cells were grown for 24 hours. An aliquot of sedimentated yeast cells amount was diluted in 10 times with the deionized water without stirring. The yeast suspensions were placed on a non-coated cover-slip when the cells were captured by the adjustable three-beam interference experimental setup described above. The period of interference pattern was chosen slightly larger than the average diameter of yeast cells, and the laser intensity at the centre of the interference pattern was about 950mW. We observed the multiple yeast cells captured by the laser gradient force originated from the interaction of light-induced dipole moment. Figure 6.12 shows that the optical trapping of tens of yeast cells in the interference field was achieved. With the laser gradient forces, the whole array of optically trapped yeast cells could be dragged by the movement of PZT.

(A)   (B)

(C)   (D)
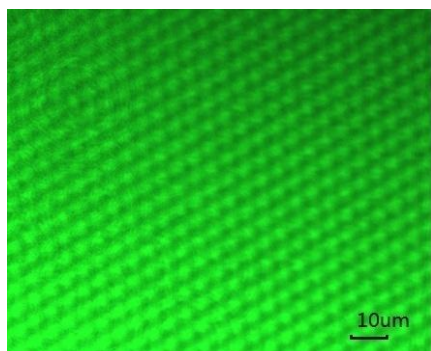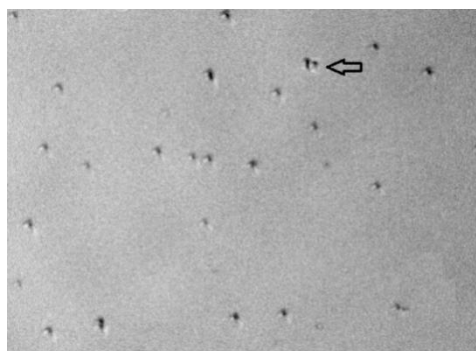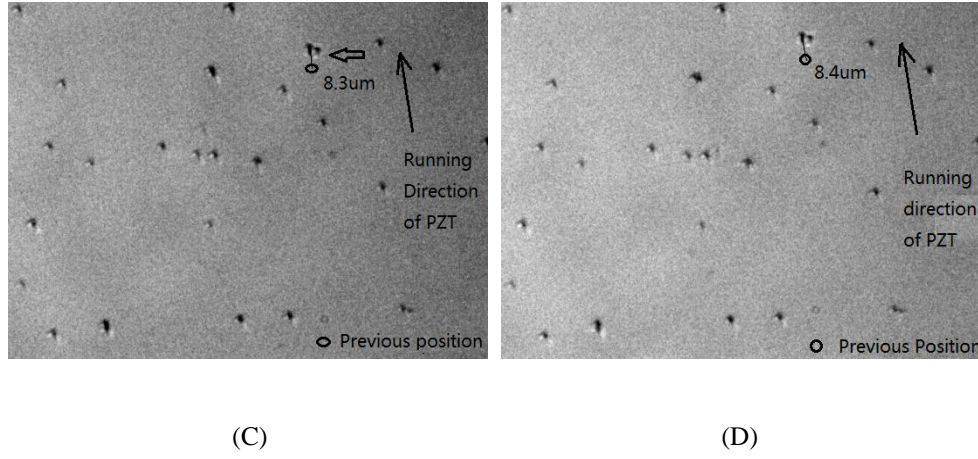
Figure 6.12 Spatial distributions of the yeast cells in the interference field. (A) Experimentally obtained patterns generated on the sample plane. (B) Initial spatial distribution of yeast cells in the sample plane in the case when the interference was switched off, and the yeast cells were in equilibrium. (C) The yeast cells were moved at a velocity of about 2μm/s in the case when the interference was switched off. (D) The yeast cells were moved at a velocity of about 2μm/s in the case when the interference was switched on.

According to the Stokes' law, the maximum deviated speed of yeast cells oriented from the centre of each dot, formed by three-beam interference, could be calculated by[71]

$$F_{drag} = 6\pi\eta R\upsilon \tag{6.12}$$

where η is the viscosity of the fluid surrounding the cells and R is the cell radius. The yeast cells were deviated by the maximum Stokes force and settled in a new equilibrium location where the drag force was compensated by the laser gradient force in the opposite direction. Figure 5 demonstrates this effect for yeast cells. Figure 6.12(A) shows a picture of regular triangle distribution of dots in an interference pattern observed by CCD. Thus, according to Eq. (6.5), the incidence angle is about 4 °, and the period of the 2D hexagonal lattice array is about 5μm. Figure 6.12(B) gives a picture of the initial spatial distribution of yeast cells when they were illuminated

by three-beam interference with the TE-TE-TM mode, and the yeast cells were in equilibrium. Figure 6.12(C) shows the movement of the yeast cells in the interference field where the interference was switched off. In this case, all of the yeast cells dragged by the movement of PZT. Figure 6.12(D) shows the movement of the yeast cells in the interference field where the interference was switched on. Then, most of yeast cells were dragged by the laser gradient force except the bigger object indicated by the arrows in the figure which could be agglomerated cells. Figure 6.12(D) shows that the yeast cells were dragged at a velocity of about 2μm/s, and then the small cells moved more rapidly towards the movement direction than large cells. Because the yeast cells are trapped by the multiple optical tweezers and the stage is dragged by the movement of PZT, the bigger object shows the relative movement of other yeast cells. According to the measurements, the interference trapping of yeast cells took place in the equilibrium at a steady rate as high as 11.6μm/s, and the trapping force started falling when the offset was greater than 1.5μm.
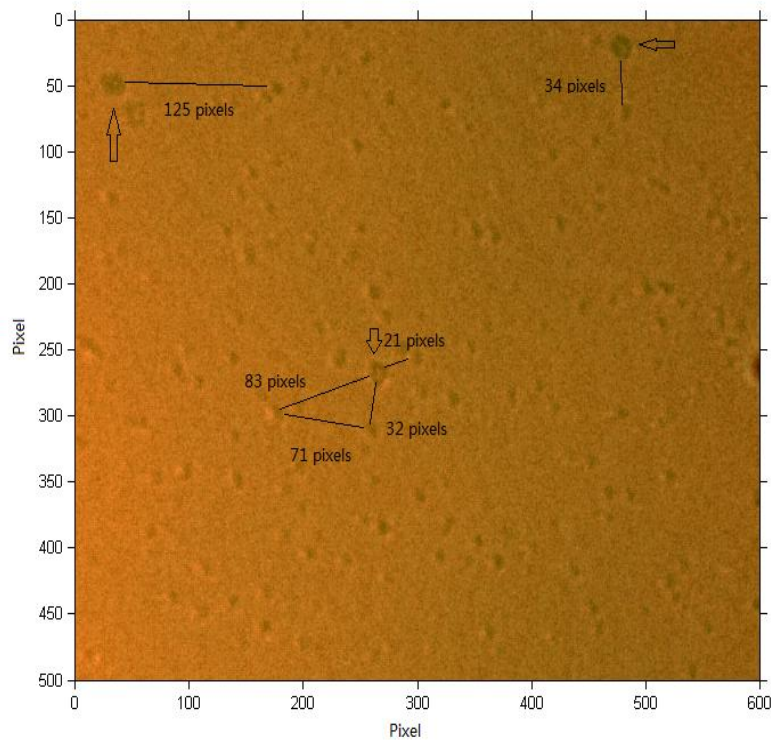
(A)
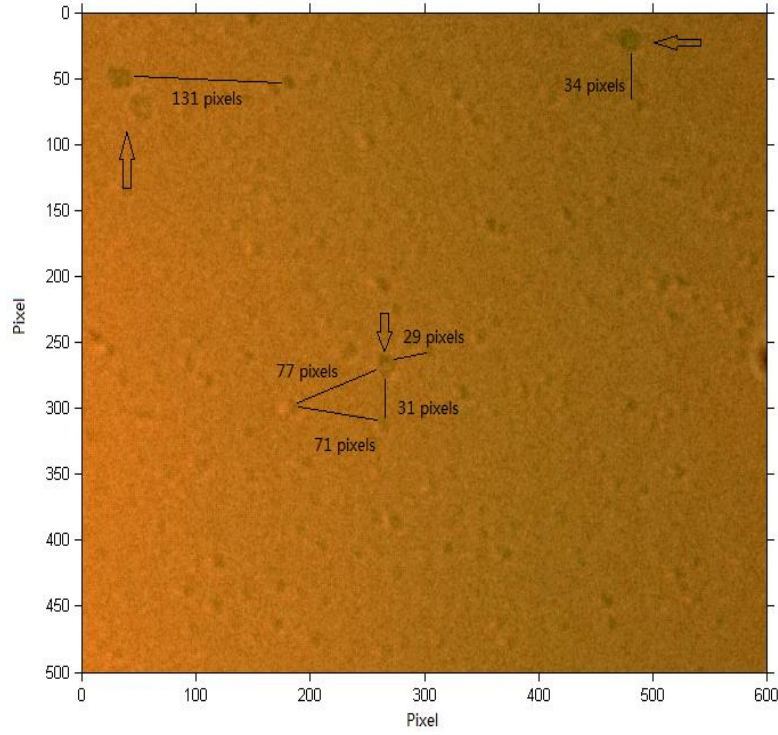
(B)

Figure 6.13 Spatial distributions of the yeast cells in the interference field dragged by the stackable

PZT. (A) Initial spatial distribution of yeast cells in the sample plane in the case when the interference

was switched off. (B) The yeast cells were moved at a velocity of about 1.5μm/s in the case when the

interference was switched on.

Figure 6.13 shows the whole array of optically trapped yeast cells dragged by the movement of the

stackable PZT. The movement of yeast cells via laser manipulation needs to realize the phase shift

on the focus by the change of light path of one beam. Hence, it can achieve a high precision on the

nano scale and hundreds of yeast cells in the interference field can be controlled, which has not

been achieved by the alternative multiple optical tweezers. The correlation coefficient of the cell

movement patterns can be calculated by[152]

$$r_k(r_1, r_2) = \frac{\text{cov}[I_0(x, y), I_k(x \pm r_1, y \pm r_2)]}{\sigma_{I_0}\sigma_{I_k}}, k = 1,2,3 \tag{6.13}$$

where I_0 and I_k are the intensity distributions of the pixels in the patterns, $\text{cov}[I_0(x, y), I_k(x \pm r_1, y \pm r_2)]$ is the covariance, and σ_{I_0} and σ_{I_k} are the standard deviations of intensity distributions, r_1 and r_2 are the phase shifts in the pixel numbers. As shown in Figure 6.13, the changes of each small cell correspond to the big cell showing that the whole array is moved from the left to the right.

6.4.2 Optical Sorting of Yeast Cells with Different Polarization Angles

Cell sorting is accomplished through the changing of laser gradient force which is proportional to the specific polarizability of the cells and the light intensity distribution in the interference field. The cell array was moved at a constant speed in the experiment, which avoided the effects of traditional manipulation with the trapezoidal acceleration motion. Then, the light intensity distribution in the interference field could be redistributed with the change of polarization angle, and the cells of interest were captured from the trap array via the different drag force. We also investigated the effect of optical sorting of yeast cells with different polarization angles.

The cells of interest could be isolated by a suitable Stokes force or drag speed corresponding to the laser gradient force. Only the cells within a certain critical size could be captured and transported by a moving gradient force and also be in the equilibrium in the motion. As shown in Figure 6.14, PZT is moved at a constant speed, and the cells have been dragged in different interference fields. Figure 6.14 demonstrates the experimental implementation of the sorting of yeast cells when the distribution of interference field is changed. By controlling the polarization angles of beams, various intensity distributions and different sizes of dots were obtained. Figure 6.14(A) shows ten cells in the illuminated field in the case where the interference was switched off. In Figure 6.14(B), the interference was switched on with the TE-TE-TM mode, and the interference field was moved by PZT at a sustained speed of 2.5μm/s. It can clearly be seen that there are three cells relatively moved toward the lower right, indicated by arrows, and the other

seven cells were trapped by the laser interference field. Then, the polarization angle is changed from the TE-TE-TM mode to the TE-TE-TE mode. The dot width in the interference field is reduced to provide the laser gradient force which is smaller than that provided by the TE-TE-TM mode. As shown in Figure 6.14(C), there are five cells relatively moved by the movement of PZT due to the change of dot size and laser intensity distribution which is in accordance with the conclusion from Figure 6.2. Moreover, two cells which are indicated by the triangles have been moved less than the three other cells due to the insufficient dragged force. With the change of the polarization angle, the shapes of the interference patterns and the value of maximum intensity change correspondingly. The simulations and the experiments have shown that the polarization angles of three interference beams have a significant impact on the shapes of the patterns and the laser gradient force.

(A)

(B)

(C)

(D)

171
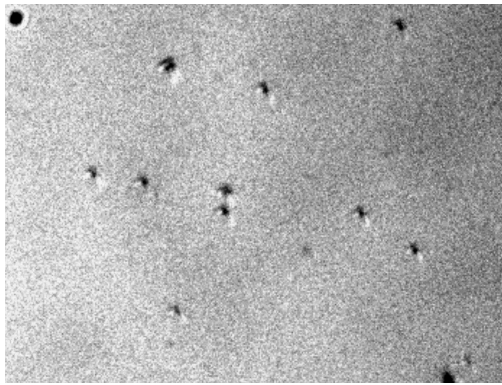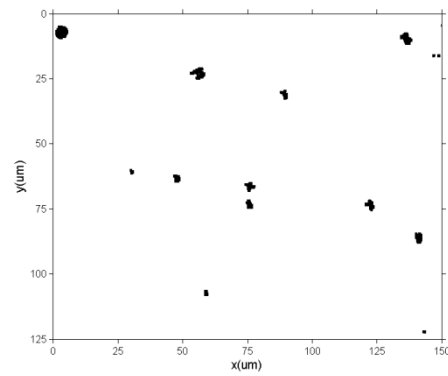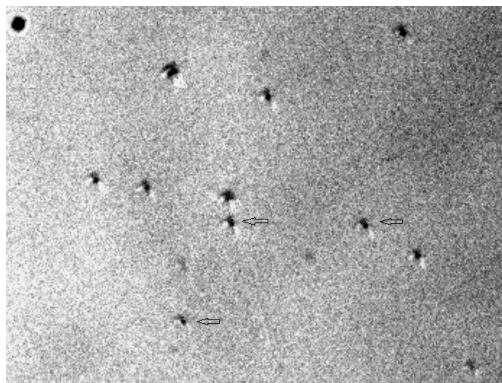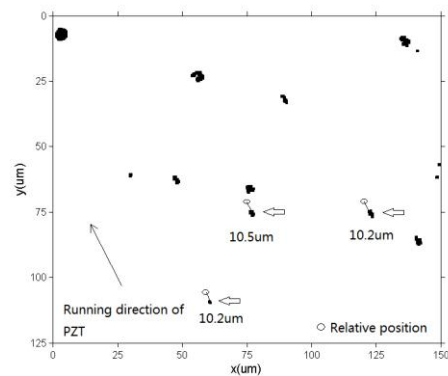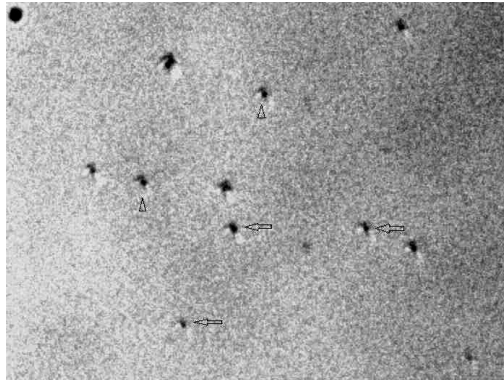
<center>(E)</center>
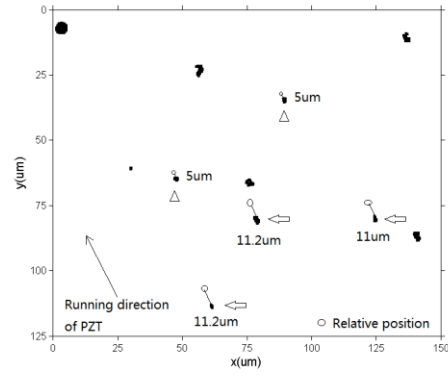
<center>(F)</center>

Figure 6.14 Sorting dynamics of the interested cells with different polarization modes. (A) Cell distribution in the illuminated field where the interference was switched off. (C) Cell distribution in the illuminated field where the interference was switched on with the TE-TE-TE mode. (E) Cell distribution in the illuminated field where the interference was switched on with the TE-TE-TM mode. (B), (D) and (F) The spatial relationships with each cell generated by MATLAB corresponding to (A), (C) and (E), respectively.

Compared with other multi-beam interference optical tweezers, without changing the device alignment of the setup, a variable and stable laser gradient force can be produced by the polarization-controlled three-beam interference experimental set-up. The set-up can generate various periodic structures with different intensities and dot sizes. Moreover, manipulation at a constant speed can avoid the influence of PZT acceleration. The selective capture and sorting of cells of different sizes by controlling the polarization angles of three beams can have new interesting possibilities of applications in cytology. In particular, applications such as sorting and separation of CTLs from a mixture of cells, capture and transportation of multiple cells are expected. The capture and sorting of biological cells are two important issues in biophysical research, and the polarization-controlled three-beam interference method can provide a way to generate various intensity distributions of optical traps with easily adjustable periods.

<center>172</center>

6.5. Summary

In this chapter, we have demonstrated a method for the capture and sorting of hundreds of cell samples using a novel polarization-controlled three-beam interference method. Firstly, three beams interference have been simulated by Matlab with the different azimuthal angles and same incident angles of $\theta_1 = \theta_2 = \theta_3 = 30°$. Then, based on the symmetrical configuration with the same incident angles and the azimuthally angles φ_n fixed as $0°$, $120°$ and $240°$ respectively, various intensity distributions are presented by changing the polarization angle of three interference beams, including the TE-TE-TE mode, TE-TE-TM mode and TE-TM-TM mode. Subsequently, the capture and sorting of yeast cells in the interference array of dots based on the change of polarization angle have been discussed. The Ray-optics model has been used to analyse the gradient force in the interference field. Finally, we have experimentally observed multiple optical tweezers and the sorting of cells with different polarization angles, which are in accordance with the theoretical analysis. Two manipulation methods based on the nano displacement platform and the stackable PZT have been implemented for the cell capture with high precision. The experimental results have shown that hundreds of yeast cells in the interference field could be realized, which has not been achieved by the alternative multiple optical tweezers, and the polarization angle affects the shapes and feature sizes of the interference patterns and the trapping force. The proposed method has its unique potential in biological research, which will be useful for the capture and sorting of cells, and the manipulation of them for further analysis.

Chapter 7

Conclusions

7.1 Summary of Thesis

The work presented in this thesis concerns the nano handling and measurement techniques for biological cells in culture. Chapter 1 provides the overview of current nano handling and measurement technologies of biological cells and describes both the advantages and limitations of each application in cytology, respectively. Chapter 2 reviews the fundamental theories and the biological cell applications of AFM and optical tweezers. With the deep investigation of traditional products, it is found that there are a number of limitations associated with the nano handling and measurement issues in the physiological cases. For instance, they cannot be used to study the suspension cells and the adherent cells simultaneously. The structural design of AFM for the air condition may not be suitable to work in liquid. There is still lack of satisfactory experimental methods and techniques for us to study cells from different aspects. Furthermore, few reports on optical tweezers have considered the dynamic analysis during the automated transportation and most of studies for the creation of multiple optical traps are limited to create a pattern of linear interference fringes or a few of dot traps without adjustable the formation. Hence, the combination and improvement of liquid-AFM and multiple optical tweezers are incorporated into the methodology of this thesis. The novel characterization methods of biological cells based on the methodology are implemented throughout the experiment research. Among them, the liquid-AFM is used both as a tool for the obtaining of true 3D surface topographical information of the living cells in vitro on the nano scale and as a force sensor for the measurement of various physical properties of biological samples, such as elasticity, adhesion, hardness and friction. Moreover, the

multiple optical tweezers can remotely manipulate the biological cells on the nano scale with less damage and provide the measurable forces and distances which are well suited for the study of cell dynamics, especially using the different forces to move and select multiple living cells. To visualize and quantify the dynamics of living cells in culture on the nano scale and accurately measure the interaction force on the surface of biological cells in the molecular level, the aim and objectives are determined accordingly.

In Chapter 3, the liquid-AFM has been developed and optimized based on the principle of atomic force microscope and its applications in cytology. Several shortcomings in current research including the insufficient area in the sample scanning, the inefficiency and less reliable in the topography of living biological sample and the incompatible AFM probe unit which cannot be used in the air conditions and liquid environments in one experiment have been solved in the novel structures. Among them, a new liquid-AFM probe unit and an increment PID control algorithm have been implemented suitable for the scan detection of cell samples in gas phase and liquid phase environments. The problems with the influence between the surface tension and the probe and the damage of probe in the sample scanning have been overcome. The proposed system is useful for the nano handling and measurement of living cells in both the air conditions and liquid environments.

In Chapter 4, by taking the strategy of the liquid-AFM, a number of emerging methods for the characterization of living biological samples in vitro were implemented based on the new structures. The biological cell imaging in different liquids was studied to improve the image quality. Subsequently, the AFM was used as a force sensor for the measurement of the adhesion force between the cell and the substrate and the mechanical properties of biological cells in culture. The Young's modulus and the cellular shear adhesion forces of two types of living cancer cells were obtained based on the measurements of the cell indentation and the deflections of the AFM cantilever in the torsional and vertical directions, respectively. The experimental results

demonstrate that the Young's modulus-frequency count distribution and the shear adhesion force of normal cancer cells is twice as much as the same type of cancer cells with TRAIL. Moreover, based on the sensitive and fast cellular shear adhesion force measurement method using an atomic force microscope, the measurement of cellular shear adhesion forces can be made based on the different positions of the cell on the nano scale. Moreover, different pushing speeds of probe and various locations of cells were used in experiments to study their influences. In this study, the measurement of the cell adhesion in the upper portion of the cell is different from that in the lower portion. It may reveal that the cancer cells have the metastasis tendency after cultured for 16 to 20 hours, which is significant for preventing metastasis in the patients diagnosed with early cancer lesions.

In Chapter 5, to overcome the limitations of liquid-AFMs including the trapping and manipulation of the cell damaged, which were difficult to achieve the manipulation in a large area and to improve the cytological diagnosis with the physical properties of the cell, the single optical tweezers was developed to integrate with the liquid-AFM. The moving nano displacement platform of liquid-AFM and the light beam phase shift were used in the optical tweezers to manipulate biological cells in culture. Moreover, the static drag force method was used to measure the cellular escape velocity, and further obtain the trapping stiffness which was similar to the numerical computations by the RO model. Among them, a new experimental method integrated with the position analysis in the Z direction was used to improve the fluid force method for the calibration and characteristic the mechanical forces exerted on optical traps and living cells. The experimental results show that the cellular escape velocity in different levels of sample plane appears quite different, and it can provide a powerful tool for the early detection and diagnosis of cancer which improves the nano handling and measurement technology by liquid-AFM.

Due to the focus of one trap on the object surface, the traditional optical tweezers cannot achieve the manipulation of multi-objects in a high efficiency and it cannot isolate the particular type cells

which usually exist in the mixture of several different morphologies of samples. Chapter 6 gives a sensitive and highly efficient polarization-controlled three-beam interference set-up for the capture and sorting of multiple cells. With the theory of superposition of three beams, simulations on the influence of polarization angle upon the intensity distribution and the laser gradient force change with different polarization angles were carried out. By controlling the polarization angles of the beams, various intensity distributions and different sizes of dots were obtained. Among them, the theoretical equations of gradient force in the interference field with the TE-TE-TE, TE-TE-TM and TE-TM-TM polarisation modes were derived and corresponding analyses demonstrated that the same particle placed on the different polarisation modes of interference fields were dragged by different gradient forces. Subsequently, we have experimentally observed multiple optical tweezers and the sorting of cells with different polarisation angles, which are in accordance with the theoretical analysis. The experimental results have shown that the polarization angle affects the shapes and feature sizes of the interference patterns and the trapping force.

In conclusion, an integrated system including the liquid-AFM and the multiple optical tweezers based on laser interference has been developed in this work to combine the advantages of high accuracy and efficiency for the nano handling and measurement of living cells. Table 7.1 shows the specifications of the integrated system. The developed system is useful for the nano handling and measurement of living cells in biomedicine.

Table 7.1 Specifications of the integrated system

	Liquid-AFM	Multiple-OT
Scanner		
Scan ranger	150μm×150μm×150μm	150μm×150μm×150μm
Open-loop resolution	0.2nm	0.2nm
Repeatability in X, Y, Z	2/2/4nm	2/2/4nm
Linearity	<0.03% Full range	<0.03% Full range
Laser	650nm	532nm
Video Microscope		
Type	Top-down video microscope	Top-down video microscope
Focus	Manual focus and zoom	Manual focus and zoom
Camera type	9M pixel color CMOS camera	9M pixel color CMOS camera/
Resolution	1.75μm	1.75μm
Magnification	5.0×	5.0×
Sample Size		
Manual X/Y stage	25mm×25mm	-
Motorized X/Y/Z stage	25mm×25mm×25mm	25mm×25mm×25mm
Standard Modes		
	Contact mode	Laser movement/Platform movement

7.2 Future Work

The work presented in the thesis aims to develop a new system and new technique which will be able to visualize and quantify the dynamics of living cells in culture on the nano scale and

accurately measure the interaction force on the surface of biological cells in the molecular level. An integrated system including the liquid-AFM and OT based on laser interference is developed and a number of significant achievements of nano handling and measurement of biological cells have been obtained, but there are still some limitations to be overcome and other potential tasks to be carried out in the future work, such as the coordination of the working speed and the accuracy for the liquid-AFM, the working mode of the liquid-AFM that may induce the cell damage in the manipulation, and the working efficiency of the multiple optical tweezers which is difficult to realize in the system adjustment Moreover, there are still lack of the significant methods for the study of both suspension cells and adherent cells at the same time.

Although the AFM has become a versatile tool with the functions for biological cell handling, imaging and force feedback. However, the scanning area is too small for many applications of cells in bioengineering, which requires a new structure of AFM or develop new scanning method for the large area scanning[153]. Besides, AFM is expected to have more functions at a high speed, high precision and large area simultaneously in the sample scanning. Recently, some AFMs with two stages appear gradually. However, the AFM based on the large area and high speed usually cannot achieve the less damaged results in the scanning due to the noise and vibrations in the integrated manipulation[154]. Hence, the requirement for the scanning of the sample with a high speed, high precision and large area simultaneously will be the indispensable improvements in the future work.

The optical tweezers system is currently the vital member of pico-Newton force spectroscopy as well as the micromanipulation tools with vast applications in the interdisciplinary research. One of the important developing trends is to integrate with various new types of light fields to carry out special or complex manipulation tasks. For instance, integrating with the ultrashort pulsed Bessel beams can realize the stable manipulation with the transferred distance in the radial direction more than 3mm[155][156][157]. Integrating with the optical vortex beam or Laguerre-Gaussian beam can be

used to study the rotation dynamics of biological cells[158][159]. Integrating with the Airy beams can trap multiple particles along the accelerating trajectory[160]. Hence, with the theories of novel optical fields, optical tweezers can be used to realize more applications in cytology.

Furthermore, the further study of the integrated system based on the liquid-AFM system and multiple optical tweezers can also offer unprecedented functionalities of the cytology examination. Since the optical tweezers system is the instrument of pico-Newton force spectroscopy and the particles in the optical field are usually suspended into the liquid, the common biological cells are not suitable for the trapping and selection. The force caused by the probe is greater than the gradient force acted on the surface of the biological cell. Hence, for these reasons, the biological cells are separated from the substrate with less damage, and the novel method with higher precision of real-time sensory information feedback has the excited potential for the future work of functionality of the cytology examination. In addition, some new methods will be further developed to the targeteding drug-delivery and study the immune function based on the integrated system.

References

[1] Lim C T, Zhou E H, Quek S T. Mechanical models for living cells- a review. Journal of Biomechanics, 2006, 39(2): 195-216.

[2] Siegel R L, Miller K D, Jemal A. Cancer statistics, 2015. CA: A Cancer Journal for Clinicians, 2015, 65(1): 5-29.

[3] Lee G, Lim C T. Biomechanics approaches to studying human diseases. Trends in Biotechnology, 2007, 25(3): 111-118.

[4] Bustamante C, Chemla Y R, Forde N R, et al. Mechanical processes in biochemistry. Annual Review of Biochemistry, 2004, 73(1): 705-748.

[5] Greenleaf W J, Woodside M T, Block S M. High- resolution, single- molecule measurements of biomolecular motion. Annual Review of Biophysics and Biomolecular Structure, 2007, 36(36): 171-190.

[6] Liu Y, Wang Z, Wang X. AFM- based study of fullerenol ($C_{60}(OH)_{24}$)- induced changes of elasticity in living SMCC-7721 cells. Journal of the Mechanical Behavior of Biomedical Materials, 2015, 45: 65-74.

[7] Bavi N, Nakayama Y, Bavi O, et al. Biophysical implications of lipid bilayer rheometry for mechanosensitive channels. Proceedings of the National Academy of Sciences, 2014, 111(38): 13864-13869.

[8] Chang L, Howdyshell M, Liao W C, et al. Magnetic tweezers- based 3D microchannel electroporation for high- throughput gene transfection in living cells. Small, 2015, 11(15): 1818-1828.

[9] Mirsaidov U, Scrimgeour J, Timp W, et al. Live cell lithography: using optical tweezers to create synthetic tissue. Lab on A Chip, 2008, 8(12): 2174-2181.

[10] Doktycz M J, Sullivan C J, Hoyt P R, et al. AFM imaging of bacteria in liquid media immobilized on gelatin coated mica surfaces. Ultramicroscopy, 2003, 97(1): 209-216.

[11] Alonso J L, Goldmann W H. Feeling the forces: atomic force microscopy in cell biology. Life Sciences, 2003, 72(23): 2553-2560.

[12] Butt H J, Cappella B, Kappl M. Force measurements with the atomic force microscope: technique, interpretation and applications. Surface Science Reports, 2005, 59(1): 1-152.

[13] Shen Y, Nakajima M, Yang Z, et al. Single cell stiffness measurement at various humidity conditions by nanomanipulation of a nano needle. Nanotechnology, 2013, 24(14): 1846-1854.

[14] Yang R, Fung C K M, Seiffert-Sinha K, et al. Real time identification of apoptosis signaling pathways using AFM- based nano robot. Nano/Molecular Medicine and Engineering (NANOMED), 2010 IEEE 4th International Conference on. IEEE, 2010: 117-120.

[15] Lang K M, Hite D A, Simmonds R W, et al. Conducting atomic force microscopy for nanoscale tunnel barrier characterizatio. Review of Scientific Instruments, 2004, 75(8): 2726-2731.

[16] Shtrahman M, Aharoni D B, Hardy N F, et al. Multifocal fluorescence microscope for fast optical recordings of neuronal action potentials. Biophysical Journal, 2015, 108(3): 520-529.

[17] Narayan K, Danielson C M, Lagarec K, et al. Multi-resolution correlative focused ion beam scanning electron microscopy: applications to cell biology. Journal of Structural Biology, 2014, 185(3): 278-284.

[18] Jinschek J R. Advances in the environmental transmission electron microscope (ETEM) for nanoscale in situ studies of gas- solid interactions. Chemical Communications, 2014, 50(21): 2696-2706.

[19] Kus J. Application of confocal laser-scanning microscopy (CLSM) to autofluorescent organic and mineral matter in peat, coals and siliciclastic sedimentary rocks- a qualitative approach. International Journal of Coal Geology, 2015, 137: 1-18.

[20] Chen W, Wang S X, et al. Study of cell toxicity of dauricine on daudi cells based on atomic force microscope. Journal of Instrumental Analysis, 2012, 31(3): 247-254.

[21] Wang M, Wei M, Cai X F, et al. Visual research of 3T3- L1 preadipocyte and cytoskeleton studied by AFM. Biotechnology, 2010, 20(5): 53-57.

[22] Sun G D, Wu S X, Li Z Z. Isolation, culture and osteogenic differentiation of mesenchymal stem cells from human umbilical cord: ultrastructure of cell membrane observed using atomic force microscope. Journal of Clinical Rehabilitative Tissue Engineering Research, 2010, 14(1): 33-37.

[23] Francis L W, Lewis P D, Wright C J, et al. Atomic force microscopy comes of age. Biology of the Cell, 2010, 102(2): 133-143.

[24] Bartenwerfer M, Fatikow S, Tunnell R, et al. Towards automated AFM- based nanomanipulation in a combined nanorobotic AFM/HRSEM/FIB system. Mechatronics and Automation (ICMA 2011) International Conference on IEEE, 2011: 171-176.

[25] Bartenwerfer M, Fatikow S. Directed nanorobot-based handling of single nanowires. Mechatronics and Automation (ICMA 2011) International Conference on IEEE, 2011: 183-188.

[26] Trache A, Lim S M. Integrated microscopy for real-time imaging of mechanotransduction studies in live cells. Journal of Biomedical Optics, 2009, 14(3): 034024-034024-13.

[27] Ahmad M R, Nakajima M, Kojima S, et al. Buckling nanoneedle for characterizing single cells mechanics inside environmental SEM. Nanotechnology, IEEE Transactions on, 2011, 10(2): 226-236.

[28] "Zyvex S100 Nanomanipulator", http://www.zyvex.com/Documents/Zyvex_S100.PDF, 2008.

[29] Pfister G, Stroh C M, Perschinka H, et al. Detection of HSP60 on the membrane surface of stressed human endothelial cells by atomic force and confocal microscopy. Journal of Cell Science, 2005, 118(8): 1587-1594.

[30] Doak S H, Rogers D, Jones B, et al. High-resolution imaging using a novel atomic force microscope and confocal laser scanning microscope hybrid instrument: essential sample preparation aspects. Histochemistry and Cell Biology, 2008, 130(5): 909-916.

[31] Haupt B J, Pelling A E, Horton M A. Integrated confocal and scanning probe microscopy for biomedical research. The Scientific World Journal, 2006, 6: 1609-1618.

[32] Liphardt J, Dumont S, Smith S B, et al. Equilibrium information from nonequilibrium measurements in an experimental test of Jarzynski's equality. Science, 2002, 296(5574): 1832-1835.

[33] Huisstede J G H, Subramaniam V, Bennink M L. Combining optical tweezers and scanning probe microscopy to study DNA-protein interactions. Microscopy Research and Technique, 2007, 70: 26-33.

[34] Donald C, Rahul T, Prasanna P S R, et al. Three- dimensional parallel particle manipulation and tracking by integrating holographic optical tweezers and engineered point spread functions. Optics Express, 2011, 19(5): 3835-3842.

[35] Gu M, Kuriakose S, Gan X. A single beam near- field laser trap for optical stretching, folding and rotation of erythrocytes. Optics Express, 2007, 15(3): 1369-1375.

[36] Visscher K, Brakenhoff G J, Krol J J. Micromanipulation by "multiple" optical traps created by a single fast scanning trap integrated with the bilateral confocal scanning laser microscope. Cytometry, 1993, 14(2): 105-114.

[37] Tatarkova S A, Carruthers A E, Dholakia K. One- dimensional optically bound arrays of microscopic particles. Physical Review Letters, 2002, 89(28): 283901-283901.

[38] Carmon G, Feingold M. Rotation of single bacterial cells relative to the optical axis using optical tweezers. Optics Letters, 2011, 36(1): 40-42.

[39] Mario F, Andrew R, Nader R S, et al. Active- passive calibration of optical tweezers in viscoelastic media. Review of Scientific Instruments, 2010, 81(1): 015103-015103-10.

[40] Binnig G, Rohrer H. Scanning tunneling microscopy. Surface Science, 1983, 126(1): 236-244.

[41] Toumey C P. Narratives for nanotech: anticipating public reactions to nanotechnology. SPT v8n2- Narratives for Nanotech: Anticipating Public Reactions to Nanotechnology, 2005.

[42] Binnig G, Quate C F, Gerber C. Atomic force microscope. Physical Review Letters, 1986, 56(9): 930-933.

[43] Huang W H, Baró A M, Sáenz J J. Electrostatic and contact forces in force microscopy. Journal of

Vacuum science & Technology. B, 1991, 9(2):1323-1328.

[44] Zhang P T. Study of feedback signal detection in atomic force microscopy. Master thesis, University of Science and Technology, 2013.

[45] Hartmann U. Theory of Van der Waals microscopy. Journal of Vacuum Science and Technology, 1991, 9(2): 465-469.

[46] Zhang H. Development of the liquid- AFMs and its application. PhD thesis, Zhejiang University, 2004.

[47] Belaidi S, Girard P, Leveque G. Electrostatic forces acting on the tip in atomic force microscopy: Modelization and comparison with analytic expressions. Journal of Applied Physics, 1997, 81(3): 1023-1030.

[48] Butt H J. Measuring electrostatic, Van der Waals, and hydration forces in electrolyte solutions with an atomic force microscope. Biophysical Journal, 1991, 60(6): 1438-1444.

[49] Eaton P, West P. Atomic force microscopy. Oxford University Press, 2010.

[50] Lee S, Sigmund W M. AFM study of repulsive van der Waals forces between Teflon AF^{TM} thin film and silica or alumina. Colloids and Surfaces A: Physicochemical and Engineering Aspects, 2002, 204(1): 43-50.

[51] Israelachvili J. Intermolecular and surface forces. Academic Press, 1992.

[52] Leveque G, Girard P, Belaidi S. Effects of air damping in noncontact resonant force microscopy. Review of Scientific Instruments, 1997, 68(11): 137-144.

[53] Chen Y F. Development of the digital AFM and its application. PhD thesis, Zhejiang University, 2005.

[54] Binning G, Rohrer H, Gerber C, et al. Surface studies by scanning tunneling microscopy. Physical Review Letters, 1982, 49(1): 57-60.

[55] Ashkin A, Dziedzic J M. Optical levitation by radiation pressure. Applied Physics Letters, 1971, 19(8): 283-285.

[56] Ashkin A, Dziedzic J M, Bjorkholm J E, et al. Observation of a single- beam gradient force optical trap for dielectric particles. Optics Letters, 1986, 11(5): 288-290.

[57] Sarshar M, Wong W T, Anvari B. Comparative study of methods to calibrate the stiffness of a single-beam gradient- force optical tweezers over various laser trapping powers. Journal of Biomedical Optics, 2014, 19(11): 115001-115001.

[58] Spyratou E, Makropoulou M, Mourelatou E A, et al. Biophotonic techniques for manipulation and characterization of drug delivery nanosystems in cancer therapy. Cancer Letters, 2012, 327(1): 111-122.

[59] Malagnino N, Pesce G, Sasso A, et al. Measurements of trapping efficiency and stiffness in optical tweezers. Optics Communications, 2002, 214(1): 15-24.

[60] Wu Y, Sun D, Huang W. Mechanical force characterization in manipulating live cells with optical tweezers. Journal of Biomechanics, 2011, 44(4): 741-746.

[61] Heller I, Hoekstra T P, King G A, et al. Optical tweezers analysis of DNA–protein complexes. Chemical Reviews, 2014, 114(6): 3087-3119.

[62] Leake M C. Combined magneto- optical tweezers and supperesolution fluorescence imaging for probing dynamic single- molecule topology of DNA, and protein machines that manipulate DNA topology. Biophysical Journal, 2015, 108(2): 232a-233a.

[63] Sinclair G, Leach J, Jordan P, et al. Interactive application in holographic optical tweezers of a multi-plane Gerchberg-Saxton algorithm for three-dimensional light shaping. Optics Express, 2004, 12(8): 1665-1670.

[64] Simmons R M, Finer J T, Chu S, et al. Quantitative measurements of force and displacement using an optical trap. Biophysical Journal, 1996, 70(4): 1813.

[65] Svoboda K, Block S M. Biological applications of optical forces. Annual Review of Biophysics and Biomolecular Structure, 1994, 23(1): 247-285.

[66] Gouesbet G, Berlemont A. Eulerian and Lagrangian approaches for predicting the behaviour of discrete particles in turbulent flows. Progress in Energy and Combustion Science, 1999, 25(2):

133-159.

[67]Zhu Y Y, Ding X F, Gao Q J, et al. The calculation and numerical simulation on optical trapping force in lateral way of One- beam laser optical tweezers. Laser Journal, 2006, 27(1):69-70.

[68] Wang W C. Electromagnetic wave theory. Wiley Press, 1987.

[69] Rubinov A N, Afanas' Ev A A. Application of gradient laser fields in biology and medicine: physical principles and prospects. XVII International Conference on Coherent and Nonlinear Optics (ICONO 2001). International Society for Optics and Photonics, 2002: 207-220.

[70] Rubinov A N. Physical grounds for biological effect of laser radiation. Journal of Physics D: Applied Physics, 2003, 36(19): 2317-2330.

[71] Itami M, Sasa S I. Derivation of Stokes' law from Kirkwood's formula and the Green-Kubo formula via large deviation theory. Journal of Statistical Physics, 2015, 161(3): 532-552.

[72] Wang H, Fu Y, Zickmund P, et al. Coherent anti-stokes Raman scattering imaging of axonal myelin in live spinal tissues. Biophysical Journal, 2005, 89(1): 581-591.

[73] Gittes F, Schmidt C F. Signals and noise in micromechanical measurements. Methods in Cell Biology, 1998, 55: 129-156.

[74] Yang I H, Co C C, Ho C C. Alteration of human neuroblastoma cell morphology and neurite extension with micropatterns. Biomaterials, 2005, 26(33): 6599-6609.

[75] Chakraborty J, Von S G A. Pleomorphism of human prostatic cancer cells (DU 145) in culture- the role of cytoskeleton. Experimental and Molecular Pathology, 1986, 44(2): 235-245.

[76] Taniguchi S. Suppression of cancer phenotypes through a multifunctional actin- binding protein, calponin, that attacks cancer cells and simultaneously protects the host from invasion. Cancer Science, 2005, 96(11): 738-746.

[77] Han J D, Rubin C S. Regulation of cytoskeleton organization and paxillin dephosphorylation by cAMP studies on murine Y1 adrenal cells. Journal of Biological Chemistry, 1996, 271(46): 29211-29215.

[78] Barrera N P, Herbert P, Henderson R M, et al. Atomic force microscopy reveals the stoichiometry and subunit arrangement of 5-HT3 receptors. Proceedings of the National Academy of Sciences of the United States of America, 2005, 102(35): 12595-12600

[79] Horton M, Charras G, Lehenkari P. Analysis of ligand–receptor interactions in cells by atomic force microscopy. Journal of Receptors and Signal Transduction, 2002, 22(1-4): 169-190.

[80] Hansma H G, Kasuya K, Oroudjev E. Atomic force microscopy imaging and pulling of nucleic acids. Current Opinion in Structural Biology, 2004, 14(3): 380-385.

[81] Xu J P, Ji J, Chen W D, et al. Novel biomimetic surfactant: synthesis and micellar characteristics. Macromolecular Bioscience, 2005, 5(2): 164-171.

[82] Variola F. Atomic force microscopy in biomaterials surface science. Physical Chemistry Chemical Physics, 2015, 17(5): 2950-2959.

[83] Bowen R L, Perry G, Xiong C, et al. A clinical study of lupron depot in the treatment of women with Alzheimer's disease: preservation of cognitive function in patients taking an acetylcholinesterase inhibitor and treated with high dose lupron over 48 weeks. Journal of Alzheimer's Disease: JAD, 2015, 44(2): 549-560.

[84] Berdyyeva T K, Woodworth C D, Sokolov I. Human epithelial cells increase their rigidity with ageing in vitro: direct measurements. Physics in Medicine and Biology, 2005, 50(1): 81-92.

[85] Corbin E A, Kong F, Lim C T, et al. Biophysical properties of human breast cancer cells measured using silicon MEMS resonators and atomic force microscopy. Lab on A Chip, 2015, 15(3): 839-847.

[86] Hecht F M, Rheinlaender J, Schierbaum N, et al. Imaging viscoelastic properties of live cells by AFM: power-law rheology on the nanoscale. Soft Matter, 2015, 11: 4584-4591.

[87] Dufrêne Y F. Sticky microbes: forces in microbial cell adhesion. Trends in Microbiology, 2015, 23(6): 376-382.

[88] Beaussart A, El-Kirat-Chatel S, Sullan R M A, et al. Quantifying the forces guiding microbial cell adhesion using single-cell force spectroscopy. Nature Protocols, 2014, 9(5): 1049-1055.

[89] Mel D A, Ramesh B, Scurr D J, et al. Fumed silica nanoparticle mediated biomimicry for optimal cell– material interactions for artificial organ development. Macromolecular bioscience, 2014, 14(3): 307-313.

[90] Gou X, Yang H, Fahmy T M, et al. Direct measurement of cell protrusion force utilizing a robot-aided cell manipulation system with optical tweezers for cell migration control. The International Journal of Robotics Research, 2014: 0278364914546536.

[91] Mills J P, Qie L, Dao M, et al. Nonlinear elastic and viscoelastic deformation of the human red blood cell with optical tweezers. Mechanics & Chemistry of Biosystems Mcb, 2004, 1(3): 169-180.

[92] Dobrzyńska I, Szachowicz-Petelska B, Sulkowski S, et al. Changes in electric charge and phospholipids composition in human colorectal cancer cells. Molecular and Cellular Biochemistry, 2005, 276(1-2): 113-119.

[93] Pesce G, Rusciano G, Sasso A, et al. Surface charge and hydrodynamic coefficient measurements of Bacillus subtilis spore by optical tweezers. Colloids & Surfaces B Biointerfaces, 2014, 116(2): 568-575.

[94] Liu J. Advanced PID control and its MATLAB simulation. Publishing House of Electronics Industry Press, 2004.

[95] Alonso J L, Goldmann W H. Feeling the forces: atomic force microscopy in cell biology. Life Sciences, 2003, 72(23): 2553-2560.

[96] Siegel R, Naishadham D, Jemal A. Cancer statistics, 2013. CA: A Cancer Journal for Clinicians, 2013, 63(1): 11-30.

[97] Gauthier M, Régnier S, Rougeot P, et al. Analysis of forces for micromanipulations in dry and liquid media. Journal of Micromechatronics, 2006, 3(3): 389-413.

[98] Jones R E, Hart D P. Force interactions between substrates and SPM cantilevers immersed in fluids. Tribology International, 2005, 38(3): 355-361.

[99] Rogowska J, Patel N, Plummer S, et al. Quantitative optical coherence tomographic elastography:

method for assessing arterial mechanical properties. British Journal of Radiology, 2006, 79(945): 707-711.

[100] Karimi A, Navidbakhsh M, Alizadeh M, et al. A comparative study on the mechanical properties of the umbilical vein and umbilical artery under uniaxial loading. Artery Research, 2014, 8(2): 51-56.

[101] Achterberg V F, Buscemi L, Diekmann H, et al. The nano scale mechanical properties of the extracellular matrix regulate dermal fibroblast function. Journal of Investigative Dermatology, 2014, 134(7): 1862-1872.

[102] Zhu Y, Dong Z, Wejinya U C, et al. Determination of mechanical properties of soft tissue scaffolds by atomic force microscopy nanoindentation. Journal of Biomechanics, 2011, 44(13): 2356-2361.

[103] McKee C T, Last J A, Russell P, et al. Indentation versus tensile measurements of Young's modulus for soft biological tissues. Tissue Engineering Part B: Reviews, 2011, 17(3): 155-164.

[104] Liu X G, Song Z X, Qu Y M, et al. Mechanical properties study of SW480 cells based on AFM. Cell Biology International, 2015, 39(8): 972-977

[105] Ko T J, Kim E, Nagashima S, et al. Adhesion behavior of mouse liver cancer cells on nanostructured superhydrophobic and superhydrophilic surfaces. Soft Matter, 2013, 9(36): 8705-8711.

[106] Yeung T, Georges P C, Flanagan L A, et al. Effects of substrate stiffness on cell morphology, cytoskeletal structure, and adhesion. Cell Motility and the Cytoskeleton, 2005, 60(1): 24-34.

[107] Carey S P, Charest J M, Reinhart-King C A. Forces during cell adhesion and spreading: implications for cellular homeostasis. Cellular and Biomolecular Mechanics and Mechanobiology, 2011, 4: 29-69.

[108] Thomas W E, Trintchina E, Forero M, Vogel V, Sokurenko E V. Bacterial adhesion to target cells enhanced by shear force. Cell, 2002, 109(7): 913-923.

[109] Noy A, Friddle R W. Practical single molecule force spectroscopy: how to determine

fundamental thermodynamic parameters of intermolecular bonds with an atomic force microscope. Methods, 2013, 60(2): 142-150.

[110] Whited A M, Park P S H. Atomic force microscopy: a multifaceted tool to study membrane proteins and their interactions with ligands. Biochimica et Biophysica Acta (BBA)-Biomembranes, 2014, 1838(1): 56-68.

[111] Huang Y X. Cell biomechanics. Physics, 2005, 34(6): 433-441.

[112] Morkvėnaitė-Vilkončienė I, Ramanavičienė A, Ramanavičius A. Atomic force microscopy as a tool for the investigation of living cells. Medicina (Kaunas), 2013, 49(4): 155-164.

[113] Evans E A, Calderwood D A. Forces and bond dynamics in cell adhesion. Science, 2007, 316(5828): 1148-1153.

[114] Haimovitz-Friedman A, Falcone D J, Eldor A, et al. Activation of platelet heparitinase by tumor cell-derived factors. Blood, 1991, 78(3): 789-796.

[115] Vremec D, Hansen J, Strasser A, et al. Maintaining dendritic cell viability in culture. Molecular Immunology, 2015, 63(2): 264-267.

[116] Du E, Dao M, Suresh S. Quantitative biomechanics of healthy and diseased human red blood cells using dielectrophoresis in a microfluidic system. Extreme Mechanics Letters, 2014, 1: 35-41.

[117] Chen S, Cheng J, Kong CW, et al. Laser-induced fusion of human embryonic stem cells with optical tweezers. Applied Physics Letters, 2013, 103(3): 033701.

[118] Picas L, Milhiet PE, Hernández-Borrell J. Atomic force microscopy: A versatile tool to probe the physical and chemical properties of supported membranes at the nanoscale. Chemistry and physics of lipids, 2012, 165(8): 845-860.

[119] Lee C C, Wu C C, Su F C. The technique for measurement of cell adhesion force. Journal of Medical and Biological Engineering, 2004, 24(1): 51-56.

[120] Shen Y, Nakajima S, Kojima S, et al. Single cell adhesion force measurement for cell viability identification using an AFM cantilever-based micro putter. Measurement Science & Technology,

2011, 22(11): 115802.

[121] Maciaszek JL, Andemariam B, Abiraman K, Lykotrafitis G. AKAP- dependent modulation of BCAM/Lu adhesion on normal and sickle cell disease RBCs revealed by force nanoscopy. Biophysical Journal, 2014, 106(6): 1258-1267.

[122] Maciaszek J L, Partola K, Zhang J, et al. Single- cell force spectroscopy as a technique to quantify human red blood cell adhesion to subendothelial laminin. Journal of biomechanics, 2014, 47(16): 3855-3861.

[123] Butt H J, Cappella B, Kappl M. Force measurements with the atomic force microscope: technique, interpretation and applications. Surface Science Reports, 2005, 59(1): 1-152.

[124] Hoogenboom P C J, Spaan R. Shear stiffness and maximum shear stress of tubular members. The Fifteenth International Offshore and Polar Engineering Conference. International Society of Offshore and Polar Engineers, 2005.

[125] Zhang X Z, Kuang Z B, Cai S X, et al. Single micropipette aspiration technique for measuring the shearing adhesion force of cells. Journal of experimental mechanics, 2000, 15(1): 9-14.

[126] Mises R V. On Saint-Venant's principle. Bulletin of the American Mathematical Society, 1945, 51(8): 555-562.

[127] Chaffer C L, Weinberg R A. A perspective on cancer cell metastasis. Science, 2011, 331(6024): 1559-1564.

[128] Shen Y, Nakajima M, Kojima S, et al. Single cell adhesion force measurement for viability identification using nanorobotic manipulation system inside ESEM. IEEE International Conference on Nano/micro Engineered & Molecular Systems, 2011: 944-947.

[129] Jákl P, Arzola A V, Šiler M, et al. Optical sorting of nonspherical and living microobjects in moving interference structures. Optics express, 2014, 22(24): 29746-29760.

[130] Ren X, Wang C, Li Y, et al. Optical tweezers array system based on 2D photonic Crystals. Physics Procedia, 2011, 22: 493-497.

[131] Kogelnik H, Li T. Laser beams and resonators. Applied Optics, 1966, 5(10): 1550-1567.

[132] Huang P, Guasto J S, Breuer K S. Direct measurement of slip velocities using three-dimensional total internal reflection velocimetry. Journal of fluid mechanics, 2006, 566: 447-464.

[133] Wu Y H. Force Characterization and motion planning in automated cell manipulation by optical tweezers. University of Science and Technology of China. 2011.

[134] Lesot M J. Similarity, typicality and fuzzy prototypes for numerical data. 6th European Congress on Systems Science, Workshop Similarity and resemblance, 2005, 94: 95.

[135] Xin H, Li X, Li B. Massive photothermal trapping and migration of particles by a tapered optical fiber. Optics Express, 2011, 19(18): 17065-17074

[136] McCauley M J, Williams M C. Mechanisms of DNA binding determined in optical tweezers experiments. Biopolymers, 2007, 85(2): 154-168.

[137] Fore S, Chan J, Taylor D, et al. Raman spectroscopy of individual monocytes reveals that single-beam optical trapping of mononuclear cells occurs by their nucleus. Journal of Optics, 2011, 13(4): 044021.

[138] Castelain M, Rouxhet P G, Pignon F, et al. Single-cell adhesion probed in-situ using optical tweezers: a case study with Saccharomyces cerevisiae. Journal of Applied Physics, 2012, 111(11):114701-114701-13.

[139] Ritter A, Asano Y, Stinchcombe J, et al. Actin depletion initiates events leading to granule secretion at the immunological synapse. Immunity, 2015, 42(5): 864–876.

[140] Jákl P, Šiler M, Zemánek P. Experimental analysis of multiple-beam interference optical traps. XIX Polish-Slovak-Czech Optical Conference on Wave and Quantum Aspects of Contemporary OpticsInternational Society for Optics and Photonics, 2014: 944105-944105-6.

[141] Mirsaidov U, Scrimgeour J, Timp W, et al. Live cell lithography: using optical tweezers to create synthetic tissue. Lab on A Chip, 2008, 8(12): 2174-2181.

[142] Liu C X, Guo Z Y, Li Y, et al. Manipulating ellipsoidal micro-particles by femtosecond vortex tweezers. Journal of Optics, 2015, 17(3): 035402.

[143] Jákl P, Arzola A V, Šiler M, et al. Optical sorting of nonspherical and living microobjects in

moving interference structures. Optics Express, 2014, 22(24): 29746-29760.

[144] Kruchenok J V, Bushuk S B, Kurilo G I, et al. Orientation of red blood cells and rouleaux disaggregation in interference laser fields. Journal of Biological Physics, 2005, 31(1): 73-85.

[145] Zhang J, Wang Z, Xu D, et al. Effects of azimuthal angles on laser interference lithography. Applied Optics, 2014, 53(27): 6294-6301.

[146] Bushuk S B, Kruchenok J V, Kurilo G I, et al. Orientation of erythrocytes in the fringes of an interference laser field. Journal of Optics A Pure & Applied Optics, 2005, 7(8):382-385.

[147] Ashkin A, Dziedzic J M, Bjorkholm J E, et al. Observation of a single- beam gradient force optical trap for dielectric particles. Optics Letters, 1986, 11(5): 288-290.

[148] Rohrbach A, Stelzer E H. Optical trapping of dielectric particles in arbitrary fields. J. Opt. Soc. Am. A. Opt. Image Sci. Vis., 2001, 18(4): 839-853.

[149] Gauthier R C, Wallace S. Optical levitation of spheres: analytical development and numerical computations of the force equations. Journal of the Optical Society of America B, 1995, 12(9): 1680-1686.

[150] Saleh B E A, Teich M C, Masters B R. Fundamentals of photonics, second edition. Journal of Biomedical Optics, 2008, 13: 87.

[151] Wu C, Kahn M, Moy W. Piezoelectric ceramics with functional gradients: a new application in material design. Journal of the American Ceramic Society, 1996, 79(3): 809-812.

[152] Liu L J, Xu H M, Song Z X, et al. Phase difference determination by fringe pattern correlation. Mechatronics and Automation (ICMA 2009) International Conference on IEEE, 2009: 4868-4873.

[153] Aoki J, Gao W, Kiyono S, et al. A high precision AFM for nanometrology of large area micro-structured surfaces. Key Engineering Materials, 2005, 295(1): 65-70.

[154] Ando T, Uchihashi T, Kodera N. High-speed AFM and applications to biomolecular systems. Annual Review of Biophysics, 2013, 42(42): 393-414.

[155] Wu F, Chen Y, Guo D. Nanosecond pulsed Bessel-Gauss beam generated directly from a Nd: YAG axicon-based resonator. Applied Optics, 2007, 46(22): 4943-4947.

[156] Zhu Z, Zhang B F, Chen H, et al. Optical trapping with focused Airy beams. Applied Optics, 2011, 50(1):43-49.

[157] Garcés-Chávez V, McGloin D, Melville H, et al. Simultaneous micromanipulation in multiple planes using a self-reconstructing light beam. Nature, 2002, 419(6903): 145-147.

[158] Gahagan K T, Swartzlander G A. Optical vortex trapping of particles. Optics Letters, 1996, 21(11):827-829.

[159] Molina-Terriza G, Torres J P, Torner L. Twisted photons. Nature Physics, 2007, 3(5): 305-310.

[160] Wu F, Chen Y, Guo D. Nanosecond pulsed Bessel-Gauss beam generated directly from a Nd: YAG axicon-based resonator. Applied Osptics, 2007, 46(22): 4943-4947.